Hamburger Schriftenreihe
Produktentwicklung und Konstruktionstechnik

Technische Universität Hamburg-Harburg
Institut für Produktentwicklung und Konstruktionstechnik
Univ.-Prof. Dr.-Ing. D. Krause
Denickestraße 17
21073 Hamburg

Conny Schillo

Reliability Based Design of Unstiffened Fibre Reinforced Composite Cylinders

Bibliografische Information der Deutschen Nationalbibliothek
Die Deutsche Nationalbibliothek verzeichnet diese Publikation in der Deutschen Nationalbibliothek; detaillierte Daten sind im Internet über http://www.dnb.de abrufbar.

Impressum

TUTECH Verlag
TUTECH INNOVATION GmbH
Harburger Schloßstraße 6-12
21079 Hamburg

Telefon: +49 40 76629-0
Fax: +49 40 76629-6559
E-Mail: verlag@tutech.de
www.tutechverlag.de

Hamburger Schriftenreihe Produktentwicklung und Konstruktionstechnik
ISSN 1868-6885

1. Auflage April 2017
ISBN 978-3-946094-14-2

Reliability Based Design of Unstiffened Fibre Reinforced Composite Cylinders

Vom Promotionsausschuss der
Technischen Universität Hamburg-Harburg

zur Erlangung des akademischen Grades
Doktor-Ingenieurin (Dr.-Ing.)

genehmigte Dissertation

von
Conny Schillo

aus
Simmern

2016

1. Gutachter: Prof. Dr.-Ing. Dieter Krause

2. Gutachter: Prof. Dr.-Ing. Benedikt Kriegesmann

Tag der mündlichen Prüfung: 14.12.2016

Vorwort

Die vorliegende Arbeit entstand während meiner Tätigkeit als wissenschaftliche Mitarbeiterin am Institut für Produktentwicklung und Konstruktionstechnik der Technischen Universität Hamburg-Harburg.

An erster Stelle gilt mein Dank dem Leiter des Instituts, Herrn Prof. Dr.-Ing. Dieter Krause, der mir die Möglichkeit gegeben hat diese Arbeit durchzuführen und immer zu einer konstruktiven Arbeitsatmosphäre beigetragen hat.

Bei Herrn Prof. Dr.-Ing. Benedikt Kriegesmann bedanke ich mich für sein Interesse an meiner Arbeit und seine stete Diskussionsbereitschaft im Verlauf meiner Tätigkeit. Herrn Prof. Dr. Ing. Karl Schulte danke ich für seine Hilfsbereitschaft bei kurzfristig auftretenden Fragestellungen und für die Möglichkeit die Ressourcen seines Instituts für Materialversuche in Anspruch nehmen zu dürfen. Den Kollegen am THF sei an dieser Stelle für ihre freundliche Unterstützung ebenfalls gedankt.

Für die tatkräftige Unterstützung bei der Hexapod-Versuchsdurchführung möchte ich mich bei meinen Kollegen Olaf Rasmussen, Benedikt Plaumann, Karsten Albers und Manfred Röhrig sowie meinem Studententeam bedanken. Micah Kranz, der mich bei den Materialversuchen als wissenschaftliche Hilfskraft über einen langen Zeitraum unterstützt hat, danke ich besonders für seine zuverlässige Mitarbeit.

Für den regelmäßigen fachlichen Austausch möchte ich mich außerdem sehr herzlich bei Dr. Tristan Lippert von der TU und Dirk Wilckens vom DLR Braunschweig bedanken.

Zum Schluss gilt mein Dank meinem Mann Niels für seine fortwährende und unermüdliche Unterstützung, die es mir insbesondere erlaubt hat diese Arbeit während meiner Elternzeit fertig zu stellen.

Zusammenfassung

In der Raumfahrt verwendete unversteifte Zylinderschalen unterliegen besonders hohen Ansprüchen bezüglich der Beherrschung von Unsicherheiten und des Gewichtes. Bisher verwendete Richtlinien basieren auf deterministischen Methoden und Daten von metallischen Zylindern, welche sich in ihrer Charakteristik deutlich von Schalen aus Kohlefaserverbundwerkstoffen unterscheiden. In der vorliegenden Arbeit wird mit Hilfe umfangreicher Versuche und Untersuchungen an Schalen aus Kohlefaserverbundwerkstoffen eine probabilistische Methode entwickelt, um fertigungs-, test- und modellbedingte Unsicherheiten innerhalb eines Bayes'schen Rahmenwerkes zu quantifizieren und entsprechende Sicherheitsfaktoren zu kalibrieren.

Dazu werden zunächst systematisch fertigungs- und testumgebungsbedingte Unsicherheiten auf Mikro-, Meso- und Makroebene bestimmt. Im Rahmen einer Sensitivitätsanalyse werden die Parameter bestimmt, welche einen signifikanten Einfluss auf die Beullast haben und deren stochastisches Verhalten somit berücksichtigt werden sollte.

Es wird ein Bayes'sches Rahmenwerk entwickelt innerhalb dessen die relevanten Unsicherheiten aktualisiert werden, sobald neue Messdaten vorhanden sind. Diese dienen als Input für eine Monte-Carlo Simulation, die eine Verteilungskurve für die zu erwartende Streuung der Beullast berechnet. Aus dieser wird ein Sicherheitsfaktor für die struktur- bzw. fertigungsbezogenen Unsicherheiten kalibriert. Zusätzlich wird mit Hilfe der Strukturversuche ein Bayes'sches Fehlermodell ausgewertet, das die Modellunsicherheit analysiert und einen Sicherheitsfaktor zu deren Abdeckung liefert.

Die entwickelte Methode bietet die Möglichkeit in Abhängigkeit der gewünschten Zuverlässigkeit und der a priori vorhanden Kenntnisse bzgl. der Unsicherheiten Sicherheitsfaktoren zu kalibrieren. Dies ermöglicht eine verbesserte Ausschöpfung des Leichtbaupotentials.

Mit Hilfe der verwendeten Bayes'schen Statistik ist es außerdem in transparenter Weise möglich, die statistische Datenbasis für CFK-Zylinder sowie die berechneten Sicherheitsfaktoren für andere Zylinderdesigns zu übertragen bzw. weiter zu entwickeln.

Contents

List of Figures

List of Tables

List of Abbreviations

A_{kl}, B_{kl}	Fourier Coefficients	-
Cov	Covariance	-
DLR	German Aerospace Center	-
$\overline{D_x}, \overline{D_y}, \overline{D_{xy}}$	bending stiffness per unit width of wall in x- and y-direction and twisting stiffness, respectively;	Nmm
E_1, E_2	stiffness in longitudinal and transverse direction, respectively	N/mm²
EE_i	Elementary Effect i	-
$E_f^{'}$	bending storage modulus	N/m²
$E_f^{''}$	loss modulus	N/m²
$\overline{E_x}, \overline{E_y}, \overline{E_{xy}}$	extensional stiffness of wall in x-, y- and shear-direction, respectively	N/mm²
FE	Finite Element	-
Fx, Fy	shear forces applied at load introduction of cylinder in x- and y-direction	kN
$\overline{G_{xy}}$	shear stiffness of orthotropic or sandwich wall in x-y plane	N/mm²
L	length of cylinder	mm
MC	Monte Carlo	-
N_1	design buckling load as defined for Single Perturbation Load Approach	kN
N_x	axial compression load	kN
P_1	perturbation load	N
R	radius of cylinder	mm
TUHH	TU Hamburg	-
Y	vector of test results	kN

$\overline{W}(x,y)$	deflection of cylinder wall at point (x,y)	mm
b^{low}, b^{up}	lower and upper bound for parameter variation for Morris Screening	-
cov	coefficient of variation	-
e	error term	-
f_{ri}	resonance frequency	1/s
Δf_i	distance between the values at +/-3 dB next to the resonance frequency	1/s
H	thickness of strip specimen	mm
k	torsional spring stiffness replacing fixed boundary condition	Nmm/°
k_i^2	correction factor depending on the Eigenmode number	-
l	length of strip specimen	mm
m	number of buckle half waves in axial direction	-
n	number of buckle waves in the circumferential direction	-
phi_1,…, phi_6	fibre angles in layer 1 to 6	°
p	perturbation level	-
p_f	probability of failure	-
q	vector of simulated data	kN
r	number of repetitions in Morris Screening	-
sem	standard error of the mean	-
t	cylinder wall thickness	mm
unc	level of uncertainty for Morris Screening; value between 0 and 1	-
$x_{50\%}$	characteristic value, 50% quantile	kN
x_D	design point	kN

Φ	cumulative distribution function of the standard normal distribution	-
Θ	model parameter	-
Θ_k^r, Θ_{ref}	set of model parameters at r-th repetition and reference set, respectively	-
β	safety index	-
β^*	buckle aspect ratio ($nL/\pi Rm$)	-
Δ	perturbation coefficient	-
ε	experimental observations	-
γ	global safety factor	-
γ_m	safety factor covering model uncertainty	-
γ_R	safety factor covering material and structural uncertainties	-
$\overline{\varphi_{kl}}, \overline{\xi_{kl}}$	phase shift angle and amplitude for Fourier representation	-
μ	mean value	-
σ	standard deviation	-
ρ	density	g/cm^3
ρ^*	autocorrelation	-
θ_i	realisation of model parameter	-

1 Introduction

1.1 Motivation

In the structural design process it is common practice to consider only nominal means as input variables and to evaluate the resulting design against design criteria. To guarantee a certain degree of conservatism, the computed stress level is not compared to the material strength but to the material strength multiplied by an empirical safety factor. Although this approach can usually be called successful in terms of low failure rates and implicit conservatism, the neglect of variant input data leads to several shortcomings. Firstly, to guarantee a conservative design, the deterministic approach requires the assumption of a worst case scenario for all input parameters, all occurring simultaneously, thus leading to overly conservative and heavy weight designs. Secondly, the system inherent safety is in fact often not known. Especially for the development of prototypes, the application of safety factors can be subject to discussions. A commonly asked question is how far the safety factor can be reduced in favour of the goals of lightweight design and low cost. Since there is generally not enough information about the relevant scatter of input variables and their influence on the structural behaviour, the safety factor cannot easily be changed. To exploit lightweight potential, it is hence necessary to quantify relevant uncertainties of influencing parameters and the structural sensitivity towards them. This is also the basis to apply a reliability based design approach.

In the case of designing unstiffened cylinders, the relevant design guideline by National Aerospace and Space Administration (NASA) [Wei65b] utilises a global knockdown factor that has been fitted to test data of axially compressed cylinders that were available in 1965. Since different test institutes contributed, different materials, test setups and boundary conditions are used that are not comparable. Furthermore, no fibre reinforced plastic (FRP) cylinders are represented in the test data. The safety margin of cylinders made of carbon fibre reinforced plastics (CFRP) and designed according to this guideline is hence not known.

Further uncertainties related to the design with FRP materials arise due to the manufacturing method employed and the geometric imperfections caused by it that has not been investigated thoroughly yet [Chr95]. Since the material properties of CFRP are created during the manufacturing process, there is also a discrepancy between the stiffness expected according to the classic lamination theory, the stiffness measured by coupon tests and structural stiffness achieved in the structure.

1.2 Objective of the thesis

This thesis aims at developing a reliability based design approach for unstiffened shells based on own experimental data and identification as well as quantification of all relevant uncertainties.

The first part of this thesis is concerned with experimental work. Quantification of uncertainties related to the stiffness evaluation of coupon test data is performed using different test preparations for tension testing as well as a different test method that uses the measurement of eigenfrequencies to determine the bending stiffness. A quantitative assessment of the testing influences is performed to determine the scatter of the stiffness properties.

Secondly, 12 CFRP cylinders with layup $[90/+30/-30]_S$ are manufactured at the German Aerospace Centre (DLR) in Braunschweig using the fibre placement method and geometric imperfections are optically measured to create a statistical data base. Microsections of several cylinders are taken to quantify statistical properties of fibre volume fraction, thickness and winding angle. These measurements are used to carry out Monte Carlo (MC) analysis to predict a probability density function of the load bearing capacity of the cylinders. From this, a safety factor for the structural resistance is computed.

Eleven cylinders are tested in axial compression on the Hexapod test rig at Hamburg University of Technology (TUHH) and buckling loads as well as occurring load imperfections are recorded. This data is used to determine the model uncertainty related to finite element (FE) models employing different degrees of information, representing different design stages. Additionally, a safety factor is computed covering the remaining model uncertainty using a Bayesian updating process.

The cylinders tested are the first statistically meaningful dataset of quasi-isotropic cylinders, including measurements of all relevant manufacturing uncertainties and load imperfections during test. The developed reliability based method to calibrate safety factors for structural as well as model uncertainties allows for higher exploitation of lightweight potential. Furthermore, the proposed Bayesian framework offers a trans-

parent and systematic approach to update the measured uncertainties as well as the safety factors in case new measurement data becomes available.

1.3 Structure of the thesis

In section 2 the state of the art concerning the buckling behaviour of unstiffened shells is described. Apart from the explanation of the physical phenomenon, the design philosophies currently employed and under investigation are outlined.

Section 3 introduces the statistical basics to describe uncertainties in structural design. Furthermore, the usage of Bayesian statistics for the purpose of considering prior knowledge or expectation on a reliability based design approach is outlined.

The experimental work within this thesis is covered in section 4 and section 5. Section 4 is concerned with the quantification of uncertainties related to the stiffness evaluation of CFRP. Within section 5, uncertainties related to the characterisation of test cylinders on a micro and macro scale are determined and the details on the structural tests on the Hexapod test rig are given.

The data gathered in section 4 and section 5 is used in section 6 to analyse the model uncertainty of FE models using different input parameters. Additionally, the influence of the boundary conditions is analysed numerically comparing different modelling approaches varying in the level of detail.

In section 7 the data gathered on all uncertainties previously investigated is used to carry out a sensitivity analysis and identify relevant parameters to be further considered. These parameters are used for a number of Monte Carlo Simulations that represent different design stages, depending on the information available. Safety factors of the structural resistance are calibrated according to the resulting distribution functions. Furthermore, safety factors for the model uncertainty are derived through Bayesian updating of the mean model error term when compared to test results.

In section 8 the results are summarised and discussed.

2 State of the art

Unstiffened cylindrical lightweight structures are commonly used in the spacecraft industry as well as for primary structure of underwater vehicles. These structures are prone to buckling due to their comparably thin shell. Buckling occurs instantaneously and leads to the immediate collapse of the structure. The prediction of the load bearing capacity in axial compression has been subject to research efforts from the 1930s onwards both experimentally and analytically. Due to an ongoing discrepancy between experimental loads achieved and analytical prediction, the design approaches used for the design of these structures are still very conservative. The basics of buckling behaviour of unstiffened shells and the state of the art concerning the uncertainties related to the design are described in this chapter.

2.1 Buckling behaviour of unstiffened shells

Thorough descriptions of the process of buckling of unstiffened cylindrical shells under axial compression can be found e.g. in WIEDEMANN [Wie07], [Wie07] or SINGER AND ARBOCZ [Sin02].

A cylindrical unstiffened shell under axial compression load is schematically shown in Figure 2-1 and a typical load displacement curve for this load case in Figure 2-2.

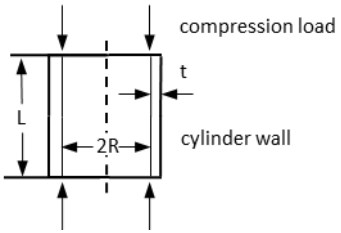

Figure 2-1 Axially compressed cylinder

During the first stage of loading the structure behaves linear elastic. The cylinder widens (barrelling effect) which results in the creation of hoop stresses around the circumference. Due to the clamping at the edges bending is restrained here, leading to additional transverse stresses (Figure 2-1). This effect is commonly neglected in the case of long cylinders.

The maximum point of the load displacement curve, denoted A in Figure 2-2, is the maximum load a perfect shell could sustain. However, many bifurcation points exist along the path between 0 and A. As the first bifurcation point is reached (point B in Figure 2-2) the structure buckles abruptly in a highly dynamic way during which the load bearing capacity rapidly decreases. Thus the difficulty is not to determine the limit load of the perfect shell at A, but to compute the first bifurcation point that determines the load bearing capacity of the structure at B.

In the presence of geometric imperfections this bifurcation point is characterised by a snap through behaviour that has been captured using high-speed cameras by ESSLINGER [Ess70], who shows that buckling starts with a single buckle. Later, HÜHNE [Hüh05] uses the high-speed Aramis system [GOM16a] to confirm her findings. By further increasing the displacement in a displacement controlled test setup, the structure reaches the postbuckling regime (path BD Figure 2-2).

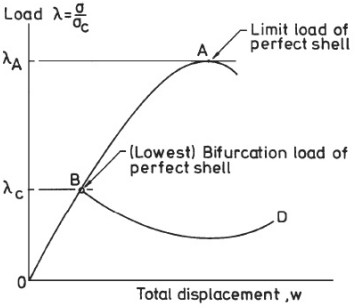

Figure 2-2 Buckling behaviour of cylindrical shell [Sin02]

When the structure buckles into the postbuckling regime the originally stiffening effect of the circumferential membrane forces diminishes. Hence, the load bearing capacity is far below the buckling load. ESSLINGER [Ess67] explains how already small geometrical imperfections lead to a reduced ability of the structure to develop circumferential membrane forces that could increase the load bearing capacity. In case of a force controlled structural loading, which is representative for real applications, the structure suffers catastrophic loss of load bearing capability without a stable postbuckling regime [Fri16].

One of the first attempts to develop design formulas to predict the buckling of such structures are simultaneously derived by LORENZ [Lor08], TIMOSHENKO [Tim10] and SOUTHWELL [Sou14]. Assuming a pure membrane stress state for the prebuckling range the buckling load for an isotropic shell can be written as

$$P_C = \frac{2\pi E t^2}{\sqrt{3\left(1-\upsilon^2\right)}}. \tag{2-1}$$

With E being the isotropic Young's modulus, t is the cylinder thickness and υ the Poisson ratio. Due to the large discrepancy found between computed buckling load and experimental result, DONNELL [Don34] develops a theory based on own experiments and those performed by LUNDQUIST [Lun34] that considers large deflections and initial imperfections in the form of a double harmonic series *w*.

$$P_C = \frac{Et^2}{12\,(1-\upsilon^2)}\nabla^8 w + \frac{E}{r^2}\frac{\partial^4 w}{\partial x^4} \tag{2-2}$$

$$w = W \sin\frac{2\pi x}{L_x}\sin\frac{2\pi s}{L_s} \tag{2-3}$$

At the time, no imperfection measurements had been performed, thus, amplitudes were chosen such that the computed buckling matched the test result [Kir89]. The theory by Donnell is commonly referred to as the classic theory.

An analytical solution for orthotropic shells is given by Wiedemann [Wie07] as

$$P_C = 2\times\sqrt{\left(\eta+\beta_{wmn}^2\right)/\left(\xi+\beta_{wmn}^2/\varepsilon\right)}\times\sqrt[4]{D_x D_y B_x B_y} \tag{2-4}$$

Here, in contrast to other notations, D_x and D_y are the in-plane stiffness parameters and B_x and B_y are plate stiffness parameters. ξ, η, ε and β are

$$\xi = \frac{\sqrt{D_x D_y}}{D_{xy}} \tag{2-5}$$

$$\eta = \frac{B_{xy}}{\sqrt{B_x B_y}} \tag{2-6}$$

$$\varepsilon = \sqrt{\frac{B_x D_y}{B_y D_x}} \tag{2-7}$$

$$\beta_{wmn}^2 = \left[\frac{\left(1-\varepsilon^2\right) + \sqrt{\left(1-\varepsilon^2\right)^2 + 4\left(\xi\varepsilon - \eta\varepsilon^2\right)\left(\xi\varepsilon - \eta\right)}}{2\left(\xi\varepsilon - \eta\right)} \right] \tag{2-8}$$

The usage of non-linear finite element methods relies on the application of geometric imperfections on the perfect cylinder geometry. Since these are not known in advance, usage is commonly made of the fact that the most unfavourable imperfection is one close to an eigenform of the cylinder. This leads to the practice of perturbing a nominal perfect geometry by a mixture of a number of eigenforms resulting from an eigenvalue analysis of a perfect cylinder (see e.g. [Arb01]). Each eigenform is asserted certain amplitude that is scaled with the thickness of the cylinder. The choice of these amplitudes is a very critical design choice that can lead to a wide range of results. Certain knowledge of the imperfections expected is hence necessary.

From the mid-30s to 60s, a large amount of tests is performed by different institutions on metallic cylinders. A comparison of the available test data at the time is given by WEINGARTEN [Wei65a] and reveals a tendency of decreasing load capacity with increasing radius to thickness ratio R/t (Figure 2-5, page14). Despite the many tests that are analysed for that study, no direct comparability is possible. The investigators use different materials, cylinder configurations and test set-ups, resulting in varying boundary conditions that are not always clear or reproducible [Sin02]. Hence, it is not possible to apply a statistical analysis that would reveal information on uncertainties and a reliability level of the structures.

2.2 Influences on predictive uncertainty of buckling load

2.2.1 Geometrical imperfections

KOITER describes in 1945 the close relation between geometrical imperfections of a cylindrical shell and the observed reduced buckling load compared to the theoretical prediction. However, his work is recognized only later when translated into English [Koi70]. Koiter considers imperfections as double Fourier series and shows how important the realisation of the geometric imperfections is for the prediction of a load reduction factor. His findings had a high impact on the research community in so far, as up to then only few research institutes made the effort of surveying the complete cylinder surface and storing this data – commonly, only the maximum amplitude was recorded [Sin02]. At the end of the seventies, surface measurements become widely

used through taking measurements at regular grid points. The patterns found are then stored as corresponding Fourier coefficients.

Comparing Fourier and Power spectra of metallic shells [Arb91] and composite shells [Hil06], [Sch15] confirms findings by [Chr95] that composite shells tend to longer waved imperfection modes as compared to metallic shells. This is probably due to local application of heat on metal cylinders during welding. This fundamental difference makes the material and manufacturing related data base necessary to calibrate knock-down factors.

Testing of CFRP cylinders commonly concentrated on the investigation of the influence of the layup. Thus, only few studies are concerned with creating a statistical database. CHRYSSANTHOPOULOS AND POGGI [Chr95] investigate 16 nominally identical unstiffened cylindrical shells with symmetric cross ply laminate $[0/90]_S$ and 14 nominal identical shells with $[+/-45]_S$ layup. Using a sensing element, the out of plane deviation is measured at grid points with a grid size of 10 mm x 20 mm. Fourier decomposition is then used to approximate the geometric imperfection pattern and is used for its statistical characterisation. Outer as well as inner contour is measured. A high correlation of long-waved modes is identified but only a very small number of short-waved modes are found on the inner contour compared to the outer contour. The appearing short-waved modes on the outer surface could be associated to local thickness variations due to overlapping layers. It is hence concluded, that the imperfection pattern on the outer surface is not representative for the geometric imperfection pattern and instead the measurements of the inner surface are used for further analysis.

HILBURGER ET AL [Hil06] use six CFRP cylinders with varying layups and measure the geometric imperfection in a regular grid of size 0.125 inch x 0.139 inch. For one cylinder with nominal thickness 1.016 mm information about the geometric imperfection is given. The pattern shows no waviness in axial direction, the amplitude ranges from 1.29 mm to – 1.56 mm.

The maximum imperfection amplitude of three of the 10 nominal identical CFRP cylinders tested by DEGENHARD ET AL [Deg10] are given by CASTRO [Cas14]. The amplitudes presented are 0.63, 0.71 and 0.63 mm, whereas the nominal thickness is 0.5 mm.

HÜHNE [Hüh08] gives the unwound plot for cylinder Z11 that shows maximum amplitude of around 1 mm. The nominal thickness is 0.5 mm.

2.2.2 Boundary conditions

An analytical prediction for the influence of boundary conditions was derived by e.g. HOFF [Hof66] and THIELEMANN and ESSLINGER [Thi64]. The predicted reduction of up to 50 % is later corrected by ALMROTH [Alm65] by considering radial constraints apparent

in the experimental setup to 20 %. Despite this conclusion, no stringent parameter study has been carried out to investigate these findings. WEINGARTEN [Wei65a] asserts through comparison of data found in literature, that the usage of Cerrolow, a low melting bismuth based alloy, yielded consistently higher buckling loads of Mylar cylinders than those bedded in Cerrobend. The difference in these alloys lies mainly in the coefficient of thermal expansion. For Cerrolow, this coefficient is slightly negative and positive for Cerrobend. However, further quantification of this effect is difficult since the influence of the boundary conditions is also dependent on geometry and structural stiffness of the cylinder.

Boundary conditions are still being suspected of being responsible for some part of the remaining discrepancy between simulation and test [Arb79], [Deg10].

2.2.3 Material characterisation

Commonly, material properties are measured in coupon tests and the resulting stiffness and strength data is used for the structural design of the component. For structures made of fibre reinforced plastics, the representation of laminate properties in situ through coupons is not equally straightforward. In contrast to metal structures, where material that has already been made is used for the structure and the coupons, the FRP is made together with the structure and can differ in its manufacturing process from the coupon.

Furthermore, the hierarchical structure of fibre composites leads to uncertainties on different scales of the structural behaviour [Cha04]. Theoretically, uncertainties on a lower scale are present on higher scales. But in structural design, usually the lowest scale considered is the ply or coupon level. On this level material properties are measured, rather than measuring fibre and matrix properties separately. Considering a multiscale approach from the ply level on, one now has to consider that uncertainties on coupon level are not necessarily the same as on component level.

On the coupon level it is well known that property measurements are strongly related to the testing method [Sch05], the preparation of the probe [Har00], [Lav00], layup [Har00] [Jac92] and edge treatment. For example, this sensitivity is among others due to arising edge effects, which generally are not or not that distinctly present in the structural component. On the structural scale, the component is more prone to manufacturing related uncertainties like complexity of the structure, contours or type of process [Pot01].

The above described factors can be very specifically related to preparation and test procedure for certain material batches. DEGENHARDT ET AL[Deg10] [Deg10] undertake coupon testing of three different batches of a nominal identical Prepreg system and measure a maximum difference of 17 % between mean values of axial stiffness.

In order to determine and quantify uncertainties related to axial stiffness measurements of CFRP laminates, a detailed study is carried in section 4.

2.2.4 Manufacturing method

HIPP AND JENSEN [Hip92] investigate the influence of manufacturing parameters of wound cylinders. Especially the role of the winding pattern and the number of layer crossings and accompanying interface changes is considered. During buckling tests, it is found that overall buckling is initiated through local buckling at layer crossings. The stiffness of the cylinders decreases with increasing number of crossings. The cylinders reach 58-75% of the buckling load predicted by finite element analysis.

A very systematic investigation of the influence of manufacturing parameters is performed by HAHN ET AL [Hah94]. Cylinders with varying layup get analysed on the microscale (fibre volume fraction, void content) as well as on the macroscale (thickness variation, geometric imperfections) and its influences on the load carrying capacity are studied. Further focus lies on the influence of the layup pattern which leads to local crossings of the layers. A very illustrative visualisation is given and reproduced in Figure 2-3.

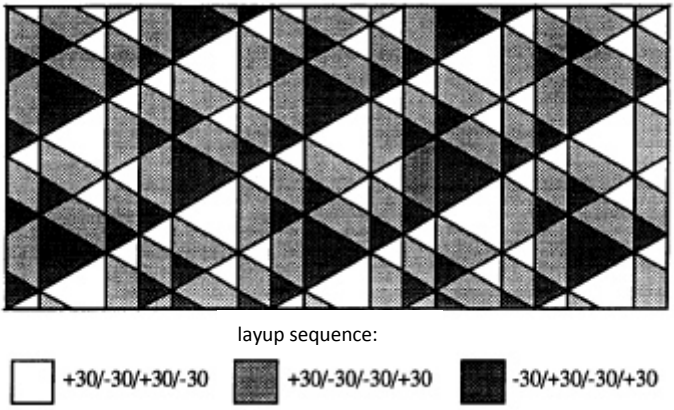

Figure 2-3 Layup changes due to winding pattern of an unwound cylinder [Hah94]

The influence of geometric imperfections and non-membrane pre-buckling deformations amounts to 10% of the overall buckling load. Additional 10 % get ascertained to the changing coupling terms of the ABD-stiffness matrix due to layup crossings. Depending on distance and number of layup crossings, a buckling load increase of up to 20 % is found for the densest configuration. The crossings do not influence the buckling mode itself, but the position of buckles and the propagation of damage.

A further result of this study is the high coincidence of the FE model with test result whereas in the model a geometric imperfection was generated by introducing a thermal load representing the cool down process during curing. The following eigenvalue analysis leads to a buckling load that differs only by 5 % from the measured buckling load.

A close relationship between the number of bifurcation points in the vicinity of the buckling load and the quality of manufacturing is also suggested by ESSLINGER [Ess69].

2.2.5 Load imperfections

To investigate the sensitivity of unstiffened cylindrical shells against a non-uniform stress state, GEIER AND ZIMMERMANN [Gei91] carry out so-called shim tests. A shim is inserted at varying positions in circumferential direction between cylinder and load introduction. This procedure is repeated for several CFRP cylinders with varying layup. The experiments reveal that certain layups show a high scatter and hence sensitivity with respect to the buckling load while other layups show only small variations in the buckling load. GEIER AND ZIMMERMANN deduce that the latter cylinders are more robust against geometrical imperfections, while ZIMMERMANN [Zim92] later also suggests that smaller or larger geometrical imperfections might be responsible for the differences.

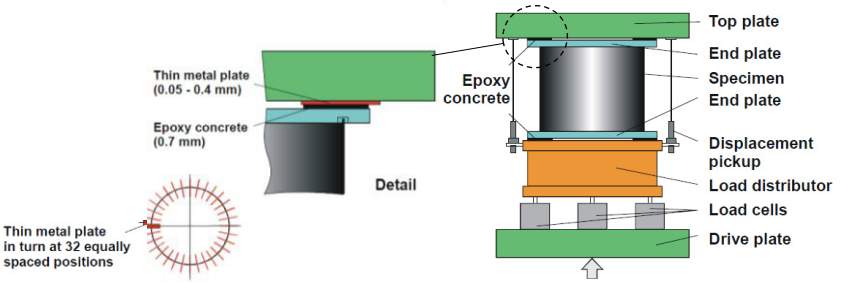

Figure 2-4 Test set up with shims, from [Hüh02]

The experiments show that a high dependence between the imperfection pattern and the orientation of the load eccentricity can occur. For one shell data regarding all 32 positions of the shim are published and show a difference of minimum to maximum buckling load of 37 % [Zim96]. HÜHNE [Hüh05] later repeats the experiments with different shells. Depending on shim size and position, the buckling load reduces by a maximum of 9 % and 27 % for a 0.2 mm and 0.4 mm thick shim, respectively, which implies a high sensitivity towards load imperfections.

A similar behaviour is later found by KRIEGESMANN [Kri12a] who assumes a load imperfection consisting of a tilted load introduction, thus introducing an inhomogeneous

stress state. He computes the inclination angle for different positions of the cylinder and achieves a good agreement with cylinders tested by HÜHNE [Hüh05] for an inclination angle of 0.009° which effectively decreases the buckling load by about 17% as compared to no assumed load imperfection.

2.2.6 Stacking sequence

The sensitivity of the buckling load towards the stacking sequence is recognized by CARD [Car69] and further investigated by GEIER ET AL [Gei02]. Geier analyses two cylinder types for which the stacking sequences are reversed and gives explanations for the varying buckling loads based on the Poisson ratio of ply packages that can amplify or reduce the buckling load depending on their position in the laminate. These effects are commonly not covered by analytical solutions that are only valid for orthotropic laminates since they do not account for all terms of the stiffness matrix. A further case of cylinders with reversed stacking sequence has been investigated by HÜHNE [Hüh05] and KRIEGESMANN [Kri12a].

2.3 Remaining discrepancies between tests and computation

CHRYSSANTHOPOULOS ET AL. [Chr95] test 30 Kevlar fabric cylinders with two different layups made by hand layup. For sixteen of them, which consist of a symmetric +/-45° layup, finite element analyses are carried out considering the measured imperfections. The analysis overestimates the buckling load by 13-31%.

Within the European research project “Design and Validation of Imperfection-Tolerant Laminated Shells” (DEVILS), nine cylindrical shells are tested under axial compression at the German Aero-space Centre (Deutsches Zentrum für Luft- und Raumfahrt, DLR) in Braunschweig [Gei91]. Seven different, asymmetric layups are used and buckling loads computed using the analytical DLR tool Baccus with different boundary conditions as well as a finite element code. Deviations to the measured buckling loads vary between 8-30% in the case of Baccus4 and between -16 to 13 % for the FE implementation [Mey01].

HILLBURGER AND STARNES [Hil04] investigate six cylindrical CFRP shells with varying layup. Three of the cylinders failed due to buckling, deviation to buckling failure prediction of a corresponding perfect shell varies between 7 % and 17 %. BISAGNI [Bis99] tested 16 composite cylinders with 6 different layups. For one of these cylinders a finite element analysis using two different methods and including the measured imperfections was performed. The numerical result overestimated the observed testing value by 15-20%.

HÜHNE [Hüh05] computes buckling loads for the same set of cylinders using the commercial software tool Abaqus. His results deviate from the buckling loads tested and published by [Mey01] between 4-30%.

Ten nominally identical CFRP cylinders have been tested at DLR by DEGENHARDT ET AL. [Deg10]. Within a project funded by the European Space Agency (ESA) the cylinders were tested and showed a coefficient of variance of buckling loads of 5.5%. Broggi [Bro11] computes buckling loads for each of these cylinders using non-linear FE models and includes geometric imperfections as well as thickness variations. Both models overestimate the buckling load by 15-43%.

2.4 Design philosophies

2.4.1 NASA SP 8007

NASA SP 8007 is a guideline for design of unstiffened shells under different loading conditions. The analytical solution for computation of the buckling load is based on a simplification of the classic theory suggested by BATDORF [Bat47] and an extension for orthotropic shells by JONES [Jon68]. All possible imperfections or uncertainties are covered through a global knockdown factor.

The basis of this knockdown factor is the test data mentioned earlier that was summarised and compared by WEINGARTEN [Wei65b] [Wei65a]. The test results he retrieves from literature are reproduced in Figure 2-5. On the horizontal axis the R/t ratio of the cylinders is depicted while on the vertical axis the ratio of computed buckling load to test result is shown.

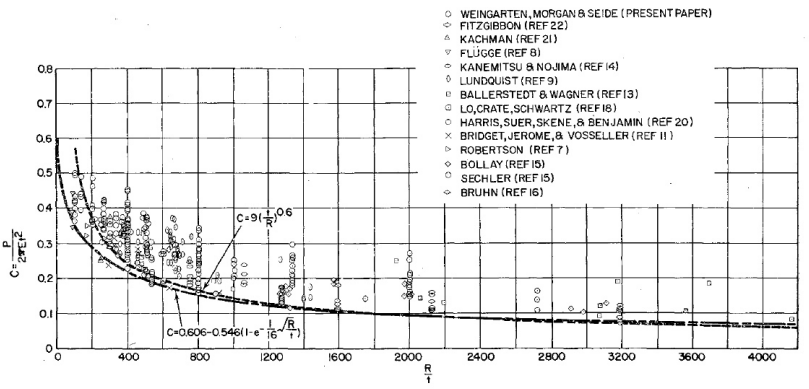

Figure 2-5 Knock-down factor curve used for NASA SP [Wei65a]

The curve shown in Figure 2-5 is the basis of the safety concept used for the NASA SP-8007 guideline for design of unstiffened shells under axial compression ([Wei65b], [Pet68]).

As outlined in section 2.1, the test data cannot be analysed statistically since different boundary conditions, materials and test set ups have been used. Hence, an equation to determine a conservative knockdown factor γ depending on the R/t ratio was developed that lies below all test data analysed and is computed as

$$\gamma = 1 - 0.901\left(1 - e^{-\phi}\right) with\ \phi = \frac{1}{16}\sqrt{\frac{R}{t}} \tag{2-9}$$

For orthotropic shells the exponent is modified using

$$\phi = \frac{1}{29.8}\sqrt{\frac{R}{t^*}}\ \ with\ t^* = \sqrt[4]{\frac{D_x D_y}{E_x E_y}} \tag{2-10}$$

E_x and E_y are the in plane stiffness parameters, D_x and D_y the plate stiffness parameters. Using the buckle aspect ratio β

$$\beta = \frac{nL}{m\pi R} \tag{2-11}$$

with m being the number of buckle half waves in axial direction and n being the number of buckle waves in circumferential direction, the buckling load for orthotropic shells is given as

$$N_x = m^2\left(1 + 2\frac{\overline{D_{xy}}}{\overline{D_x}}\beta^2 + \frac{\overline{D_y}}{\overline{D_x}}\beta^4\right) + \frac{\gamma^2 L^4}{\pi^4 m^2 \overline{D_x} R^2}\frac{\overline{E_x}\,\overline{E_y} - \overline{E_{xy}}^2}{\overline{E_x} + \left(\frac{\overline{E_x}\,\overline{E_y} - \overline{E_{xy}}^2}{\overline{G_{xy}}} - 2\overline{E_{xy}}\right)\beta^2 + \overline{E_y}\beta^4} \tag{2-12}$$

Note the appearance of γ square in the numerator.

The recommendations of the NASA SP-8007 do also apply for cylinders made of fibre reinforced plastics. Notably, the previously mentioned influence of the coupling terms of the laminate stiffness matrix, further investigated by GEIER ET AL [Gei02], cannot be captured.

Also, none of the cylinders depicted in Figure 2-5 is made of FRP. Although some CFRP cylinders are later tested and the buckling loads are compared to the design loads given by the NASA SP, it is only concluded that the approach leads to very conservative

results (see e.g. [Deg10]). There is however not enough statistical meaningful data to determine the real inherent safety of the structure designed using this approach.

2.4.2 Single perturbation load approach (SPLA)

Based on findings by ESSLINGER [Ess70] that the collapse is initiated at a single buckle, HÜHNE [Hüh05] develops a design concept called single perturbation load approach (SPLA) which incorporates the usage of a transverse point load on the outer cylinder surface using finite element analysis. The idea is that this point load triggers the first buckle and hence allows for the computation of conservative load estimation. Hühne performs a parameter study concerning the amplitude of the transverse load and finds that above a certain load level, the computed buckling load does not further decrease.

The point load is applied during an initial load step within the finite element analysis. During the second load step, the axial compression load is applied. The design load is then computed via a non-linear FEA. Hence, a global knockdown factor with respect to a perfect cylinder can be found without further knowledge about manufacturing uncertainties.

In some cases the computed design load exceeds the buckling load observed in experiments [Hüh05]. The SPLA is hence further investigated within the framework of the EU-project DESICOS (New Robust Design Guidelines for Imperfection Sensitive Composite Launcher Structures, www.desicos.eu). It is found to be conservative in terms of covering possible geometric imperfections [Kri12b].

2.4.3 Probabilistic approach

Probabilistic approaches for the design of unstiffened shells were first proposed by BOLOTIN [Bol62] and later picked up by others [Fra69], [Roo69].

ELISHAKOFF AND ARBOCZ analysed cylindrical shells by considering the Fourier coefficients used to approximate the geometric imperfections as random variables within an analytical framework [Eli82], [Eli87]. However, no statistical data base for comparison with real cylinders was available. In order to validate the procedure, 30 beer cans are measured and tested at the TU Delft [Arb79]. A comparison of the resulting probability density functions shows no good agreement and it is concluded that not all uncertainties are accurately represented in the model.

SCHENK AND SCHUELLER [Sch03] consider random geometric imperfections of 7 copper electro-plated, isotropic cylindrical shells referred to in [Arb79] and generate artificial geometric imperfections by applying a Karhunen-Loeve expansion to generate eigenfunctions with uncorrelated random variables [Sch01]. The standard deviation of the

resulting simulation compares reasonably well with the standard deviation of the test results.

CHAMIS AND ABUMERI [Cha05] perform Monte Carlo simulations treating ply thickness, fibre volume ratio and fibre longitudinal modulus as random variables. No geometric imperfections are considered. Static and dynamic analyses are compared but no comparison to test results is possible.

DEGENHARDT ET AL. [Deg10] carry out Monte Carlo simulations and treat material parameters probabilistically. The resulting probability density function does not match the test result.

BROGGI ET AL. [Bro11] use the measurements taken by DEGENHARDT to perform new Monte Carlo simulations. Here, the focus is on generating artificial, representative geometric imperfection patterns by using random fields. Evolutionary power spectra are used to capture the statistical properties of the random field. The method leads to good agreements for the torsional load case. For axial compression it is found that not all uncertainties are captured in the model.

KRIEGESMANN [Kri10] performed Monte Carlo analysis for the cylinders tested by HÜHNE [Hüh08] and considers geometric imperfections as well as boundary imperfections as random variables. The probabilistically derived lower bounds were conservative with respect to the test results but less conservative than the NASA SP. Due to the small sample size, the results could not be validated. Later, KRIEGESMANN applies an extension of the semi-analytic approach suggested by ELISHAKOFF AND ARBOCZ [Eli82], [Eli87] to the set of shells tested by DEGENHARDT ET AL. [Deg10]. Good approximations of the probability density function of the test results are found for both the semi-analytic as well as the Monte Carlo simulation.

BIAGI AND DEL MEDICO [Bia08] derive reliability based knock-down factors by statistically analysing so-called ‘equivalent imperfection amplitudes’. The procedure consists of computing the collapse load of the imperfect shell for different imperfection amplitudes with an in-house code, which includes a characteristic imperfection shape that is used to derive equivalent imperfection amplitude corresponding to the collapse load measured during the experiment. These equivalent imperfection amplitudes are computed for cylinder tests found in literature and lead to a statistical distribution that is used as input for a Monte Carlo simulation. From these simulations, a knockdown factor can be computed in accordance with a target reliability level. The method relies on using one characteristic imperfection shape for all cylinders considered.

2.5 Contribution to open research questions

Although the spacecraft industry performed a large amount of cylinder tests, especially in the 1930's to 1970's, there is only very few available data on CFRP cylinders. Representative tests are necessary since the manufacturing method and type of material differ in the generation of geometric imperfections that can have a large influence on the buckling behaviour. For composite cylinders, research has frequently been focused on the variation of layups. Consequently, only few institutes have tested a statistical meaningful set of identical cylinders which is the necessary basis for the development of a reliability based design concept (see Appendix A1 for an overview of tested CFRP cylinders with geometrical data and layups). Figure 2-6 depicts the CFRP cylinders found in literature with their R/t ratio against the number of specimens per layup. Only two research groups, BISAGNI et al. [Bis99],[Bis03] and GEIER [Gei91]and MEYER-PIENING ET AL. [Mey01] tested four cylinders of the same layup. DEGENHARDT [Deg10] tested 10 cylinders with identical layup with a R/t of 545. The layup was chosen to be [+24/-24/+41/-41]. Due to high slenderness and structural elastic behaviour, it is possible to load the cylinders repeatedly. The cylinders tested by SCHILLO [Sch15] are characterised through a lower R/t value of 147. They are the only set of cylinders with eleven specimens that consist of a quasi-isotropic layup, representing structural applications.

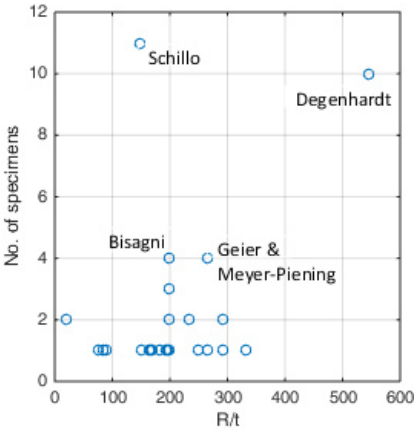

Figure 2-6 Number of identical CFRP cylinders tested with certain R/t

Despite advanced techniques in measuring the geometrical imperfections and their consideration in finite element models, a considerable discrepancy between test and model result remains. Among the parameters that could explain those discrepancies are the spatial variability of material and structural parameters, the usage of simplified boundary conditions and negligence of load imperfections.

Within this thesis, load imperfections are explicitly measured using a 6 degree of freedom load cell for the first time. Also, the influence of the pre-stress state generated through the mounting process has not been quantified yet numerically and is addressed in section 6.1.6.

The advantage of a reliability based design approach is to be able to design against a chosen realiability level. But knowledge about all relevant scattering design parameters is vital, leading to high measurement costs. Thus, necessary information may often not be available, especially in early design stages. In the following sections, the results of extensive measurements regarding material, structural and testing uncertainties are presented. Using Bayesian updating, this information can also be used in cases where similar structures are designed.

3 Uncertainties and sensitivities in structural design

The following sections recall some basics regarding classification of uncertainties and their treatment in structural design. A brief introduction to Bayesian statistics is given that is vital for the methodical approach to develop safety factors in section 7.

3.1 Identifying uncertainties

Uncertainties regarding structural design are commonly categorized as either *aleatoric* or *epistemic* uncertainties [Ayy11]. Aleatoric uncertainties refer to system inherent uncertainties that characterise that quantity like for example the scatter of some material property. These uncertainties just happen to be there and may or may not be relevant for the analysis. Epistemic uncertainties are those that are due to a lack of information. This may be because a quantity is not sufficiently accurately measured or because the computational model neglects certain effects. These uncertainties can in principal be reduced by increasing the experimental or modelling effort.

3.1.1 Characterising uncertainties

In order to characterise the uncertainty of a quantity the data can be described in various ways. A full description is given through the probability mass function (PMF) in case of discrete values or the probability density function (PDF) in terms of a continuous quantity. These functions give the probability p that a random variable takes certain values. Figure 3-1 shows examples for a PMF and PDF for a variable denoted x.

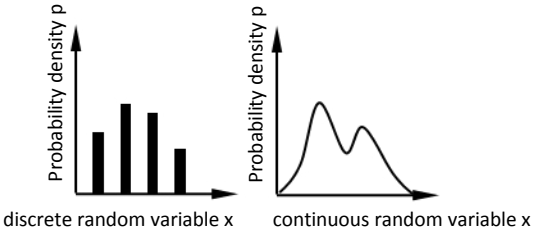

Figure 3-1 PMF (left), PDF (right)

A common way to analyse data in terms of uncertainty is to analyse the *moments* of the PMF or PDF. The first moment is the expected value or the mean and for a random variable *X* is defined as

$$E[X] = \mu_X = \sum_x x p_X(x) \tag{3-1}$$

$$E[X] = \mu_X = \int_{-\infty}^{\infty} x f_X(x) dx \tag{3-2}$$

The second most important quantity associated with a random variable *X* is its variance. It provides a measure of the dispersion around the mean and is defined as follows:

$$\mathrm{var}(X) = E\left[(X - E[X])^2\right] = \sum_x (x - E[X])^2 p_X(x) \tag{3-3}$$

$$\mathrm{var}(X) = E\left[(X - E[X])^2\right] = \int_{-\infty}^{\infty} (x - E[X])^2 f_X(x) dx \tag{3-4}$$

The dispersion can also be expressed through the *standard deviation* σ, which is defined as the square root of the variance:

$$\sigma = \sqrt{\mathrm{var}(X)} \tag{3-5}$$

A common way to characterise the dispersion in a normalised way is to provide it through the *coefficient of variation* (COV), which is defined as

$$COV = \frac{\sigma_X}{\mu_X} \tag{3-6}$$

3.1.2 Distribution functions

In many cases in structural design, the probability density function of a random variable can be described by a normal distribution. This is usually justified be the central limit theorem, which states that the expected value of a sufficiently large number of iterates of independent random variables, each with a well-defined expected value and well-defined variance, will be approximately normally distributed, regardless of the underlying distribution (refer to e.g. [Ber08]).

The PDF of a normal variable *X* is written as

$$f_n(x) = \frac{1}{\sigma\sqrt{2\pi}} e^{-\frac{1}{2}(\frac{x-\mu}{\sigma})^2} \tag{3-7}$$

Another commonly used distribution function is the lognormal distribution. A random variable *X* is lognormal distributed if the logarithm of *X* is normally distributed:

$$f_{\log}(x) = \frac{1}{x\sigma\sqrt{2\pi}} e^{-\frac{1}{2}(\frac{\log(x)-\mu}{\sigma})^2} \tag{3-8}$$

where μ and σ are the mean and standard deviation, respectively, of the associated normal distribution. Normal and Lognormal distributions are closely related. If *X* is distributed lognormal with parameters μ and σ, then *log(X)* is distributed normally with mean μ and standard deviation σ. The mean *m* and variance *v* of a lognormal random variable are functions of μ and σ:

$$m = \exp\left(\mu + \frac{\sigma^2}{2}\right) \tag{3-9}$$

$$v = \exp\left(2\mu + \sigma^2\right)\left(\exp\left(\sigma^2\right) - 1\right) \tag{3-10}$$

The lognormal distribution is applicable when the quantity of interest must be positive, since log(X) exists only when *X* is positive.

A very useful property of the lognormal distribution is that the sum of two lognormal distributed variables is also lognormal distributed. Suppose *X* and *Y* are two lognormal distributed variables and *Z*=*X* x *Y*, then

$$\log(Z) = \log(X) + \log(Y) \tag{3-11}$$

This property is the reason why lognormal distributions are often used to model multiplicative error models [Fab02].

3.1.3 Correlation analysis

A measure to determine the dependence among uncertain quantities is the correlation coefficient ρ. It measures the degree to which an uncertain quantity varies linearly with another uncertain quantity. It is defined as the ratio of the covariance (Cov) of the quantities *x* and *y* to the square root of the product of the variances of *x* and *y*:

$$\rho_{xy} = \frac{Cov(x,y)}{\sqrt{\mathrm{var}(x)\,\mathrm{var}(y)}} = \frac{E\left[(x-\mu_x)(y-\mu_y)\right]}{\sqrt{\left[E\left[(x-\mu_x)^2\right]\right]\left[E\left[(y-\mu_y)^2\right]\right]}} \tag{3-12}$$

The correlation coefficient varies between -1 and +1 with the higher bound representing a linear relation of positive slope while negative value implies a negative linear relation of negative slope. The higher the magnitude, the higher the dependence of the quantities and degree with which the quantities vary together. Zero correlation implies no linear association between *x* and *y* although a non-linear dependence might still exist.

In case a certain degree of association is suspected among one quantity with itself over space, the so called autocorrelation can be computed as:

$$\rho = \frac{Cov(z_1,z_2)}{\sqrt{\mathrm{var}(z_2)\,\mathrm{var}(z_2)}} = \frac{1}{\sigma_1\sigma_2} E\left[(z_1-\mu_{z1})(z_2-\mu_{z2})\right] \tag{3-13}$$

The degree of linear association can then be measured as a function of separation distance.

3.2 Identifying sensitivities

The purpose of a screening method for identifying the sensitivity of a model response towards scatter of input parameters is to reduce the relevant sample space. If the scatter of an input parameter has a large influence on the model response, this scatter should be considered for the analysis. If the scatter of the parameter turns out to be negligible it can be treated deterministically.

Local Methods

A local analysis addresses sensitivity relative to point estimates of parameter values. Variables or parameters under investigation are varied one at a time by a small amount around some fixed point and the effect on the output is calculated. Thus, these methods are commonly derivative based and assume linear relationships.

Global Methods

A global analysis examines sensitivity with regard to the entire parameter distribution. All variables or parameters are varied simultaneously over their entire feasible space, typically using a sampling based approach. The effects on the output of individual variables/parameters as well as interactions between them are assessed. These methods are employing regression methods, are variance-based and can be computationally demanding.

Morris Screening

This screening method proposed by Morris [Mor91] aims at combining the advantages of simplicity and speed of local methods in a global context. In contrast to local methods it is not restricted to linear relationships. It also does not rely on assumptions regarding relative sparsity of important inputs as well as monotonicity with respect to the inputs.

The evaluation of sensitivities is performed by analysing so-called *Elementary Effects* (EE). An elementary effect describes the change in the output variable when one of the input parameters is perturbed in a methodical way that will be described shortly. Θ_1 to Θ_k represent the input parameters and Δ the perturbation coefficient. The *EEi*s are defined through

$$EE_i^r = \frac{y(\Theta_1^r, \Theta_2^r, \Theta_i^r + \Delta, \ldots, \Theta_k^r) - y(\Theta_{ref})}{\Delta} \tag{3-14}$$

where *r* stands for the number of repetitions chosen for the sampling and $y(\Theta_{ref})$ is the model response of the reference configuration of all input parameters belonging to the *r*-th repetition.

To generate the sample space, firstly the number of repetitions *r* and the perturbation level *p* need to be chosen. The perturbation level describes the number of levels across which the perturbation factors x_i are varied. It hence defines the grid spacing of the k-dimensional parameter space. Each x_i may take values from {0, 1/(1-p), 2/(1-p),…1}. It can be shown that the optimum choice of the perturbation coefficient Δ is given for [Mor91]

$$\Delta = \frac{p}{2(p-1)} \tag{3-15}$$

The randomization process described in Appendix A2 is utilised to define a set of perturbation factors x_i for each repetition *r*. Additionally, the perturbation range used can be influenced by some prior believe about the uncertainty of the parameter. This factor

unc is set to a value between 0 and 1, with 0 describing no uncertainty and 1 a maximum of uncertainty. A lower and upper bound for the parameter variation is then computed through

$$b^{low} = \Theta^{ref}\,(1 - unc)$$
$$b^{up} = \Theta^{ref}\,(1 + unc) \tag{3-16}$$

These bounds are used to scale the perturbation factors x_i^r resulting from the randomization process

$$\Theta_i^r = b^{low} + (b^{up} - b^{low}) \cdot x_i^r \tag{3-17}$$

Having defined the randomized and scaled parameter space, the mathematical model is run *r* x (*k+1*) times and the elementary effects are computed using Equation (3-14). For each parameter, the corresponding distribution of EEs resulting from the number of repetitions is evaluated in terms of their mean and standard deviation (Equations (3-1) and (3-2)).

3.3 Treatment of uncertainties in design philosophies

The question what safety means and how it is treated in structural design is addressed in DIN 1055-100 [DIN01] (refer to Table 3-1) and here, the safety concepts are categorized into five levels from which the first four, that do not account for economic data, are further described below.

Table 3-1 Classification of safety concepts according to DIN [DIN01]

Concept	Level	Safety measure	Method
Deterministic	0	Global safety factor ν	Empirical methods
Semi-probabilistic	1	Partial safety factors γ	Limit state, calibration
Probabilistic approximate	2	Safety index β	Method of moments, FORM, SORM, response surface
Probabilistic 'precise'	3	Probability of failure P_f/ probability of survival P_S	Monte Carlo, numerical integration
Economical optimal	4	Allowable probability of failure / allowable safety index	Optimization methods considering economic data, using methods from level 2 and 3

Level 0: Deterministic safety concept

On level 0, the problem is analysed in a purely deterministic way. Design variables are treated as certain fixed values resulting in a deterministic design. Any uncertainty that might be present is considered by a global safety factor υ, leading to an allowable stress σ_{all} of

$$\sigma_{all} \geq \sigma_{act} \cdot \upsilon \tag{3-18}$$

where σ_{act} is the stress acting on the structure. This global safety factor is determined empirically and commonly results from prior experience with similar structures. The global safety factor is adjusted in case failures are observed.

Level 1: Semi-probabilistic safety concept

The semi-probabilistic approach is the most widely applied one in structural engineering and is described in detail in EN 1990 [EN 02]. The allowable is computed by multiplication of several partial safety factors γ_n, accounting for uncertainties related to different sources

$$\sigma_{all} = \sigma_{act} \cdot \gamma_1 \gamma_2 \gamma_3 .. \gamma_n \tag{3-19}$$

Each γ represents an influence that might decrease the load carrying capacity to a varying amount. For example in the case of a fibre reinforced structure, γ_1 might consider an influence of temperature while γ_2 reduces the allowable stress depending on the manufacturing process, since a winding process achieves better material properties than a hand layup. The partial safety factors are determined either through empirical calibration or through simple probabilistic methods, e.g. through level 2 methods.

In the latter case, the random variables are first transformed to a standard normal distribution with zero mean and standard deviation of one using the following relation:

$$x_i^* = \frac{x_i - \mu_{xi}}{\sigma_{xi}} \tag{3-20}$$

For a given target reliability index β_T, partial safety factors to provide that reliability can be computed through [Bae03]

$$\gamma_i = \frac{x_i^*}{E[x_i]} \tag{3-21}$$

In which γ_i is the partial safety factor for the variable x_i and x_i^* is the value of the transformed variable x_i at the design point.

Level 2: Probabilistic approximate safety concept

The probabilistic approximate approach is widely used in civil engineering praxis. Here, an allowable safety index β is defined which depends on the application of the structure and the consequences of failure (economic loss, loss of life, etc.). The basis of the computation of the safety index is the knowledge of some statistic properties of the load and resistance parameters. These are represented through their first and second moments, the mean and variance.

The first order reliability method (FORM) uses the information about first and second moments of the input variables. It facilitates a Taylor series expansion about the mean values of the basic random variables. The series is truncated at the first-order terms, namely the first order approximate for the mean and for the variance of the performance function *g*

$$\mu_g \approx g(\mu_{x1}, \mu_{x2}, \ldots, \mu_{xn}) \tag{3-22}$$

$$\sigma_g^2 \approx \sum_{i=1}^{n}\sum_{j=1}^{n}\left(\frac{\partial g}{\partial X_i}\right)_{\mu}\left(\frac{\partial g}{\partial X_j}\right)_{\mu} Cov\left(X_i, X_j\right) \tag{3-23}$$

The reliability index β can then be defined as

$$\beta = \frac{\mu_g}{\sigma_g} \tag{3-24}$$

If *g* is assumed to follow a normal distribution, the probability of failure P_f is given by Equation (3-26).

If μ_R and σ_R are the mean and standard deviation of the resistance of the structure, and μ_S and σ_S the mean and standard deviation of the load level, β is calculated as

$$\beta = \frac{\mu_R - \mu_S}{\sqrt{\sigma_R^2 - \sigma_S^2}} \tag{3-25}$$

A graphical interpretation of this value is given in Figure 3-2.

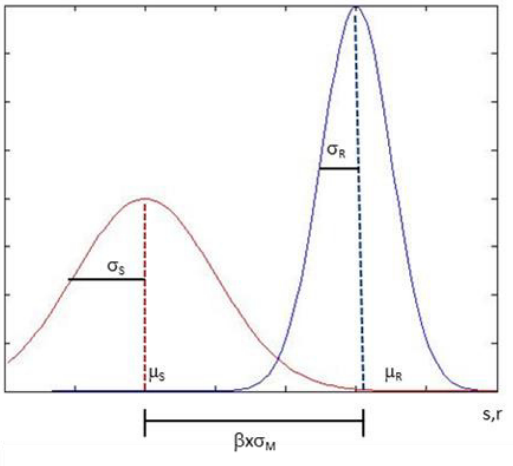

Figure 3-2 Graphical interpretation of the safety index β

The relation between the probability of failure P_f and the safety index β can then be written as

$$P_f = 1 - \Theta(\beta)$$
$$\Theta(\beta) = \frac{1}{\sqrt{2\pi}} \exp\left(-\frac{\beta^2}{2}\right) \tag{3-26}$$

In which Θ is the cumulative probability distribution function of the normal standard variate.

While on level 2 the first two moments are considered, level 3 considers the complete distribution function that describes each uncertainty. In doing so, it is admitted that all design variables consist of some kind of uncertainty represented through a distribution function. Since a scatter is also attributed to the load applied, the distribution functions of the load and resistance of the structure will overlap at a certain degree, indicating a positive value for the probability of failure.

Level 3: Probabilistic precise safety concept

On level 3, the probabilistic 'precise' safety concept is employed. Monte Carlo (MC) simulation techniques estimate the probabilistic characteristics of a functional relationship. For this purpose direct simulations are performed by drawing samples of the basic variables according to their probabilistic characteristics and feed them into the function under consideration. This function may be analytical or a finite element model. An estimate of the resulting probability of failure is

$$P_f = \frac{N_f}{N} \tag{3-27}$$

Where N_f is the number of simulations giving a negative result for the performance function and N being the total number of simulations.

Level 4: Economical optimal

The fourth level of the classification additionally incorporates economic data for the optimization process. These methods have not been considered within this thesis.

3.4 The Bayesian perspective

In classical frequentist statistics, parameters describing a probabilistic model are assumed to be unknown but constant. They are commonly computed on the basis of counting. For example: a coin is tossed several times and the probability that head occurs at the next toss is inferred from the relation of how many tosses have been thrown with respect to the number of total tosses. The inference becomes precise if a large number of experiments (in this case tosses) are performed. However, if only one toss is performed an inference based on this logic would lead to a 100 % chance of throwing head on all following tosses.

From a Bayesian point of view, the parameters describing the probabilistic properties are considered as uncertain parameters. Inferences about these parameters are performed by updating the probability of a hypothesis about this quantity as new observations are made. The key idea is to formulate a prior probability density function about the nature of an unknown quantity which is then updated with the likelihood function. The likelihood function describes the probability of this unknown quantity taking certain values conditioned on an event. Thus, knowledge about any unknown quantity can be expressed probabilistically. In particular, this description for the prior can be formulated irrespective of the source that leads to this formulation. Bayesian statistics hence offer a framework to combine different kinds of information, like test data from different experiments and subjective judgement.

Bayesian statistics are state of the art and are widely used in a wide range of disciplines In the context of structural mechanics, it is anchored in such fundamental engineering standards as [ISO97] that describes statistical methods for quality control of building materials and components, or [EN 02] the Eurocode-basis of structural design. Examples for the application of Bayesian statistics for dynamic analysis of structures can be found in [Gol11], [Yue10]. For applications static problems see e.g. [Tof11].

The following sections give a brief introduction to the basic concepts of Bayesian statistics that are relevant for this work. For a thorough treatment of Bayesian statistics see for example [Gel13], [Kru11], [Siv06] or [Ber08].

3.4.1 Conditional probability, total probability and Bayes theorem

A conditional probability allows for inference about an event based on the observation of another event. As an example: the probability of throwing a six on a six-sided dice is 1/6. The probability of 6 occurring if it is known that the outcome is even is

$$P(\textit{outcome is } 6 \mid \textit{outcome is even}) = \frac{1/6}{1/2} = \frac{1}{3}$$

If all outcomes are equally likely the definition of conditional probability can be written as

$$P(A \mid B) = \frac{P(A \cap B)}{P(B)} \tag{3-28}$$

meaning the probability of the outcome A given B is the probability of the intersection of A and B occurring (elements belonging to A *and* to B) divided by the number of elements belonging to B.

Let $A_1,\ldots,A_n$ be disjoint events that form a partition of the sample space. Assuming that $P(A_i)>0$ for all i, it follows for any event B within the sample space

$$\begin{aligned} P(B) &= P(A_1 \cap B) + \ldots + P(A_n \cap B) \\ &= P(A_1)P(B \mid A_1) + \ldots + P(A_n)P(B \mid A_n) \end{aligned} \tag{3-29}$$

Figure 3-3 illustrates this relation. Since the events $A_1,\ldots,A_n$ form partitions of the sample space, the event B can be decomposed into the disjoint sum of its intersections A_i with B.

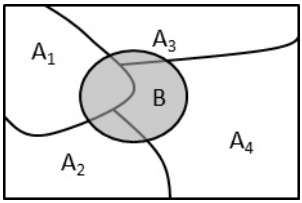

Figure 3-3 Visualisation of the total probability theorem with events A_i and B

Bayes rule now relates conditional probabilities of the form P(A|B) to conditional probabilities of the form P(B|A), in which the order of the conditioning is reversed. Bayes rule is then written as

$$P(A_i \mid B) = \frac{P(A_i)\,P(B \mid A_i)}{P(B)} = \frac{P(A_i)\,P(B \mid A_i)}{P(A_1)P(B \mid A_1) + \ldots + P(A_n)P(B \mid A_n)} \tag{3-30}$$

3.4.2 Basic concept

In engineering practice, lack of information is a common situation and makes engineering judgement necessary. In the case of parameter estimation, some knowledge might be present about the possible values or their range, coming from experience of the designer or a similar engineering problem. Suppose a discrete case where a model parameter Θ is assumed to be a set of discrete values θ_i, i=1,2,…,n with prior likelihood $p_i=P(\Theta=\theta_i)$. As new observations or test results become available, the prior assumptions on the parameter θ can be updated through Bayes' theorem and the probability mass function (PMF) P for θ can be computed as:

$$P(\Theta = \theta_i \mid \varepsilon) = \frac{P(\varepsilon \mid \Theta = \theta_i)P(\Theta = \theta_i)}{\sum_i^n P(\varepsilon \mid \Theta = \theta_i)P(\Theta = \theta_i)} \quad i = 1,2,\ldots,n \tag{3-31}$$

Here, $P(\Theta = \theta_i)$ is the *prior* probability of $\Theta=\theta_i$, reflecting our knowledge about the parameter before the experiments. This knowledge can be based on previous experiments or subjective judgements. $P(\varepsilon \mid \Theta = \theta_i)$ is the *likelihood* of the experimental outcome ε if $\Theta=\theta_i$ – in other words, the conditional probability of observing the experimental outcome ε assuming that the parameter is θ_i.

$P(\Theta = \theta_i \mid \varepsilon)$ is the *posterior* probability of $\Theta=\theta_i$, the probability that has been updated based on new observations ε. The denominator serves as a normalising factor to ensure that the sum of posterior probabilities adds up to 1.

In the continuous case, sums are replaced by integrals:

$$f_{\Theta|X}(\theta \mid x) = \frac{f_\Theta(\theta)\,f_{X|\Theta}(x \mid \theta)}{\int f_\Theta(\theta')\,f_{X|\Theta}(x \mid \theta')\,d\theta'} \tag{3-32}$$

The formulation of a prior probability density is vital for the approach. However, if no information is available a common way is to formulate a so-called uninformative prior, written as a uniform distribution.

The following example is reproduced from Ang and Tang [Ang07] to illustrate the concept.

> Reinforced concrete piles for a building foundation could be subject to defects resulting from poor construction quality. Some of the common defects would include insufficient bonding, inadequate length, cracks, and voids in concrete. An engineer would like to estimate the proportion of piles that are defective in a given project that may consist of hundreds of piles. Suppose that from the engineers' experience with a range of construction quality for various pile foundation contractors in the region of the project site, he estimated (judgementally) that the proportion of defective piles, *p*, for the site would range from 0.2 to 1.0 with 0.4 as the most likely value; more specifically, *p*, is described by the prior PMF as shown in Table 3-2 (first line).
>
> The values of *p* are discretized at 0.2 intervals to simplify the illustration.
> On the basis of this prior PMF, which is based entirely on the engineers' judgement, the Bayesian estimated probability of a defective pile would be (by virtue of the total probability theorem) the sum of the products of proportions of the files being defective and corresponding prior probabilities (refer to Table 3-2):
>
> $$\hat{P}' = (0.2)(0.3) + (0.4)(0.4) + (0.6)(0.15) + (0.8)(0.10) + (1.0)(0.05) = 0.44$$
>
> In order to supplement his judgement, the engineer ordered a pile to be selected for inspection. The outcome of the inspections shows that the pile is defective. Based on the result of this single inspection, the PMF of p would be revised according to Equation (3-31)
>
> $$P''(p = 0.2) = \frac{(0.2)(0.3)}{(0.2)(0.3) + (0.4)(0.4) + (0.6)(0.15) + (0.8)(0.10) + (1.0)(0.05)} = 0.136$$ [1]
>
> Similarly the posterior probabilities for the other values of *p* are obtained as follows:
>
> $$P''(p = 0.4) = 0.364$$
> $$P''(p = 0.6) = 0.204$$
> $$P''(p = 0.8) = 0.182$$
> $$P''(p = 1.0) = 0.114$$

[1] Please note: the numerator stems from a binomial distribution

From this example it can be seen how a prior knowledge or judgement about a parameter can be updated in the light of new information. The PMF shifts towards higher probability of defective piles with each new pile tested being defective (Table 3-2). However, it is important to note that the finding of one defective pile does not lead to conclusion that all piles will be defective.

Table 3-2 Probabilities of certain proportions of piles being defective

	Proportion of piles being defective					Bayesian estimate
	0.2	0.4	0.6	0.8	1.0	
Prior P'	0.300	0.400	0.150	0.100	0.050	0.44
Posterior P'' (one inspection defective)	0.136	0.364	0.204	0.182	0.114	0.55
Posterior P''' (two inspections defective)	0.049	0.262	0.221	0.262	0.205	0.66
Posterior P'''' (three inspections defective)	0.015	0.158	0.120	0.317	0.310	0.70

3.4.3 Univariate problem with unknown mean and unknown variance

Descriptions for a more general treatment of estimation problems where not only the mean but also the variance of a parameter is unknown can be found e.g. in [Siv06] or [Gel13] and is reproduced here from [Gel13]. The difficulty here is to formulate a conjugate prior distribution for μ given σ^2 and σ^2 such that the posterior distribution function can be solved analytically. For the univariate case, these functions can be described through a normal distribution for $\mu|\sigma^2$ and the inverse chi-square distribution for the variance σ^2

$$\mu \mid \sigma^2 = N\left(\mu_0, \sigma^2 / \kappa_0\right)$$

$$\sigma^2 = Inv - \mathrm{X}^2\left(\nu_0, \sigma_0^2\right)$$

where the parameters κ_0 and ν_0 represent the degrees of freedom. The joint prior density can then be written as

$$p\left(\mu, \sigma^2\right) \propto \frac{1}{\sigma}\left(\sigma^2\right)^{-(\nu 0/2+1)} \exp\left(-\frac{1}{2\sigma^2}\left[\nu_0\sigma_0^2 + \kappa_0\left(\mu_0 - \mu\right)\right]\right) \tag{3-33}$$

The joint posterior density is the product of the joint prior density and the normal likelihood:

$$p\left(\mu,\sigma^2 \mid y\right) \propto \frac{1}{\sigma}\left(\sigma^2\right)^{-(\nu 0/2+1)} \exp\left(-\frac{1}{2\sigma^2}\left[\nu_0\sigma_0^2+\kappa_0\left(\mu_0-\mu\right)^2\right]\right)\cdot \\ \cdot\left(\sigma^2\right)^{-n/2} \exp\left(-\frac{1}{2\sigma}\left[(n-1)s^2+n\left(\bar{y}-\mu\right)^2\right]\right) \tag{3-34}$$

In this formulation, s^2 is the variance and $\bar{y}$ the mean of the test data.

3.4.4 Bayesian meta-analysis over all specimen groups

A common problem in evaluating test data is that the data might come from several independent measurements. This might happen if results from different test institutes or a manufacturer and a test institute are compared and different values are found for a nominal identical material. The question then arises if differences are due to different preparations, boundary conditions, material batches or if the scatter of the property under investigation itself is very high. This is addressed by a meta-analysis, a combined analysis of results from different tests that assumes the different observations belonging to the same underlying population. Hence, the observations share a common mean but vary in their scatter.

From a Bayesian point of view, the common mean is then modelled as a random variable Θ. For this analysis, a normal prior is assumed, with known mean x_0 and known variance σ_0^2. The model used for the analysis has the form [Ber08]

$$X_i = \Theta + W_i, \quad i = 1,\ldots,n$$

Θ and W_i are independent and normal, where for

$$E\left[W_i\right] = E\left[W_i \mid \Theta=\theta\right] = 0, \quad \mathrm{var}(W_i) = \mathrm{var}\left(X_i \mid \Theta=\theta\right) = \sigma_i^2$$

This means for the prior

$$f_\Theta(\theta) = c_1 \cdot \exp\left\{-\frac{(\theta-x_0)^2}{2\sigma_0^2}\right\}$$

And the likelihood

$$f_{X|\Theta}\left(x \mid \theta\right) = c_2 \cdot \exp\left\{-\frac{(x_1-\theta)^2}{2\sigma_1^2}\right\}\ldots\exp\left\{-\frac{(x_n-\theta)^2}{2\sigma_n^2}\right\}$$

Here, c_1 and c_2 are normalizing constants that do not depend on θ.

Recalling Bayes' rule (Equation (3-32)) an analogy to the numerator can be written as

$$c_1 \cdot c_2 \cdot \exp\left\{-\sum_{i=0}^{n} \frac{(x_i - \theta)^2}{2\sigma_i^2}\right\}$$

After some algebra, which involves completing the square inside the exponent, the numerator is found to be of the form

$$d \cdot \exp\left\{-\frac{(\theta - m)^2}{2v}\right\}$$

This expression is describing again a normal distribution with mean m and variance v to estimate Θ and is written as:

$$m = \frac{\sum_{i=0}^{n} x_i / \sigma_i^2}{\sum_{i=0}^{n} 1/\sigma_i^2} \tag{3-35}$$

$$v = \frac{1}{\sum_{i=0}^{n} 1/\sigma_i^2} \tag{3-36}$$

3.4.5 The MAP rule

A general Bayesian inference method is the maximum a posteriori probability (MAP). It is used for point estimation by maximizing the posterior distribution $f_{\Theta|X}(\theta|x)$

$$\hat{\theta} = \arg\max_{\theta} f_{\Theta|X}(\theta \mid x) \tag{3-37}$$

The concept is illustrated in Figure 3-4, showing a continuous posterior distribution function for a parameter θ and the realisation of θ that has the highest probability to occur.

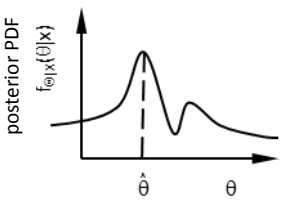

Figure 3-4 MAP rule for inference of a continuous parameter

The form of the posterior function, as given by Bayes rule, allows for an important computational shortcut: since the denominator of Equation (3-32) is constant for all θ, the maximization is only dependent on the numerator. Thus, in this case the point estimate can be carried out without computing the denominator. This is significant since the denominator is in most problems not solvable analytically and the numerical solution can be computational expensive.

4 Uncertainties with respect to stiffness properties of CFRP

With an anisotropic and inhomogeneous material as CFRP, the sources of uncertainties related to its stiffness properties can be manifold. It is hence not clear if the measured scatter of the material property is really attributed to the property itself or more concerned with the preparation of the specimen, the test procedure or the way the test is evaluated. To address these issues, several specimen sets from the same material batch of a prepreg material (EP137/CR527) are tested with varying procedures and resulting differences in stiffness evaluation are studied. The influence of the stiffness evaluation range is also briefly addressed and more thoroughly described in [Sch13].

After this analysis the Prepreg used for manufacturing of the cylinders, AS7/8557, is investigated. Due to high variations of mean values and scatter found for the longitudinal stiffness with tension tests (sections 4.1.1.3 and 4.2.3), additional measurements are carried out employing a different method based on evaluation of bending stiffness through the dynamic behaviour of coupon specimens (section 4.4).

4.1 Parameter study regarding stiffness evaluation

4.1.1 Tension testing of EP137

For the chosen CFRP prepreg test material, EP137-CR527/120-35, a parameter study is performed with the parameters divided into three categories. The first category is the specimen preparation where the width and the curing cycle for application of the gripping are varied. Concerning the test procedure, the clamping device for the specimen has been varied as well as the method to measure the strain at the specimen. Within the last category, the range for the evaluation of stiffness according to the corresponding DIN and ASTM is compared as well as a study about evaluation of strain increments up to failure carried out. The parameters are summarised in Table 4-1.

Table 4-1 Parameters studied with respect to stiffness (see also Appendix A4)

specimen preparation	width	15 mm 25 mm
	curing cycle	21°C 70°+20kN pressure
test procedure	clamping device	Manual clamping Self-clamping
	strain Measurement	Extensometer Strain gauges
stiffness evaluation	strain range DIN	
	strain range ASTM	
	strain range incremental up to failure	

4.1.1.1 Expected stiffness of EP137-CR527

The material under consideration is EP137-CR527/120-35 from Gurit which uses a 24k IMS fibre [Gur13]. The product data sheet of the fibre manufacturer denotes the fibre longitudinal stiffness as 290 GPa [Toh14]. No data for the matrix used is directly available. However, stiffness values of epoxy commonly range around 3500 MPa and this value is used for an estimate of the expected Prepreg stiffness.

The fibre mass fraction has been measured for 10 specimens taken out of two manufactured plates according to DIN EN 2564. The mean fibre volume fraction was then computed as 53% with standard deviation of 0.5%. From simple rule of mixtures, a value for the longitudinal stiffness of the CFRP specimens E_{11} can be inferred, leading to:

$$E_{11} = 0.52 \cdot 290\ GPa + 0.48 \cdot 0.35\ GPa = 155\ GPa$$

4.1.1.2 Preparation of test specimens

All specimens tested are made using hand layup technique. The unidirectional prepreg tapes of 300 mm width are cut from the role with length of 300 mm. Eight unidirectional layers are used for one plate whereupon each layer is firmly rolled on the stacking and a vacuum is applied after preparation of every four layers. The prepared laminate is placed in a setup depicted in Figure 4-1.

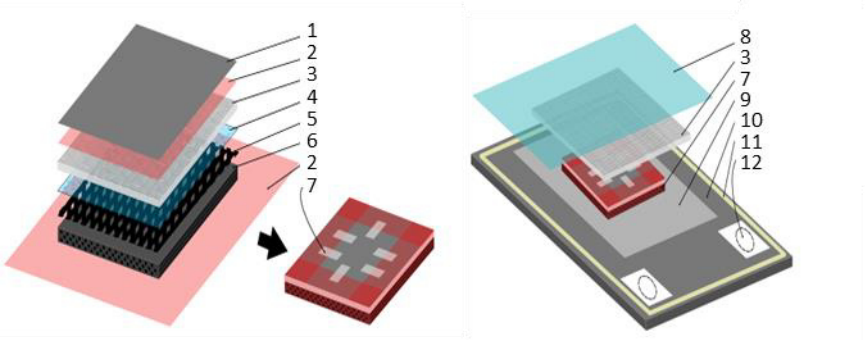

Figure 4-1 Coupon plate setup for autoclave process
(1) GFRP sheet, (2) PTFE-film, (3) suction fleece, (4) perforated film, (5) peel ply, (6) laminate, (7) wrapped laminate setup, (8) vacuum film, (9) hostaphan film, (10) aluminium plate, (11) tacky tape, (12) suction holes for vacuum pump attachment

The laminate setup is next cured in an autoclave process recommended by the supplier [Gur13] at 120° C for 90 min with vacuum applied.

After cooling, the laminate is prepared for application of the gripping devices by cleaning and grinding of the area to be glued. To ensure the later cutting of specimens in 0°-direction, a small strip of the plate along the fibre orientation is creased to serve as reference edge. Depending on the parameters under investigation, GFRP-strips or CFRP-strips are glued to the edges of the laminate followed by application of aluminium strips. Also, two types of curing cycles are investigated, one at room temperature and one at 70° C for 45 min and an applied surface pressure of approximately 0.7 N/mm².

The finished laminate plate with gripping device is then cut to the dimensions depicted in Figure 4-2 using a diamond saw blade, whereupon the width is varied within the current parameter study and specimens of 15 mm width are also cut. It has to be mentioned that for this comparison, specimens of 25 mm and 15 mm are cut from the same plates, respectively, to exclude possible differences in the laminate plate manufacturing. Refer to Appendix A4 for further details regarding number of specimens and measurement results.

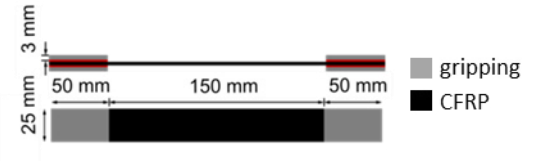

Figure 4-2 Coupon dimensions according to DIN EN ISO 527

The edges of a set of specimens are then grinded simultaneously on a clamping plate using different grain sizes until a grain size of P1000 is reached (Figure 4-3).

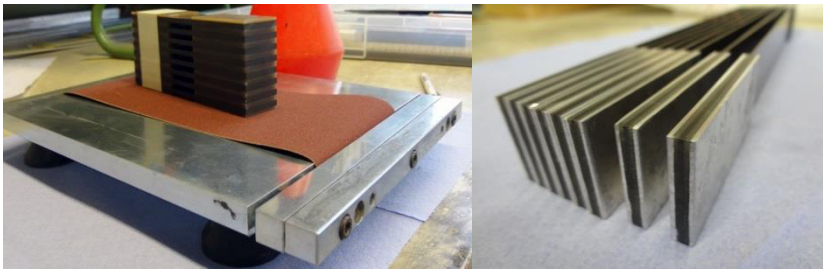

Figure 4-3 Clamping plate with specimens (left), grinded edges (right)

4.1.1.3 Tension tests

The characterisation of the material is achieved by conducting tension tests according to DIN EN ISO 527 [DIN97] with a Zwick universal testing machine 1474. The test speed is kept constant at 2 mm/min to ensure quasi-static behaviour.

Strains are measured using a Zwick/Roell extensometer 6336.102b, whereby some samples have additional strain gauges to verify the extensometer results. The clamping devices used with the according working principles are depicted in Figure 4-4. For the manual clamping four screws at the top gripping and at the bottom gripping have to be tightened in a way that allows no slipping but also does not squeeze the gripping more than necessary. Hence, the first specimen is tightened using a clamping torque of 100 Nm at the screws and for each subsequent specimen the torque is reduced until slipping during the test occurs. This procedure leads to a clamping torque of 80 Nm. Only specimens tightened at that value were evaluated.

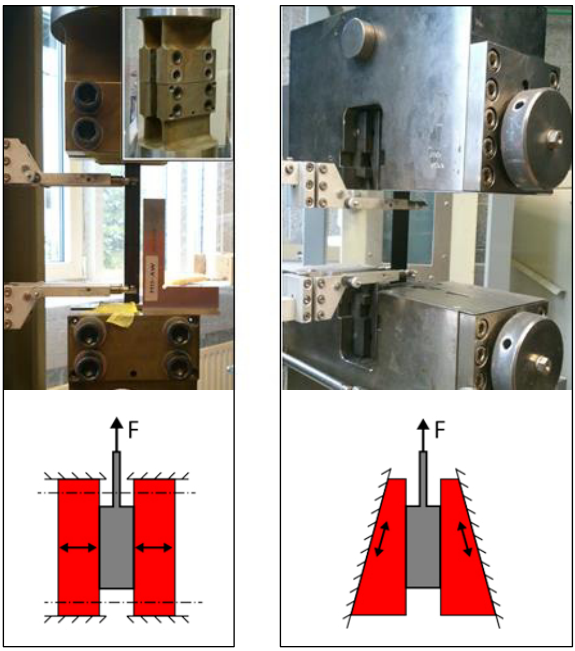

Figure 4-4 Manual clamping (left), self-clamping (right)

4.1.2 Results of parameter study

Mean and 5-95% confidence intervals for the specimen groups tested are plotted in Figure 4-5. The key to identify the abbreviations used can be found in Appendix A4.

A discrepancy between the means as well in the scatter of the measured data can be observed, here indicated through different sized confidence intervals. The highest Young's modulus was evaluated for specimens GhbsoE12 which were manufactured without peel-ply, width of 25 mm, heat and pressure applied during application of gripping and tested using manual clamping (133.6 GPa). The lowest Young's modulus of 127.2 GPa was found for specimen group GcbswE, which differs from the previous described group by the application of peel-ply during manufacturing as well as the specimen width. The difference for the mean is 5 % and 6 % for the lower confidence bound. The influences of the other factors investigated range within this order of magnitude. The type of stiffness evaluation range, described through the usage of the corresponding ISO or ASTM, respectively, resulted in a maximum difference of the computed Young's modulus of 2% for the third specimen group. The size of the confidence intervals is not significantly influenced.

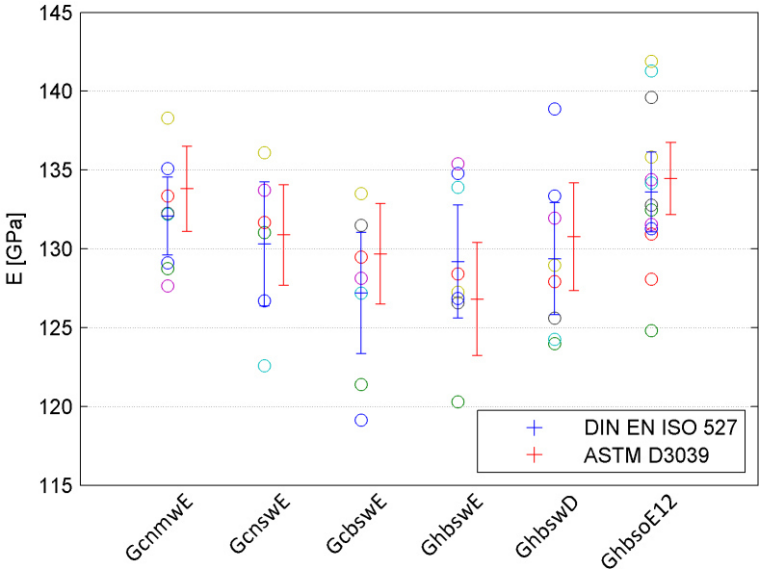

Figure 4-5 Results of parameter study regarding stiffness evaluation

Regarding the influence of the strain range considered, for one batch of specimens eight different increments of strain were evaluated for computation of the secant modulus. Results are depicted in Figure 4-6.

For the first evaluation point between 0.05% and 0.25% strain, the mean value lies significantly below the expected stiffness of 155 GPa. In the range between 0.2 and 0.3%, which corresponds to the maximum working range of common composite applications, computed mean values are also up to 20% below the expected value and increasing towards higher strains up to a mean of 159 GPa for the highest evaluated range between 1.3 % and 1.4 % strain. The expected stiffness gets exceeded at a strain level of approximately 1 %.

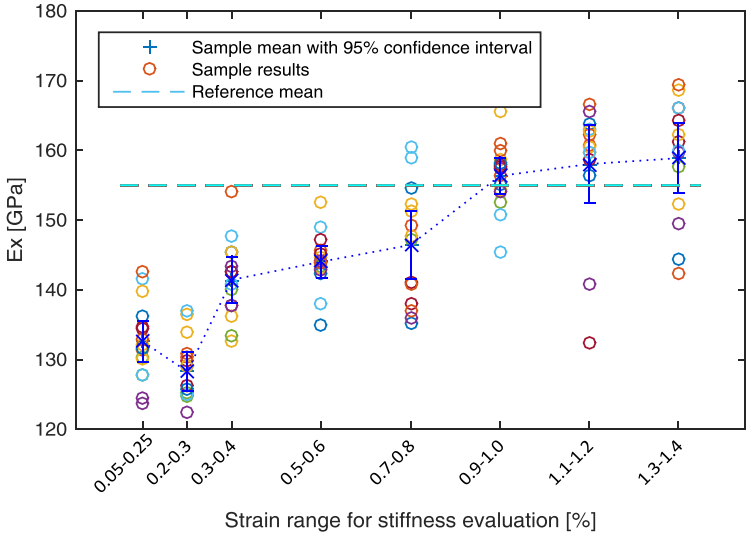

Figure 4-6 Influence of stiffness evaluation range

4.2 Tension testing of CFRP cylinder laminate AS7/8552

The Prepreg material used for the cylinders tested in section 5 is a slit tape denoted AS7/8552 by Toho Tenax.

4.2.1 Expected stiffness of AS7/8552

According to the corresponding data sheet [Hex11] the Young's modulus amounts to 153 GPa at a fibre volume fraction of 59 % while data sheet [Hex14a] gives an expected value of 145 GPa at a fibre volume fraction of 60 %. The corresponding layer thickness is 0.137 mm.

The varying specifications indicate that a variation in Young's modulus of approximately 4 % between different batches can be expected.

Following the rule of mixture and fibre stiffness of 248 GPa [Hex14a] as well as the resin stiffness of 4.5 GPa [Hex14b] leads to an expected longitudinal stiffness of 151 GPa at 60 % fibre volume fraction. For the fibre volume fraction of 65 % found for the manufactured cylinders (section 5.3.3) the calculation leads to 163 GPa.

4.2.2 Preparation of test specimens of AS7/8552

For the preparation of coupon specimens, a quasi-isotropic (QI) $[90,\pm30°]_S$ laminate as well as an eight ply unidirectional (UD) laminate is wound with process parameters identical to the cylinder manufacturing method (refer to 5.2.2). The laminate is then cut from the mandrel and peel plies are applied to both sides. The sheets are placed between two stainless steel plates and a vacuum setup is prepared. The setup is cured in an autoclave process similar to the cylinder manufacturing process [Hex14b].

After cooling, eleven specimens are cut from the QI plate with a width of 25 mm and 6 from the UD plate with a width of 15 mm. The further preparation corresponds to specimens denoted GcnmwE (refer to Annex A4).

All specimens are tested according to DIN EN ISO 527-4 [DIN97] in a tension testing rig (section 4.1.1.3).

4.2.3 Results of coupon tests of AS7/8552

From 11 QI specimens tested, 10 specimens broke within the free length (Figure 4-7, left) and have been used for the determination of the Young's modulus between strain levels 0.05 to 0.25. The resulting mean Young's modulus is 46.8 GPa with a standard deviation of 2.3 GPa (cov=5 %)

Of the six UD specimens, one showed delamination at the gripping. All other specimens could be evaluated and lead to a mean Young's modulus of 125.6 GPa with standard deviation 4.5 GPa (cov=3.6 %) (Figure 4-7, right).

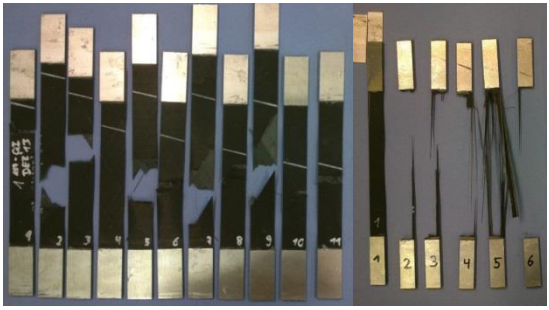

Figure 4-7 Broken coupon specimens, QI (left), UD (right)

4.3 Comparison of CLT and test results

For both prepreg systems investigated, a large discrepancy was found between expected Young's modulus according to rule of mixtures and measured tension tests. For

the EP137-CR527 tests of the reference configuration (GcnmwE) the measured value is 15 % below the expectation.

For the AS7/8552 Prepreg at 65 % fibre volume fraction, the coupon stiffness measured lies 29 % below the value computed by constituent data (section 4.2.1) and rule of mixture.

4.4 Dynamic identification of Young's' modulus

Bending stiffness values derived from flexural-test data will be comparable to those derived from tensile-test data only at strain levels where the stress-strain relationship is linear and for specimens which have a homogeneous structure. This is due to higher influence of layers that are further away from the neutral axis. However, this influence was found to be negligible for the layups investigated.

4.4.1 Working principle according to DIN EN ISO 6721

Determination of the dynamic Young's modulus using resonance curve procedure is carried out according to DIN EN ISO 6721, part 3 [DIN96].

ISO 6721 covers the determination of loss factor and storage modulus of test strips excited by a sinusoidal force. The method employed is denoted as method A, where the test strip is fixed on one end and actuated using a shaker at varying frequency, in this case between 10-2500 Hz, to reach the fifth eigenfrequency. The resonance curve of the forced vibration is measured and the complex modulus is calculated from the results. The frequency response is measured around the resonances and the frequency values are determined where the amplitude has reduced by 3 dB compared with the resonance value (Figure 4-8). Due to some noise in the measurements, the resonance curves are smoothed prior to analysis.

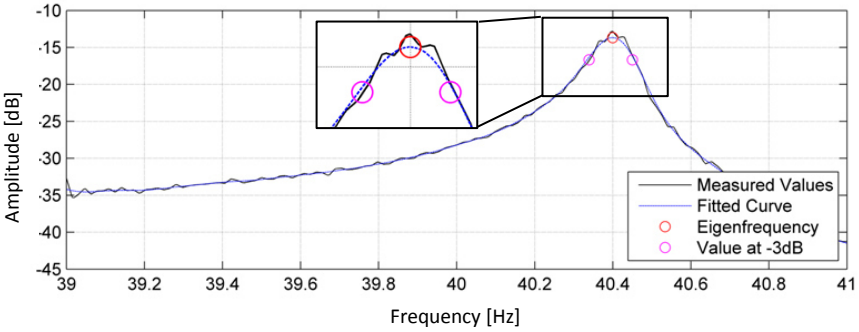

Figure 4-8 Resonance curve around eigenfrequency with 3 dB decrease

The characteristics of the materials investigated are calculated using the resonance frequency and the distance of the respective 3 dB points.

The bending storage modulus is then calculated as

$$E_f^{'} = \left[4\pi \cdot (3\rho)^{0.5} l^2 / h\right]^2 \cdot \left[f_{ri} / k_i^2\right]^2 \tag{4-1}$$

where r is the density, l and h are length and thickness of the strip, respectively, f_{ri} is the resonance frequency and k_i^2 a correction factor depending on the mode number.

The loss modulus is computed as

$$E_f^{''} = E_f^{'} \cdot \tan\delta = E_f^{'} \cdot \Delta f_i / f_{ri} \tag{4-2}$$

with Δf_i being the distance between the values at +/-3 dB next to the resonance frequency.

The complex modulus, representing the bending stiffness, is then

$$E^* = \sqrt{E_f^{'2} \cdot E_f^{''2}} \tag{4-3}$$

4.4.2 Test setup

The test setup is shown schematically in Figure 4-9, left and in practice in Figure 4-9, right. A shaker of type RMS SW 122/3 in conjunction with a power amplifier RMS TG A is used with a maximum amplitude of 7 mm and an axial force of 196 N.

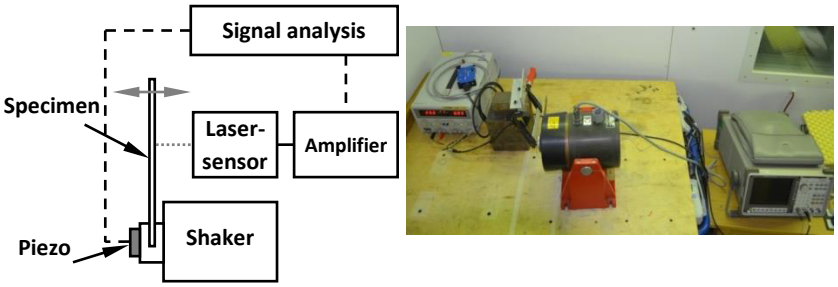

Figure 4-9 Test setup for dynamic identification of Young's modulus

The clamping is depicted in Figure 4-10. Care has been taken to always apply the same torque force for the screws to apply the same pressure within the clamping area for all specimens.

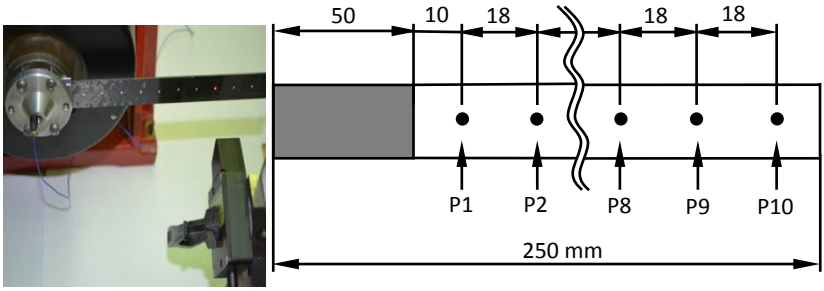

Figure 4-10 Clamping and laser measurement (left), specimen markings (right)

All specimens are marked with 10 equidistant points (Figure 4-10). The laser sensor is moved perpendicular to the test specimen plane to measure sequentially at each marked point.

For each specimen, resonance curves for the first five eigenfrequencies are recorded at each point resulting in 50 measurements per specimen.

The materials analysed are summarised in Table 4-2 with according dimensions and consist of a unidirectional and quasi-isotropic layup for the two prepregs described in section 4.1.1 and 4.2.

Table 4-2 Specimens used for dynamic analysis

			nominal values			
material	layup	No. of specimens	h [mm]	l [mm]	b [mm]	ρ [g/cm³]
EP 137 / CR 527	UD [8x0°]	10	1.00	200	25	1500
	QI $[90,+45,0,-45]_S$	10	1.00	200	25	1500
AS7 / 8552	UD [8x0°]	6	1.08	190	15	1570
	QI $[90,+30,-30]_S$	6	0.81	190	15	1570

4.4.3 Results

In contrast to the investigation performed by [Meh12] for a laminate made of fabric, the variation of modulus values derived from different locations of the same specimen was generally below 0.1 % and was hence not further considered. Instead, mean values for each specimen are computed over the length of the specimen. The results for the

complex modulus are depicted in Figure 4-11 for the QI specimens and in Figure 4-12 for the UD specimens.

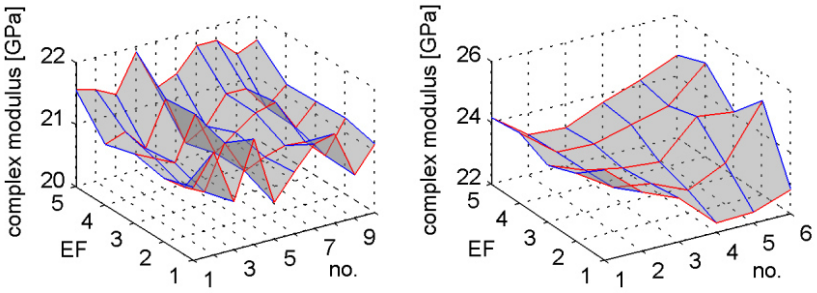

Figure 4-11 Complex modulus of QI specimens, EP137-CR527 (left), AS7-8552 (right)

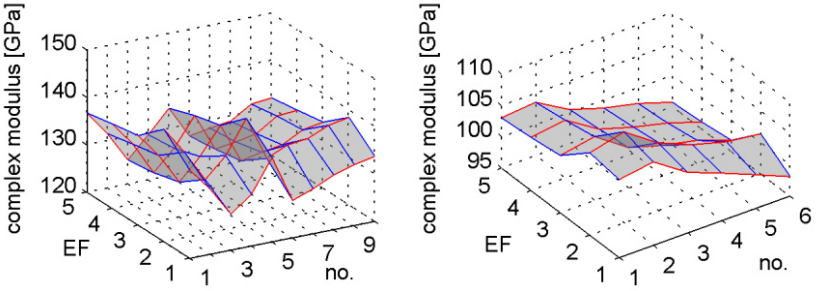

Figure 4-12 Complex modulus of UD specimens, EP137-CR527 (left), AS7-8552 (right)

Little influence is found for the eigenfrequency (EF) that is the base for the computation of the complex modulus (note the small scales for the z-axis in Figure 4-11 and Figure 4-12). From the scale of the graphs it is also visible that the scatter of the specimens is very low. The coefficient of variance is somewhat higher for the UD specimens, namely 1.87 % for EP137-CR527 and 2.50 % for AS7-8552 and 1.49 % and 1.12 % for the QI specimens, respectively (refer Table 4-3).

In Table 4-3 the mean bending stiffness according to DIN EN ISO 6721 is given along with the tension modulus measured for the same material (4.1.1.3 and 4.2.3). To compare the results the stiffness matrices for the two materials are computed in compliance with the tension tests. Then, the bending stiffness is calculated using the following relation :

$$E_b = \frac{12}{t^3 \cdot d_{11}} \tag{4-4}$$

where t is the specimen thickness and d_{11} is the first entry of the compliance matrix. The resulting computations for bending and tension stiffness values along with relevant measurements are summarised in Table 4-3.

Table 4-3 Comparison of stiffness measurements for different test methods

			bending stiffness DIN EN ISO 6721			tensile stiffness DIN EN 527		bending stiffness calculated from uniaxial tests
pre-preg	layup	mean t [mm]	mean [GPa]	COV [%]	tan δ	mean [GPa]	COV [%]	mean [GPa]
EP137-CR527	UD	1.04	132.8	1.87	0.0024	131.0	3.30	131.0
	QI	1.01	21.1	1.49	0.0062	48.4	5.00	21.8
AS7-8552	UD	1.06[1]	101.95	2.50	0.0045	125.6	3.57	125.6
	QI	0.85	23.68	1.12	0.0091	46.7	4.97	21.6

4.4.4 Summary and discussion

The tension tests according to DIN EN 527 show significant deviations when changing the specimen preparation method. In particular, considerable scatter is found within each set of specimen, ranging from 2.7 to 5 %. In contrast, the reproducibility of the evaluated stiffness value within a set of specimens is very high when applying DIN EN ISO 6721. Here, scatter exceeds 2 % only for the AS7-8552 UD specimens. This indicates that the material inherent scatter is lower than found by the tension test.

When directly comparing methods, only marginal differences of the bending stiffness measured using ISO 6721 and those calculated from tensile stiffness values are found for EP 137-CR 527 as well as for the QI specimens of AS7-8552. UD specimens of AS7-8552 show a very high deviation for the bending stiffness. This is probably due to the

[1] Including resin layer

large influence of the thickness on the computational result and the presence of the resin layer that contributes little to the bending stiffness compared to the outer fibre layers but is also considered in the overall thickness measurement that has been carried out using a micrometre gauge. If the thickness without resin layer found for a six layer coupon specimen in section 5.3.1 is scaled to eight layers, and the resulting 0.971 mm is inserted in Equation (4-3), the computed tension and bending stiffness is 125.4 N/mm², thus very closely matching the result of the tension test.

The test method to evaluate the bending stiffness by dynamic analysis is very susceptible to the thickness of the specimen. Thus, additional measurements should be carried out and confirming the measured thicknesses using a micrometre gauge via analysing micrographs. The manufacturing method of the specimens should be adjusted such that no significant resin layer remains on the surface, e.g. by using different peel ply.

The considerably lower scatter of the material stiffness found for the dynamic analysis in conjunction with the variety of scatter found for different test setups in section 4.1 for the static test suggest that the material stiffness scatter is overestimated by those tests. Consequently, for future numerical analysis the lower scatter results from the dynamic tests are used.

5 Experimental analysis of cylinder buckling

The following section describes the characterisation of 12 CFRP-cylinders and experimental work on the TUHH Hexapod. Large parts of this section have been pre-published in [Sch15].

5.1 Tension testing of resin for cylinder potting

5.1.1 Preparation of the test specimens

For the potting of the cylinders epoxy resin L with hardener GL-2 is used in conjunction with small amounts of quartz powder with a weight ratio of 10:3:0.4, respectively. A 3D-printed plastic mould is used with specimen dimension as described in ASTM D638-02a [AST02]. The material is then cured at room temperature for 24 hours. After demoulding, the surface is grinded cautiously to achieve good surface properties.

5.1.2 Tension tests

Tension tests are carried out in accordance with ASTM D638-02a using a Zwick universal testing machine 1474. The test speed is kept constant at 5 mm/min.

Strains are measured using a Zwick/Roell extensometer 6336.102b (Figure 5-1, left). The specimens are loaded until fracture occurs (Figure 5-1, right).

Figure 5-1 GL-2 resin specimens

5.1.3 Results

Two of the four samples did not break within the gauge length but the fracture strength is not of interest for this analysis. Elastic stiffness properties could be evaluated and are summarised in Table 5-1. With a mean of 3110 MPa, the stiffness lies within the lower range of typical epoxy resins.

Table 5-1 Coupon test results for potting material

specimen no.	width [mm]	thickness [mm]	Young's modulus [MPa]
C1	13.02	4.01	3210
C2	13.02	3.98	3190
C3	13.04	3.99	3150
C4	13.07	3.92	2910
μ	13.04	3.98	3110
σ	0.02	0.04	140.5

5.2 Preparation of unstiffened cylinder specimens

5.2.1 Measurement of the mandrel

Two cylinders are manufactured at DLR in Braunschweig using the filament winding process [Sch15]. The material used is a ¼'' slit Hexcel AS7/8552 CFRP-Prepreg with a nominal thickness of 135 µm at 60% fibre volume content. A mandrel consisting of a

1.82 m steel pipe and end domes is grinded and used to manufacture a cylinder of corresponding length that is cut to 6 cylinders of 255 mm length each. The diameter ratio of the mandrel to the inner tube is 2 for realisation of geodesic winding angles of the ±30° layers.

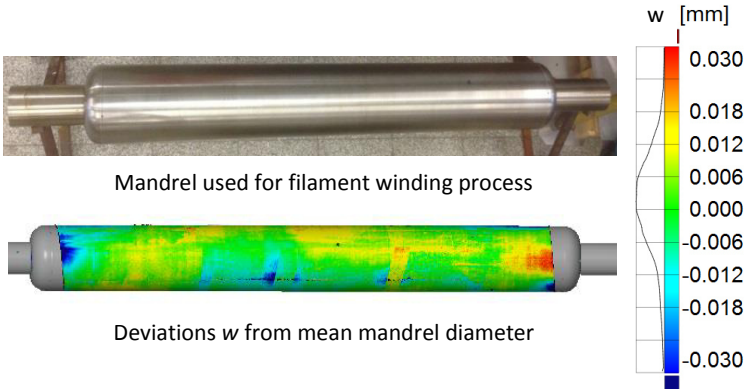

Figure 5-2 Mandrel as is (top), surface plot (bottom)

The mandrel is measured using the GOM-ATOS scanning system [GOM16b] at DLR. ATOS uses two cameras to take images of the object and uses photogrammetric methods to compute the position of the measured points in space.

Depicted in Figure 5-2 is the deviation from its mean radius of 113.905 mm. The area that is used to wind the cylinders shows a tolerance of +/- 0.03 mm. The outer edges show slightly higher deviations of up to 0.04 mm. The colourbar depicted on the right hand side of Figure 5-2 also shows the histogram of deviations found.

5.2.2 Winding process

After cleaning the mandrel, applying of release agent and referencing the mandrel in the filament winding machine, the layers corresponding to a [90°,±30°,±30°,90°]-layup are wound with a slit-tape continuously pre-stressed with 50 N.

The nearly gap free and overlap free fibre placement quality achieved in the process is shown exemplary in Figure 5-3.

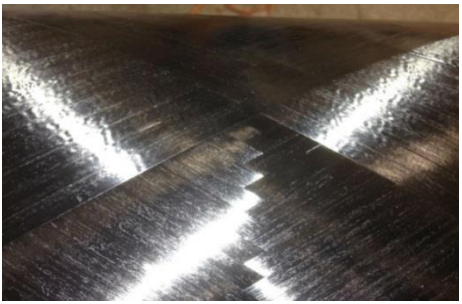

Figure 5-3 ±30° Crossing of +30° and -30° tapes

The filament winding process is finished with the winding of a peel-ply tape (50 mm width) with an overlap of 50%.

Finally the mandrel is placed in an autoclave and the laminate is cured under 7 bar and 180°C in a cycle according to [Hex14b].

After curing the mandrel is fixed in the filament winding machine and the peel ply is removed. The positions of the edges of the 6 cylinders are marked with an initial saw-cut.

After cutting off the domes of the laminate and loosening of the laminate from the mandrel, the laminate can be shifted along the rotational axis of the mandrel. A circular saw is mounted on the head of the filament winding machine and positioned to the end of the cylindrical range of the mandrel. The previously marked cutting edges are aligned to the saw blade and fixed on the mandrel. The specimens are cut by moving the rotating saw blade towards the mandrel.

5.2.3 Layup identification

The layup process chosen by the manufacturer resulted in a non-homogeneous layup-sequence that varied in longitudinal as well as circumferential direction for both cylinders manufactured. The two resulting winding-ups are depicted in Figure 5-4 with individual cylinders separated through vertical dotted lines and numbered according to their position on the mandrel.

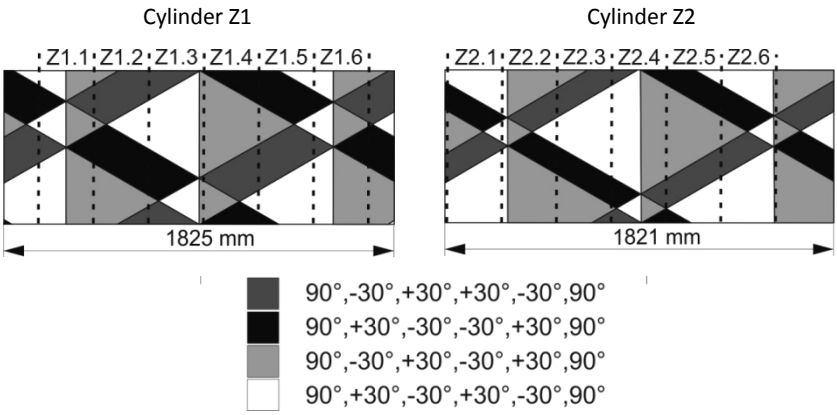

Figure 5-4 Layup patterns of the cylinders

5.2.4 Clamping of cylinders

A schematic drawing of the steel mounting is depicted in Figure 5-5. It consists of a circular ground plate on which the inner ring and outer ring are attached. Both rings are divided into two parts to allow for easy decomposition. The inner contour of the outer ring is inclined at an angle of 60° with respect to the top surface. The outer ring is clear off the cylinder.

The outer diameter of the inner ring corresponds to the nominal diameter of the cylinder in the top section. Here, the cylinder fits tight with tightness varying due to manufacturing tolerances of the cylinders. From there the contour descends into a small recess.

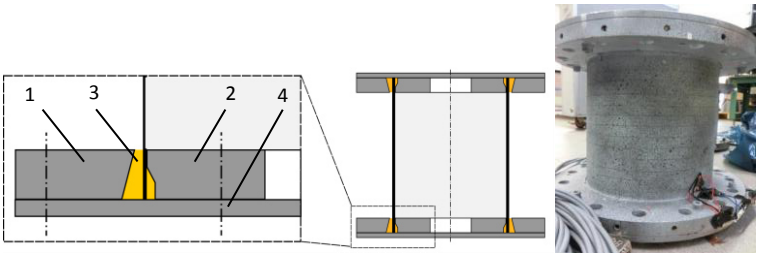

Figure 5-5 Mounting arrangement, schematic (left)
(1) outer ring, (2) inner ring, (3) resin, (4) baseplate; fully mounted (right)

Inner ring and baseplate and outer ring and baseplate are drilled together during the manufacturing process respectively to avoid misalignments. Aligning pins are installed to guarantee exact and reproducible alignment.

Before the cylinder is placed into the mounting, all metal parts are treated with a release agent to allow for disassembling and reuse of mountings. The recess area is filled with epoxy (type L with hardener GL 2). The cylinder is then slowly lowered into the matrix-bed so surplus epoxy can escape through the gap between outer ring and cylinder.

The matrix is then cured for several hours at around 30°C. After cooling, the procedure is repeated for the other side. Due to matrix shrinkage, small amounts of epoxy are repeatedly injected into the gap until the epoxy levels with the top of the outer ring.

The holes visible on the surfaces of the outer rings (Figure 5-5, right) can be used to screw pins through the rings down to the epoxy bed. Since no structural connection exists between epoxy and the metal parts due to the usage of a release agent, the pins can be used to transfer shear loads (not necessary for pure axial load cases).

5.3 Microanalysis

Polished micrograph sections (Figure 5-7) show the six layers from inner contour of the cylinder to outer contour (left to right). This section was cut out of a cylinder at an angle of 20° with respect to the cylinder axis, resulting in the outer 90° layers being cut under 70° (refer to Figure 5-6) and appearing as very long ellipses in Figure 5-7.

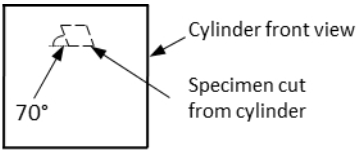

Figure 5-6 Cylinder schematic with specimen cut for microanalysis

The boundaries of all layers are clearly visible, with a particular separation between layer one and two. The interface here is more pronounced and resin rich than for other interfaces. This zone indicates that during the autoclave process, not all surplus resin from the Prepreg bled out.

Some voids are also visible as black spots in layer two and four.

A distinct contour of the inner 90° layer (layer one) of the cylinder can be seen on the left hand side. This is where the Prepreg tape was wound on the mandrel. On the outside 90° layer a wave-like pattern with growing and decreasing thickness of a resin layer is visible. This resin layer strongly varies in thickness approximately from 15 to 100 µm.

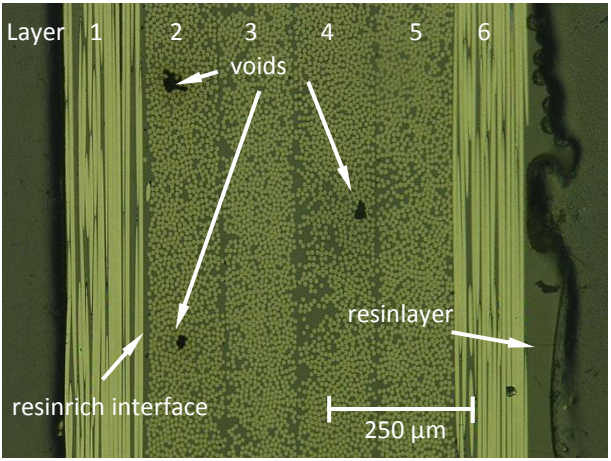

Figure 5-7 Polished micrograph section

This epoxy-layer results from the application of the peel-ply and the processing under heat and pressure. Epoxy gets effectively pressed out of the layers (which is intended to increase the fibre volume fraction). However, when removing the peel-ply, an epoxy-layer remains on the surface.

5.3.1 Thickness

5.3.1.1 Thickness distribution

Due to the existence of the outer resin layer, the optical measurements carried out to determine the thickness of the cylinders cannot be directly used for the determination of the thickness of the load carrying laminate. Instead, 9 microscopic specimens are taken from cross sections of cylinders Z1.1, Z1.2, Z2.1 and Z2.4. Additionally, 3 samples are taken from a coupon plate and 3 from a tube section of the first manufactured tube that has not been tested in buckling before. 20 thickness measurements are taken from each sample to evaluate the overall thickness of the 6 Prepreg layers, as well as the thickness of the outer resin layer. A meta-analysis, as described in section 3.4, is then carried out for thickness measurements of the individual layers as well as for the overall thickness of the laminate. Figure 5-8 shows the results for the individual layers.

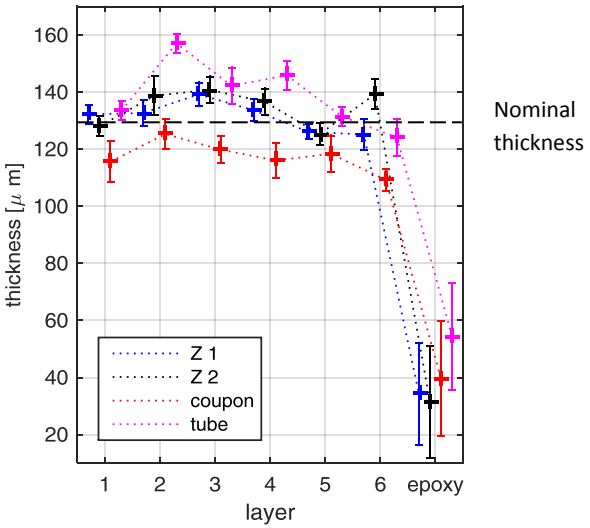

Figure 5-8 Mean thickness and standard deviations for individual layers

While the samples from Z1 and Z2 are similarly scattering around the nominal thickness value of 130 µm, the coupon specimens are considerably thinner. Most likely, this effect is due to the coupon plate being able to expand freely sidewards during the autoclave process.

Specimens from the tube section show higher thickness values, especially for the epoxy layer. The specimens are taken in close proximity to the end dome section (~150 mm) and one of the specimens is omitted due to high misalignment of the elliptical principal axis from the laminate plane, indicating lacking compression in some parts of this tube section.

Table 5-2 Uncertainty of overall thickness (without resin layer)

	Z1	Z2	coupon	tube
μ [µm]	791.5	811.2	728.5	804.1
σ [µm]	6.38	3.01	7.17	3.99

A combined treatment of specimens from Z1 and Z2 using a meta-analysis leads to a mean thickness of 803 µm with COV of 1.70 %. The mean resin layer thickness is 33 µm (COV=57 %).

5.3.1.2 Thickness autocorrelation

To study the correlation length of the laminate thickness, measurements are taken at 20 positions of each specimen along its width. A distance between measurement positions of 62.5 µm is chosen in order to evaluate a reasonable number of data points up to a distance of 1000 µm, corresponding to the element size used in Finite Element models in section 7. Measurements include optical determination of individual layer thicknesses at this position as well as the thickness over all layers. Figure 5-9 shows an example of the resulting measurement grid.

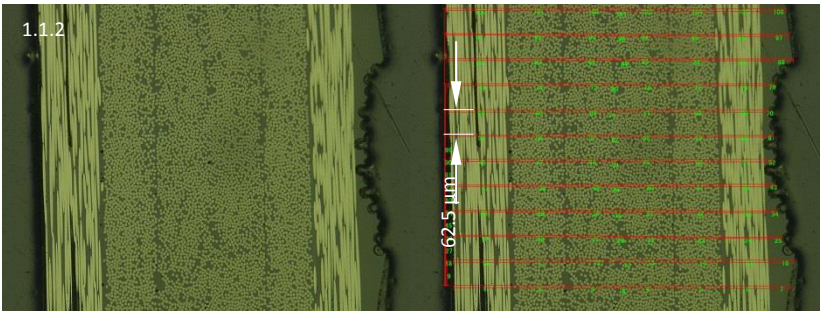

Figure 5-9 Example for taking thickness measurements for autocorrelation analysis

First two digits of the specimen number represent the cylinder number, the last digit is numbered consecutively. Missing specimens have not been evaluated due to extreme waviness of inner and outer contours indicating a certain load history that might result from the cutting method. Two examples of such specimen are depicted in Figure 5-10. For comparison, three of these specimens are further analysed.

The autocorrelation coefficients are then computed according to Equation (3-13) and shown in Figure 5-11.

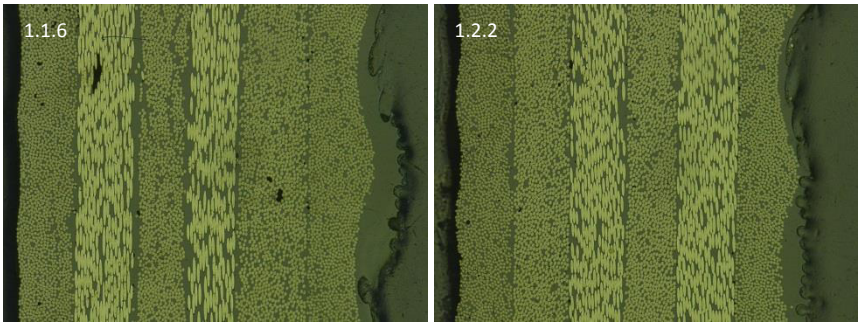

Figure 5-10 Example for specimens omitted due to large deformations

At the lowest measured distance the autocorrelation lies between 0.5 and 0.8 and rapidly decreases from there. The highest negative correlation is then reached at a distance between 500 to 600 µm. At distances greater than 600 µm, coefficients tend to be of very low magnitude (Figure 5-11).

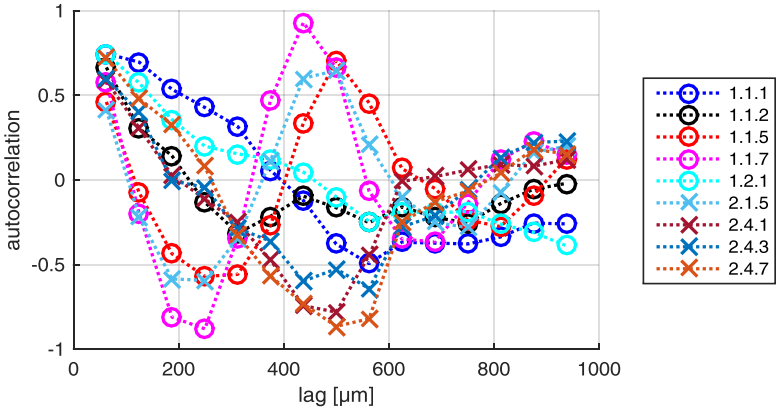

Figure 5-11 Autocorrelation of cylinder specimens

Three specimens (1.1.5, 1.1.7 and 2.1.5, refer Figure 5-12) show a different behaviour with respect to their autocorrelation. Here, a cosine-like periodicity is visible up to around 500 µm with distance from maximum to minimum of 200 µm.

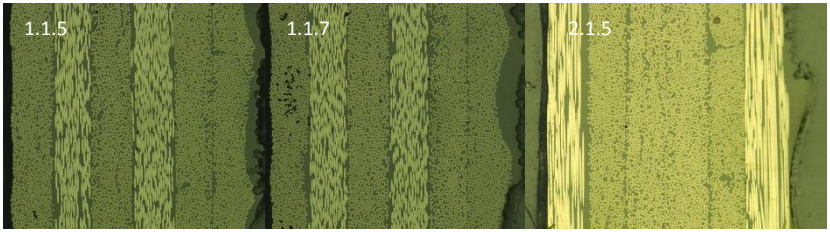

Figure 5-12 Specimens with different autocorrelation behaviour

Additional analysis is performed for the specimens from the coupon plates (2a-b, 6a), as well as from the rim of a tube section of Z1 that has not been tested in buckling (t1-t4). Figure 5-13 shows a variable autocorrelation coefficient that is around 0.6 for the lowest measured distance of 62.5 µm but rapidly decays from there and generally does not reach a relevant coefficient amplitude at greater distances.

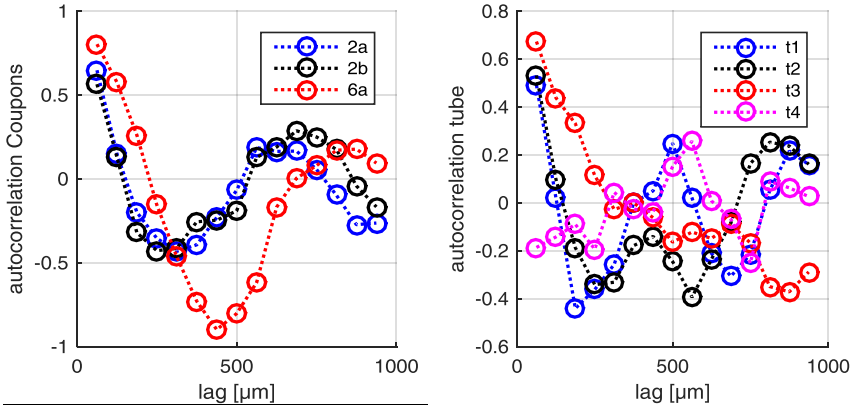

Figure 5-13 Autocorrelation of coupon specimens (left) and of tube section (right)

The analysis of the autocorrelation values shows that the relevant correlation length is very short (~62.5 µm) and albeit a certain waviness is apparent, there is no regular characteristic wavelength or amplitude on this scale.

For the implementation of the thickness distribution in a FE model this means that an independent treatment of thicknesses for neighbouring elements of size significantly bigger than 62.5 µm is justified.

5.3.2 Fibre orientation

An analysis concerning distribution of fibre angles within the laminate is carried out to verify a commonly assumed value for the standard deviation of 2° [Sic09]. A principal method to determine the fibre orientations through optical analysis of the ellipses of cut fibres is published by Yurgatis [Yur87]. For a Prepreg investigated he found a standard deviation below 1 %.

Polished micrographs at a magnification of 600x are used to evaluate the scatter. The open software ImageJ [Ras15] is used to process the images. In the first step an area is chosen for the analysis (Figure 5-14 (1)). The next step is to use a threshold for distinguishing colours and assign black to the fibres and white to the surrounding matrix (Figure 5-14 (2)). The automatic identification of ellipses works if neighbouring ellipses are only surrounded by white pixels, which is why only a small number of ellipses remain for the calculation of the fibre angle (Figure 5-14 (3)). The angle is then calculated from $\alpha = \arcsin\left(\frac{minor\ axis}{main\ axis}\right)$ and mean and standard deviations are determined.

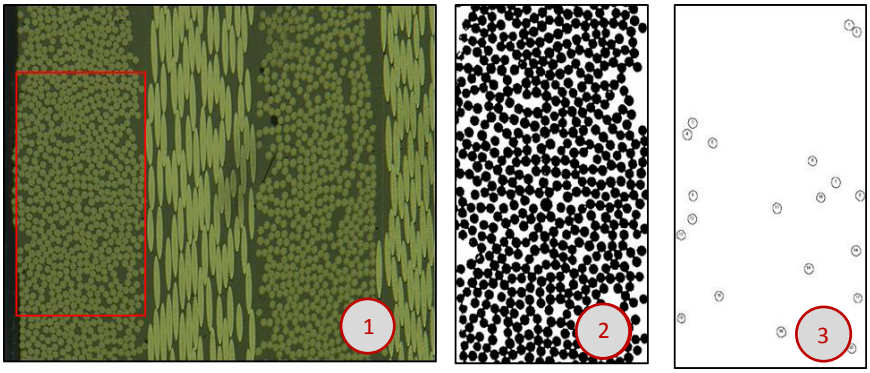

Figure 5-14 Example for analysis of fibre orientation
(1) chosen area, (2) adjusting colours, (3) recognition of ellipses that do not touch neighbouring fibres

The analysis is performed for each layer separately on five separated positions on 5 and 4 specimens of Z1 and Z2, respectively, and on the 3 coupon specimens. The resulting standard deviations are summarised in Table 5-3.

Table 5-3 Standard deviations computed from analysis of micrographs

layer	1	2	3	4	5	6
Coupon	-	1.8	3.3	2.6	2.4	-
Z1	1.5	1.0	1.0	0.9	1.3	1.6
Z2		1.3	2.2	1.5	2.1	

The comparably high scatter found for the coupon layers might be due to handling during the manufacturing process: after winding, the plate sections are cut from the mandrel, drawn flat and put on an aluminium plate for the autoclave process by hand. It is possible that through this last step fibre angles get disturbed.

Comparison of specimens from Z1 and Z2 reveal slightly higher scatter for the Z2 specimens. However, it has to be noted that with this kind of analysis the local fibre angle due to waviness and the global fibre angle due to the winding machine precision are determined simultaneously. It is possible that the restriction to measuring fibres that are less supported by neighbouring fibres leads to higher scatter than expected due to the very local picture retrieved from a microsection. When concluding on the global angle scatter from the local scatter, a certain error is hence expected. For this study the determination of a conservative value for the expected scatter is sufficient and the literature value of 2° is likely to be very conservative.

In order to exactly determine the differences between local and global fibre angle the micrographs could be grinded repeatedly by a certain amount to evaluate fibre angles for the same areas at different depths of the specimen.

5.3.3 Fibre volume content

Two methods have been employed to determine the fibre volume content. Firstly, the fibre weight fraction (FWF) is determined by wet-chemically dissolving the matrix of specimens according to DIN EN 2564 [DIN98]. Twelve specimens are cut from plates manufactured for the coupon tests with layup $[90,+30,-30]_S$ and four specimens from a section of the untested cylinder, previously referred to as tube specimens. The mean fibre volume fraction (FVF) is then computed using the constituent densities given in Table 5-4 (refer to Appendix A3 for measured data) as

$$FVF = \frac{1}{\left[1+\frac{\rho_f}{\rho_m}\left(\frac{1}{FWF}-1\right)\right]} \tag{5-1}$$

Table 5-4 Densities of tape strip constituents

material	density ρ [g/cm³]
AS7-fibre [Hex14a]	1.79
HexPly 8552 Epoxy [Hex14b]	1.2

Table 5-5 shows the computed mean fibre volume content for coupon and tube specimens that differ by about 5 %.

Table 5-5 Fibre volume content according to DIN EN 2564

	μ [%]	σ [%]
Coupon specimens	63.2	1.26
Tube specimens	57.1	0.19

Secondly, the fibre volume content is determined optically for each layer. The areas investigated are identical to those considered in 5.3.1.1. The software ImageJ is again used to apply a threshold for distinguishing colours and assign black to the fibres and white to the surrounding matrix. The fibre volume content is then calculated through determining the ratio of white pixels to black pixels. This approach is exact in when fibres are cut perpendicular to their axis (Figure 5-15, left). An error arises when fibres are cut at an angle since the method relies on a constant number of fibres through the thickness of the volume element. Figure 5-15 also depicts two off-axis cutting angles (mid, right) that show the number of fibres is not necessarily constant over the element.

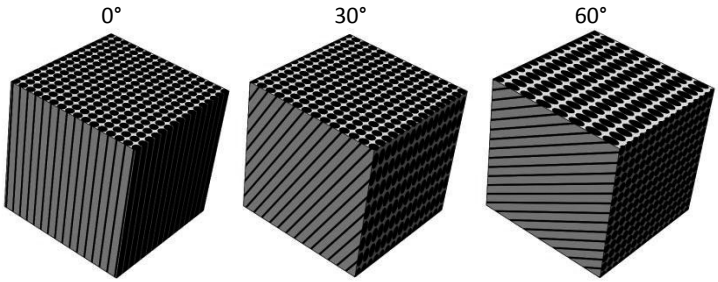

Figure 5-15 Representative volume element at different cutting angles

An error estimation is hence performed by analysing the top surface of a representative volume element at different cutting angles and computing the deviation to the

fibre volume content of the volume element. The volume element is chosen to represent the current analysis, meaning that the cube consists of an edge length of 125 µm and the fibres' diameter is 6.9 µm. The fibres are assumed to be equally spaced for simplicity.

The resulting errors for the angles considered are depicted in Figure 5-16. The error remains below 1.3 % for angles below 70°. At very high cutting angles the error increases significantly (5.1 % at 80°). At a cutting angle of 90° the top surface of such a volume element would slice along the fibre axis, making the method not applicable.

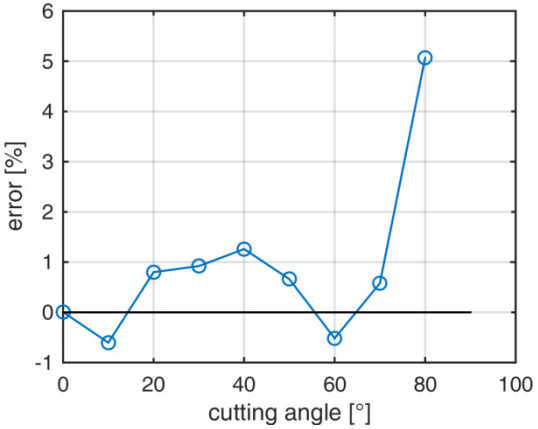

Figure 5-16 Error made when determining FVC through areal examination

The observed optically measured fibre volume contents are presented in Table 5-6.

Table 5-6 Optically measured fibre volume content

	Z1	Z2	coupon
µ [%]	61.13	58.15	67.41
σ [%]	1.81	2.12	2.34

5.3.4 Correlation of fibre volume content and thickness

To determine if the correlation between fibre volume content and thickness needs to be considered in the numerical analysis, the correlation coefficients are determined for the coupon specimens as well as for the specimens of cylinder sets Z1 and Z2.

The measurements are evaluated for layers two to four at 10 of the 12 measurement positions (Figure 5-17). The fibre cutting angles of the outer layers 1 and 6 are too large

to be used for the optical analysis of fibre ellipses. Thickness measurements are averaged over the three measured thicknesses at the fibre volume segment considered (see Figure 5-17). The fibre volume fraction is identified according to the procedure described in 5.3.3 for each layer with a height of 125 µm (Figure 5-17). The average sum of thicknesses at that position is then correlated to the averaged fibre volume fraction over layers 1 to 4 according to Equation (3-12).

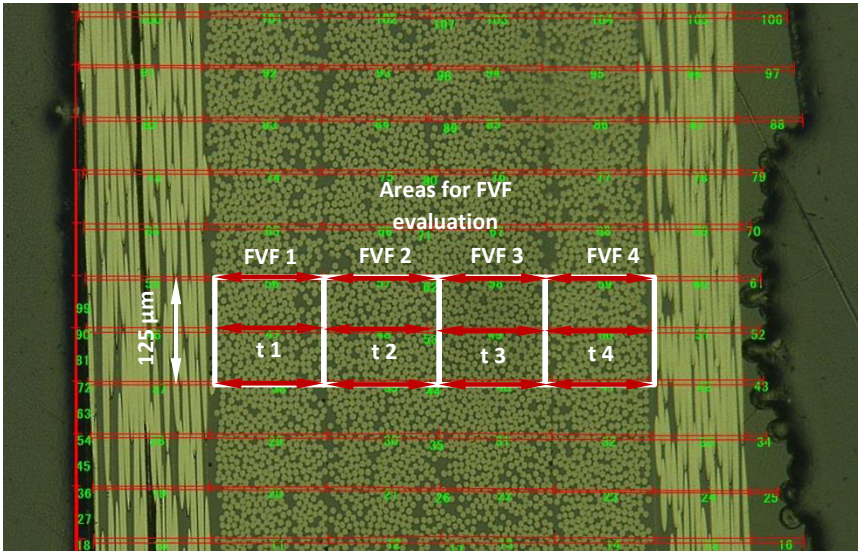

Figure 5-17 Example for data basis of correlation analysis

The results are summarised in Table 5-7 showing no clear tendency for a correlation of fibre volume content at the scale considered. Values scatter over a wide range between 0.64 and -0.33.

Table 5-7 Correlation coefficients for fibre volume content against thickness

source	Coupon			Z1					Z2			
specimen no	2a	2b	6a	1.1.1	1.1.2	1.1.5	1.1.7	1.2.1	2.1.5	2.4.1	2.4.3	2.4.7
correlation coefficient	0.64	-0.37	0.10	0.50	-0.05	-0.33	0.03	0.41	0.03	0.63	0.48	0.38

When considering the average values for thickness and fibre volume content over a range of 1000 µm, the correlation coefficient computed for specimens of set Z1 result

in 0.60 and -0.33 for set Z2. Thus, such a correlation is considered to be negligible for the Monte Carlo analysis performed in section 7.3.

On the scale considered (height of 125 µm and width 1000 µm) the assumption of constant number of fibres is not applicable.

5.3.5 Void content

To verify the quality of the cylinder material an analysis of the void content is performed. Along each micrographic section, five locations are arbitrarily chosen. However, a location is moved if the surface of the specimen shows scratches or pollutions in this section. Figure 5-18 shows the approach from left to right. Firstly, a figure is taken at a magnification of 300x. Each layer is now analysed separately and corresponding sections are cut from the overview. Next, the open software ImageJ is used to filter dark areas of the figure. It is visible in Figure 5-18 (3) that not only the voids are recognized as dark areas, but also the transition from fibres to matrix can be interpreted as dark spots. Hence, in the last step, a threshold is set for a minimum pixel size to filter those particles. As a result, an area is determined for the remaining particles identified as voids. This area in relation to the area considered describes the void content of the layer. Summarised mean and standard deviations of specimens of Table 5-7 are presented in Figure 5-19 in %.

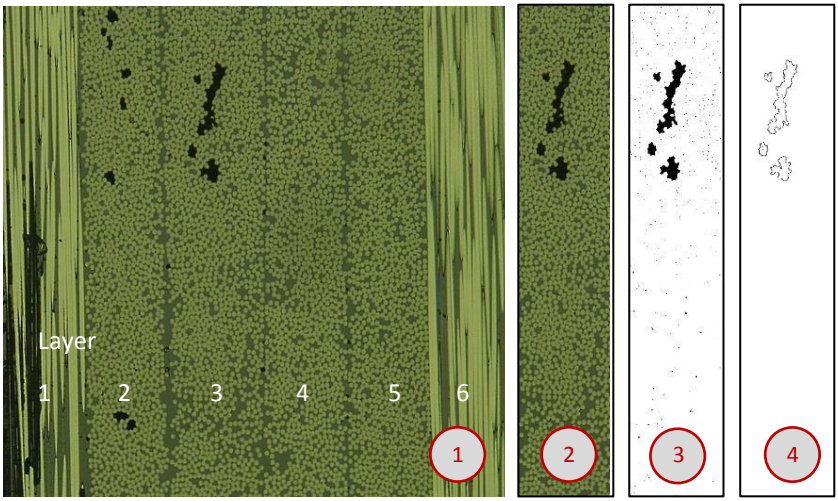

Figure 5-18 Example for void content analysis
(1) specimen, (2) image of layer 3, (3) filtering of dark colours, (4) filtering of small particles

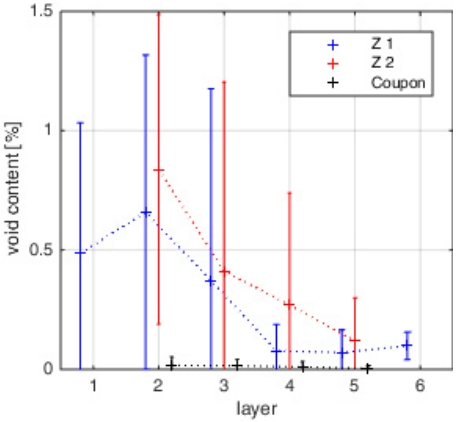

Figure 5-19 Comparison of void contents

Overall, the void content is very low for specimens of set Z1 and set Z2 with means growing slightly towards the inner layers. Still, the mean void content is below 1 %, indicating high product quality [Lie14]. For the coupon specimens voids are almost not detectable.

5.4 Cylinder geometry

5.4.1 ATOS measurements

All cylinders are measured prior to testing using the ATOS-system at DLR. From the measured data points an equidistant mesh of surface point coordinates is extracted. This can be used as an input for a finite element analysis. Also, deviations of the node positions to a best fit cylinder can be computed and the resulting imperfection pattern plotted. The radii of the best fit cylinders for all 12 cylinders are presented in Table 5-8.

Table 5-8 Radii of best fit cylinders from ATOS measurements

	Radius [mm]					
Cylinder	.1	.2	.3	.4	.5	.6
Z1.x	114.852	114.828	114.856	114.870	114.852	114.865
Z2.x	114.873	114.857	114.863	114.858	114.883	114.889

5.4.2 Comparison of imperfections prior and after mounting

The cylinders 2.1-2.6 are measured using the ATOS system before they are glued into the mountings and after. This was done to quantify the influence of the mounting on the shape of the cylinders.

The resulting measurements are similar for all 6 cylinders. Exemplary, the deviations from the best-fit cylinder of Z2.1 are shown in Figure 5-20. The equidistant peak-lines visible in circumferential direction result from peel ply fibres that could not be removed.

The cylinder shows a slight ovalized shape whereat ovalization at top and bottom are offset by 90° with respect to the cylinder axis.

With deflections of up to 0.70 mm from the nominal radius, the deformation is not visible to the naked eye. However, it is more than three times the maximum deflection measured after mounting. A direct comparison with adjusted legend is depicted in Figure 5-20, showing significant higher amplitudes of deviation from the nominal radius for the unmounted cylinder.

The large deflections due to the tendency of the unrestrained cylinder to ovalize give no hint towards the imperfection pattern that will be present after mounting and during the tests. Only at a small circumferential section at mid-height deviations are in the order of magnitude as observed after mounting.

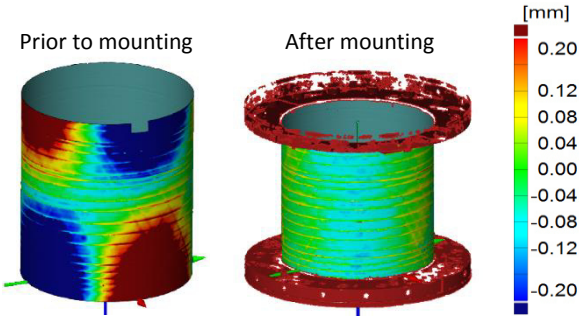

Figure 5-20 Deviations from best-fit cylinder for Z2.1

5.4.3 Surface plots

The winding-up of the mounted cylinder surface with its shell-wall mid-surface imperfection on the z-axis are plotted for cylinders Z 1.1 and Z 1.2 in Figure 5-21 [Sch15].

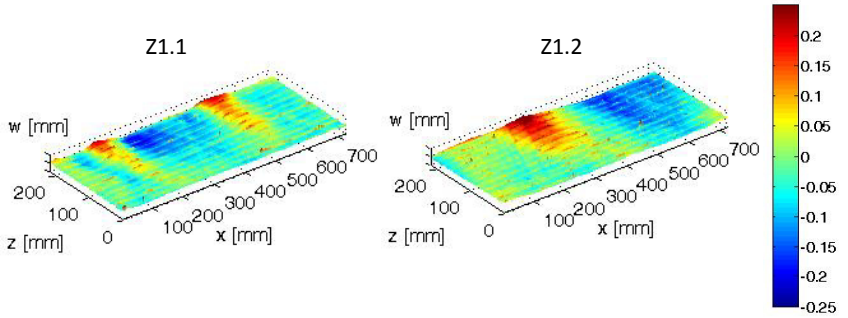

Figure 5-21 Shell-wall mid-surface imperfections

The tendency for long wave modes in axial and circumferential direction is clearly visible on all plots. Furthermore, there is an influence of the mounting sequence visible: at the lower edge with z=0 mm, which has been put on the steel mounting and glued first, the mid-surface imperfections are significantly lower than at the upper edge. This is due to the fact that the cylinder could deform more freely as compared to the second mounting step when the lower edge is already constrained. These patterns are hence indicating a certain pre-stress state.

An overview of occurring deviations can be found in the histograms given in Appendix A6 for each cylinder.

5.4.4 Power Spectral Density (PSD)

The characteristics of the shell-wall mid-surface imperfection can be considered as signal information with varying amplitude over the cylinders circumference or length. A common way to transform this information from a length-domain to a frequency domain (with unit 1/mm) is to use a Fourier transformation and decompose the imperfection pattern into its sine or cosine contents. In the context of geometric imperfections, the frequency axis is commonly scaled to represent the number of half-waves fitting into the considered length of the cylinder (compare e.g. Refs. [Arb02], [Arb05], [Kri11]).

Since the Fourier transform assumes next to stationary also ergodic signals, a more general way to analyse a random signal is to consider its power spectral density (PSD), which has been done by e.g. [Eli82], [Sch10], [Kep13]. A truncated Fourier transform F(x) is used, which decomposes a zero-mean random field f(x) of finite length L into its sine and cosine contributions as a function of frequency.

$$F(\omega) = \frac{1}{2\pi} \int_0^L f(x) \cdot e^{-I\omega x} dx \qquad (5\text{-}2)$$

The PSD is then described through [Sch10]

$$E\left[\left|F(\omega)\right|^2\right] = \int_0^L S(\omega, x)dx \qquad (5\text{-}3)$$

In this case, the well-known Welch method [Wel67] is used to estimate the PSD. It consists of the following steps

1. Dividing the data sequence into segments
2. Multiplying a segment by a window function (here: turkey window)
3. Taking the Fourier transform of the product
4. Multiplying procedure 3 by its conjugate to obtain the spectral density of the segment
5. Repeat procedures 2 through 4 for each segment so that the average of these periodogram estimates produce the power spectral density estimate

The resulting plots are depicted in Figure 5-22 for cylinders Z1.1 (left) and Z1.2 (right). They illustrate the strong narrow-bandedness of the information analysed, which is represented solely through very low frequencies with their power increasing along the z-coordinate of the cylinder.

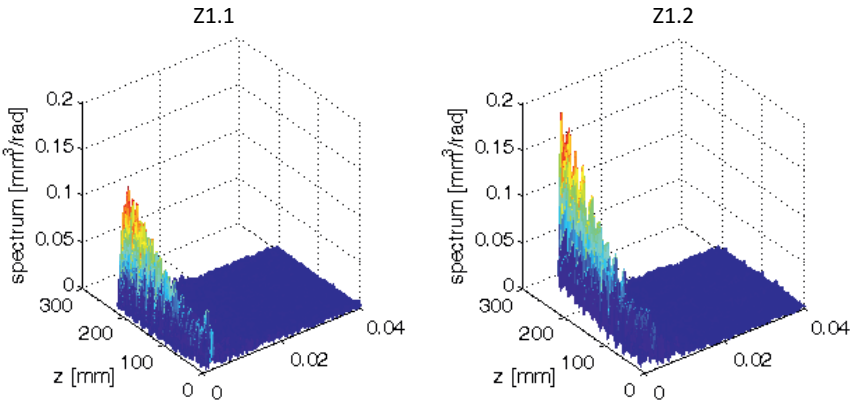

Figure 5-22 Power spectral density

For an easier read of the amplitudes, the following representation is chosen (Figure 5-23). From the PSD the y-axis of the plots is scaled down to represent the amplitude of the mid-surface imperfection. On the x-axis, instead of frequencies, the more intuitive unit of number of half-waves fitting in axial direction into the considered direction of the cylinder is depicted. For each half wave number occurring, the median (red bar), standard deviation (blue box) and 5 % to 95 % percentile (black bars) are depicted. Appearances of outliers are marked with red crosses. In contrast to the dominance of

the ovalization mode (4 half waves) of the unconstrained cylinder, it is now the mode consisting of two half waves that show the largest amplitude contribution, with the mean lying below 5% of the cylinder thickness.

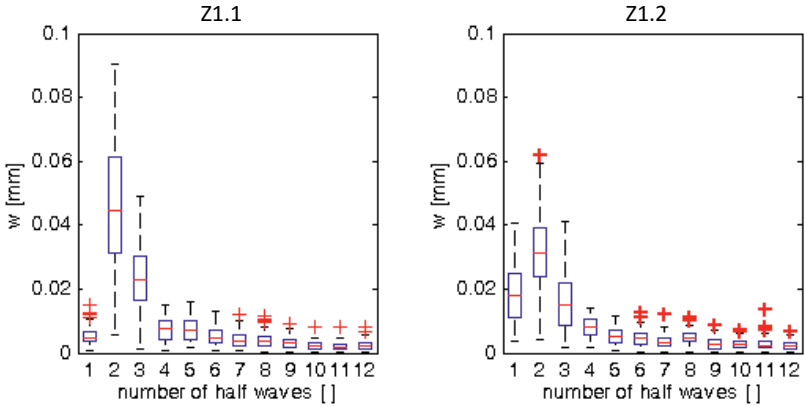

Figure 5-23 Geometrical imperfections represented through half waves in axial direction

5.4.5 Root mean square

From the PSD the root mean square (*rms*) of the amplitude can directly be calculated as the square root of the area under the spectrum vs. frequency curve corresponding to certain height of the cylinders. So for each z-position on the cylinder the *rms*-value is computed and depicted for cylinders of set 1 and set 2 in Figure 5-24.

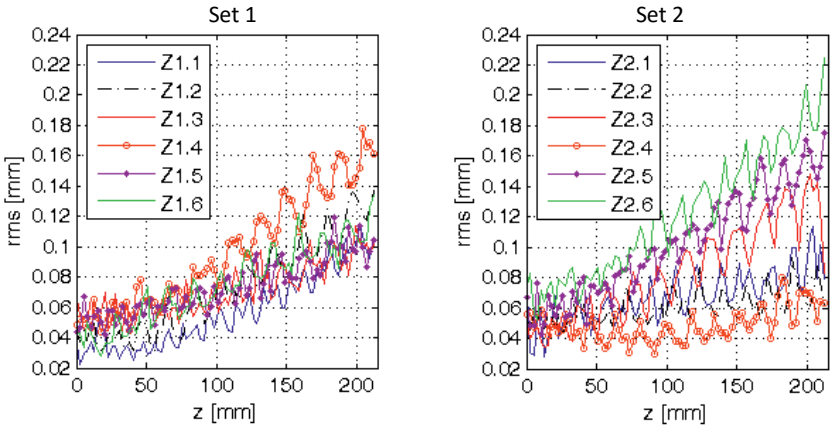

Figure 5-24 Root mean square values over cylinder height

Although some information about stochastic properties is lost, this representation offers a very direct way to compare an important characteristic regarding the amplitude of the geometric imperfection. However, the strong deviation between the *rms* values at the bottom of the cylinders at z=0 mm and the top at z=215 mm indicate that in the case of these cylinders, taking only the mean *rms* over the whole cylinder surface (refer to Table 5-9) may be misleading in terms the geometric quality achieved.

Table 5-9 Mean root mean square values

Cylinder no.		.1	.2	.3	.4	.5	.6
mean *rms* [mm]	set Z1.	0.06	0.07	0.07	0.1	0.07	0.08
	set Z2.	0.07	0.06	0.08	0.05	0.10	0.12

5.5 Structural tests

In the following section, the structural testing of 11 CFRP-composite cylinders, tested on the Hexapod testrig at TUHH [Pla13] (Figure 5-25), is described [Sch15]. Testing consisted of 2 parts. Firstly, the load in axial tension and compression is applied in the elastic regime to determine stiffness properties of the cylinders. After that, all cylinders are loaded in compression until buckling occurs.

Figure 5-25 Hexapod testing facility

Usage of the Hexapod allowed measuring possibly occurring load imperfections using a custom made 6 dof-load cell with a maximum loading capacity in axial direction of 200 kN and 150 kN in transverse directions.

5.5.1 Strain gauges

Strain gauges varied between cylinders, only data of cylinders 1.1-1.3 are reproduced here, which had eight strain gauges applied, evenly distributed in 45° steps around the circumference.

5.5.2 Load introductions

Two types of load introduction are chosen for the tests, one comprising a “clamped support” (Figure 5-26, left), and the other one representing a “simple support”. The lower attachment to the Hexapod base is identical for both and is realised through a plate with centring (no. (1) in Figure 5-26).

The clamped arrangement prohibits rotation or tipping of the structure once the first buckle appears in the structure. The arrangement also allows for application of tension or torsion loads if desired. In order to achieve a stress-free mounting as far as possible, the upper attachment consists of two plates with radial positioned webs welded to them ((6) and (7) in Figure 5-26). The lower part (6) is screwed to the cylinder mounting. Three slot holes are milled into each of those webs. The corresponding counterpart (7) has bolt holes drilled to it. Once the upper part of the attachment is screwed to the Hexapod, the apparatus can be lowered in a way that corresponding parts of (6) and (7) match and can be screwed together with bolts and nuts.

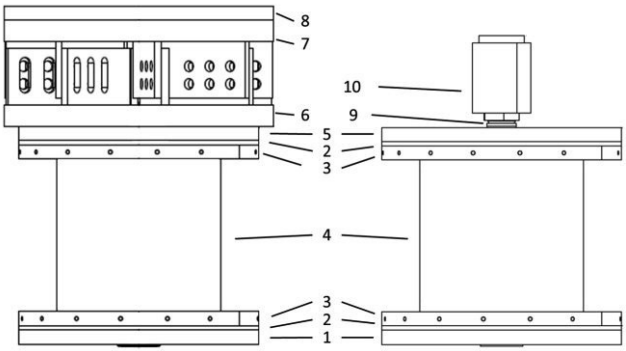

Figure 5-26 Test arrangements, clamped support (left), simply supported (right)
(1) Lower attachment plate with centring, (2) Baseplate, (3) Outer ring, (4) Cylinder, (5) Adapter plate (6) Bottom part torte – plate with welded webs including slot holes, (7) Upper part torte – plate with welded webs including holes, (8) Adapter plate – torte/ Hexapod, (9) Ball and socket joint, (10) Uniaxial load cell

The simply supported arrangement is depicted on the right hand side of Figure 5-27. Here, the Hexapod is directly resting on a uniaxial load cell (10) that is connected to the cylinder mounting via a ball and socket joint.

The clamped arrangement has been designed in order to apply compression, tension and eventually torsion forces for stiffness evaluation. The simply supported edge condition is used to resemble a realistic buckling load case where the structure tilts at buckling.

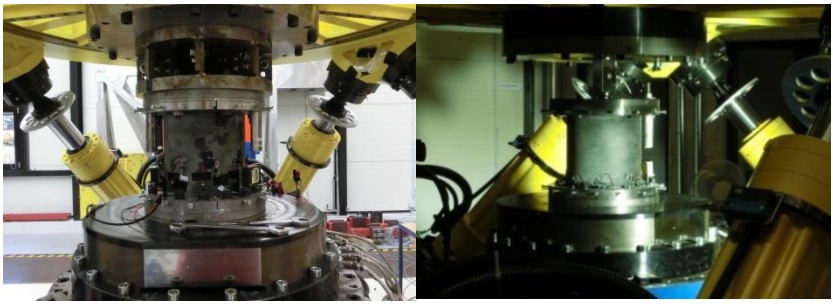

Figure 5-27 Test setups, clamped (left), simply supported (right)

5.5.3 Tests in the elastic regime

Prior to the buckling tests, all cylinders are tested in tension and compression in the elastic regime with a clamped support arrangement (Figure 5-26 and Figure 5-27, left). For tension tests the applied load is manually restricted to 30 kN, for compression tests to -15 kN. For each test, the load-displacement curve is recorded and after reaching the chosen limit, the cylinder is unloaded. Each loading condition is repeated five times per cylinder.

The corresponding stress-strain curves are used to compute the global structural stiffness. Due to an observed inhomogeneous stress state, the stiffness is derived by averaging over all stress strain curves measured per cylinder.

Due to the applied low load level, the strain range chosen for evaluation is between 0.01 and 0.03 %. The ratio of computed compression to tension modulus is presented in Table 5-10 and generally shows a high agreement.

Table 5-10 Ratio of computed compression to tension modulus

Cylinder	1.1	1.2	1.3	1.5	1.6	
compression to tension modulus	0.96	0.98	1.00	1.06	0.98	
Cylinder	2.1	2.2	2.3	2.4	2.5	2.6
compression to tension modulus	1.05	0.92	0.93	1.03	0.99	0.93

Only cylinders Z1.1-Z1.3 had 8 strain gauges applied to them so sufficient data for averaging to realistic absolute stiffness value was possible. These results are given in Table 5-11.

Table 5-11 Structural stiffness computation

Cylinder	1.1	1.2	1.3
Compression modulus	50.2	50.7	52.1
Tension modulus	52.5	51.5	51.9

5.5.4 Buckling tests

The expected buckling load is initially computed analytically according to WIEDEMANN [Wie07] (Equation (2-4)) using nominal values (Table 6-1 and Table 6-2) and resulting in 71.6 kN.

Buckling tests are carried out displacement controlled. Load application stops in case a significant loss of compression force is measured.

The maximum loads that the structures sustain are read from the measured load displacement curves and are summarised in Table 5-12 [Sch15]. The COV of 3.96 % is quite low and within a similar order of magnitude as the 10 nominally identical cylinders tested by DEGENHARDT [Deg10], which showed a COV of 5.5 %.

Table 5-12 Buckling loads

Cylinder	1.1	1.2	1.3	1.5	1.6	2.1	2.2	2.3	2.4	2.5	2.6
Buckling load [kN]	60.2	57.4	62.1	61.9	60.4	58.8	61.7	60.5	56.2	57.7	55.4
μ	59.3			COV [%]	3.96						

5.5.4.1 Load imperfections

The shear loads acting on the cylinder at the moment of its respective highest load capacity are depicted in Figure 5-28. A comparison of the resulting shear vectors leads to a mean shear load of 3.1 kN with a standard deviation of 0.4 kN.

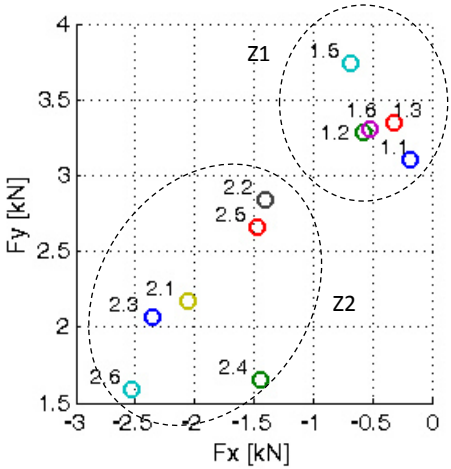

Figure 5-28 Measured load imperfections at buckling [Sch15]

A reason for the occurring load imperfection might be that the drill holes of the attachment rings are centred with some tolerance, so that the position of the ball socket connection also has some tolerance. Since fewer screws have been used for the attachment of set 2 of the cylinders, this could explain the larger scatter of load imperfections.

5.5.4.2 Optical high speed measurements

Buckling test measurements were complemented by recording with a CamRecord 5000 high speed camera at a frame rate of 8000 f/s [Opt13]. The videos reveal that almost all buckling failures initiate with a single buckle in close vicinity to the lower mounting. The buckles then quickly propagate until the post-buckling pattern is visible at mid-height of the cylinders (Figure 5-29).

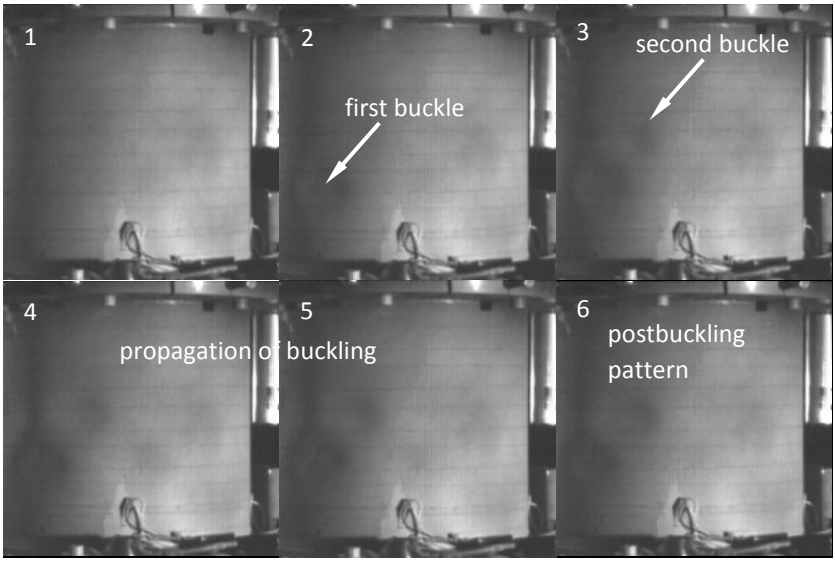

Figure 5-29 Onset of buckling observed via high speed camera (Z2.2) [Sch15]

5.5.5 Thermography

Pulse Phase Thermography is a NDT technique in which a thermal pulse is applied to a specimen and the thermal response is measured by an infrared camera. Any subsurface defects will disturb the heat flow and will appear as local hot or cold areas on the resulting temperature images.

Images from eight different angles of cylinders of set 2 have been taken prior and after buckling tests. For set Z1 pictures were taken after the final buckling test only. The equidistant lines visible on all images result from peel-ply leftovers.

Typical appearances of the thermography analyses are depicted in Figure 5-30. Almost no defects are observed in the cylinders of set Z1 (Figure 5-30, left). In contrast, the thermography analysis of set Z2 shows multiple white lines oriented at +30° (Figure 5-30, right).

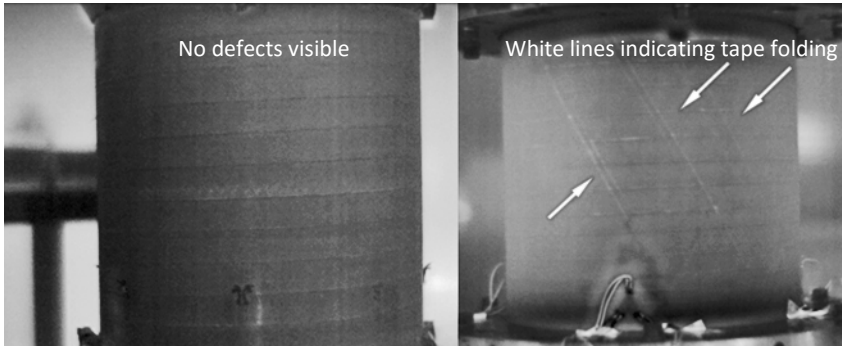

Figure 5-30 Thermographic comparison of Z1.1 and Z2.1 (at position 90°) [Sch15]

After discussion with the manufacturer it became clear that these lines indicate longitudinal folding of slit-tape segments. Thus, there are local thickness increases and epoxy-rich areas adjacent to it.

Pictures taken after buckling indicate that for cylinders 2.1 and 2.4-2.6, the observed white spots, indicating delaminations, occur in direct proximity or between these flaws, as depicted in Figure 5-31 for Z2.5. The appearance of these delaminations between flaws correlates with lower buckling loads below the mean. Thermography analysis of the cylinders that achieved buckling loads above the mean showed no initial flaws and in case of two cylinders (Z1.1, Z2.3) no delaminations after buckling at all.

Regarding the position of delaminations, a comparison with the buckling pattern recorded by the Aramis system and depicted in Figure 5-31 for cylinder 2.5 shows the delaminations to occur at points of reflexion of radial displacement curves, the sharp kinks between minimum and maximum deflection.

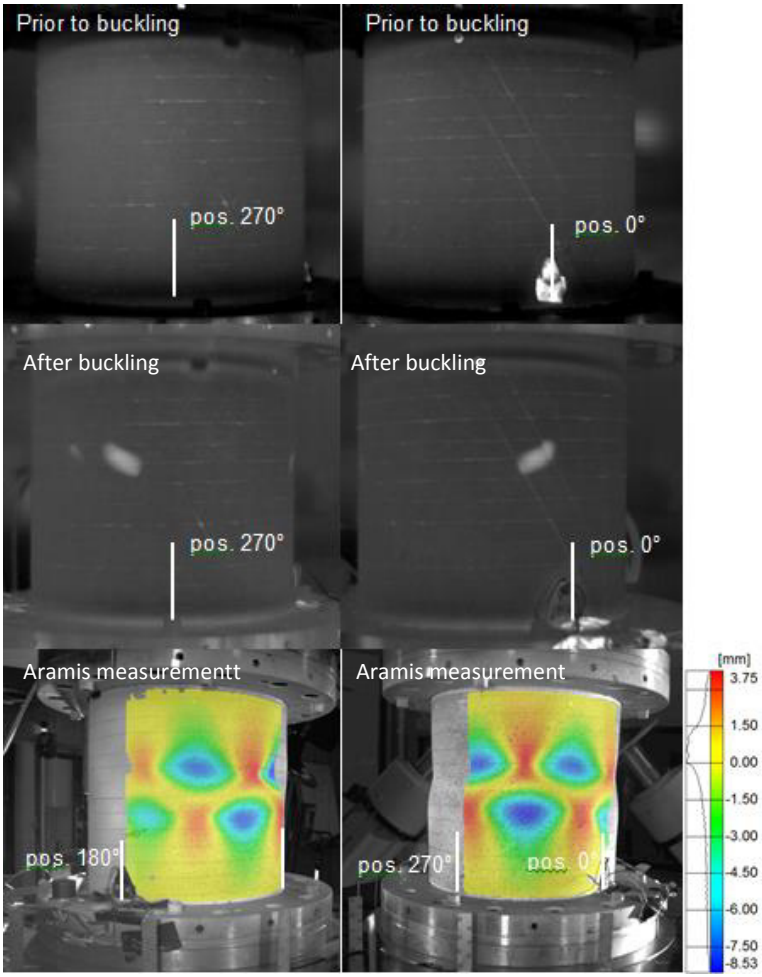

Figure 5-31 Thermography and postbuckling pattern of Z2.5 [Sch15]

Cylinder Z1.2, the only one out of the first set with a buckling load below 60 kN showed no pronounced fibre lines that might indicate flaws. However, a very large delamination area is detected oriented in 30°-direction along the fibre direction, thus indicating an area of low cohesion (Figure 5-32).

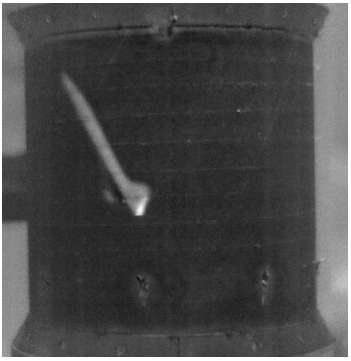

Figure 5-32 Z1.2, delaminated area [Sch15]

5.5.6 Multiple buckling

Several cylinders are tested repeatedly in axial compression. The test set-up is not changed compared to the single buckling tests, except that the Aramis system is only measuring in the postbuckling regime.

For cylinder 1.6, the set-up is changed after 11 tests with the last four buckling loads being almost equal in magnitude. The load introduction is changed to the fixed mounting and three more buckling tests are performed.

Figure 5-33 shows the decline of buckling load in the subsequent tests after the first buckling test. After a certain number of tests that varies individually for each cylinder, the curve suggests that a plateau of bearable buckling load (difference less than 2%) is reached. The buckling load level achieved here in % of the load reached in the respective first buckling is summarised in Table 5-13 and lies between 70-90%.

Table 5-13 Buckling load at plateau level in % of first occurring buckling load

1.1	**1.2**	**1.6**	**2.2**
69%	87%	73%	70%

The Aramis measurements show a two-row buckling pattern that moves slightly after the third test to the top – a former depression is now deformed outwards and conversely. A correspondence between switch in the mode and decrease of buckling mode cannot be found.

The change of mounting for Z1.6 leads to a significant increase in buckling load from around 45 kN to about 55 kN, the latter forming a plateau again for three subsequent

tests. The corresponding Aramis-measurement, depicted in Figure 5-33, also shows a two-row pattern with depressions and heights being situated close together.

For cylinder 2.2 an additional thermography measurement has been performed after each test. The resulting pictures are assigned to the corresponding test in Figure 5-34. No delaminations are present prior to testing.

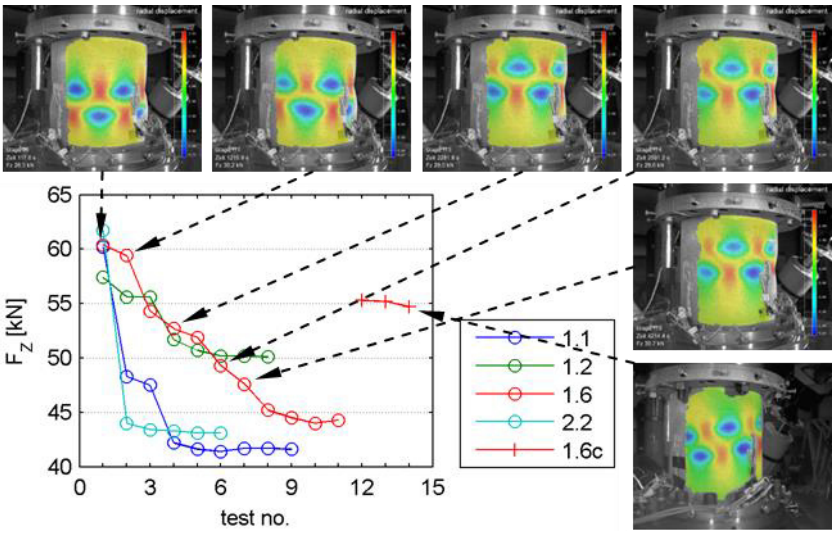

Figure 5-33 Buckling loads of cylinders tested repeatedly, postbuckling pattern Z1.6

After the first buckling test, a delamination area is observed, oriented at 60° with respect to the z-axis of the cylinder. The size of the delamination increases slightly after the second test: an additional, slightly fainter spot is visible that is oriented approximately at -30° with respect to the cylinder axis (marked in second picture in Figure 5-34). From the second test onwards, no growth of the delamination is observed. Correspondingly, the buckling load drops significantly after the first test from 61.7 kN to 44 kN, the last four tests show almost identical buckling loads, varying between 43.4 kN and 43.1 kN.

The buckling pattern itself does not change, but the buckles are deeper for the tests following when compared to the first one (Figure 5-35).

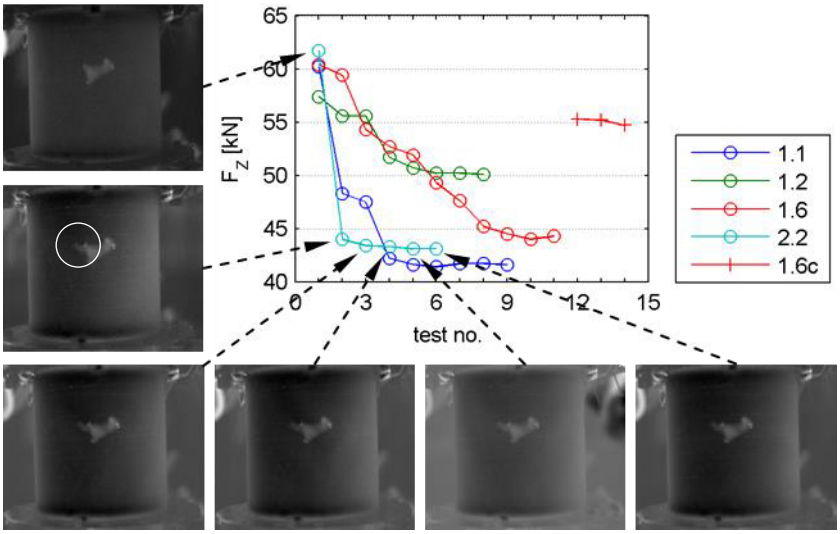

Figure 5-34 Thermography of cylinder 2.2 at 270° after each buckling test

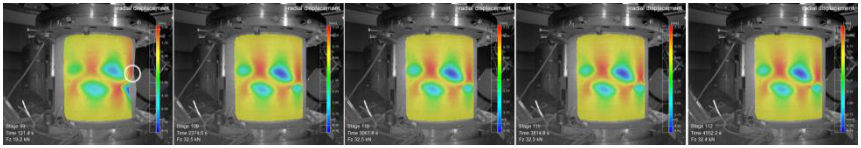

Figure 5-35 Postbuckling patterns of cylinder 2.2 after each test

All cylinders tested multiple times showed significant reduction in buckling load. However, the four cylinders under investigation showed very different behaviour when it comes to a comparison of the load reduction in relation to the number of tests. While cylinders 1.1 and 2.2 reach a certain load level quickly (Z1.1 after 3 tests, Z2.2 after the first test), Z1.2 and 1.6 reach the plateau gradually after 5 and 8 tests respectively.

In situ thermography is undertaken for Z2.2 only. In that case, the plateau is reached after the first test. It seems plausible, that if the damage in the structure does not grow, the structure behaves in the same way repeatedly, leading to similar buckling loads, described as plateau here.

The white circle in the left picture of Figure 5-35 shows the position of the delamination corresponding to thermography pictures of Figure 5-34. The delamination hence occurs at the edge of the buckle where the deformation gradient has a maximum.

5.6 Summary and discussion

Although optical thickness measurements were taken for cylinders of set Z2 by using the ATOS system to measure the inner and the outer surface, thickness measures were evaluated by analysing micro sections in order to identify and leave out the outer resin layer in further computations. This was considered necessary since the resin layer does not contribute to the load carrying capacity of the cylinders.

The analysis of micrographs generally showed a good quality of the cylinders in terms of void content and fibre volume fraction. While the analysis of specimens from set Z1 and set Z2 showed strong similarities, the coupon specimens showed remarkable deviations although an effort was made to resemble the manufacturing process of the cylinders. However, since the manufactured sheets needed to be straightened and the edge constraint were missing during the curing process, the sheet material could spread and bleed resulting in thinner layers and higher fibre volume fraction as compared to the cylinder specimens. The fibre orientation showed slightly higher scatter which might be due to the manual handling during the straightening process.

The autocorrelation analysis showed very low absolute values above a lag length of 62.5 µm. Also, correlation of thickness and fibre volume content was not found on the scale considered (up to 1000 µm). These two possible correlations are hence neglected in the Monte Carlo simulations.

The outer resin layer that stems from the manufacturing process influenced the optical measurement of the outer surface on a small scale. The same accounts for the peel ply fibre that stuck to the surface in a regular pattern. For the analysis of the geometric imperfection these very short-waved influences can be filtered by reducing the number of Fourier coefficients used to approximate surface geometry (refer to Appendix A7).

The power spectral analysis shows how the spectrum of the cylinders is clearly dominated by the first three to four half-waves. This dominance by low half-wave numbers was also found by [Kep13].

Although it is shown that the *rms* value of the geometric deviations from the perfect cylinder surface vary with height due to the potting process, a mean *rms* value is calculated in order to be able to compare to data found in literature.

The structural tests in the elastic regime showed a high compliance between structural tension and compression stiffness. Regarding buckling tests, high speed shootings show the inition of buckling at a single buckle. Thermography shows delaminations after buckling that occur preferably close to manufacturing flaws in the case of the second set of cylinders. To investigate the relation between occurring delamination and reduc-

tion of buckling load, the in situ observation should be employed for future buckling tests.

Notable is also the increase in buckling load by about 22 % when changing from a load introduction that allows tilting at buckling to a “clamped” setup where the cylinder is effectively kept in straight position. This effect should be considered when evaluating test data as basis for practical designs since there the structure will tilt at buckling.

The cylinders tested contribute to the creation of a database for CFRP cylinders close to practical applications. This is important since the layup and manufacturing method can have a large influence on the geometric imperfections.

6 Numerical analysis

Within this section the structural tests are recomputed deterministically using finite element methods and compared to the test results. The role of the stiffness of the cylinder mounting is treated separately.

6.1 FE-Modelling of structural tests

The role of the level of detail regarding modelling of boundary conditions is investigated using four different approaches that are compared to the standard procedure of using clamped end conditions for the cylinders. Cylinders are always modelled using S4R shell elements, and a load controlled non-linear computation is performed. The modelling of the clamping condition is varied only. The models used are described hereafter.

6.1.1 General remarks

Within the finite element code ABAQUS/Standard, a four node shell element with reduced integration (S4R) is used to represent the cylinder shell wall. A convergence study was performed to determine the number of elements to be used. 214 elements in axial direction and 722 in circumferential direction were used for discretization.

A nonlinear, load-controlled quasi-static analysis is performed using the well-known Newton-Raphson method and using the *static stabilize* option in Abaqus (damping factor 1e-6). The computation fails to converge at the buckling point where no further load increase is possible. Cross check calculations were performed using displacement controlled procedure to compute into the postbuckling regime and compare the results, but the postbuckling regime itself was not further investigated.

Dimensions and material properties used for the FE-models are the mean measured values as summarised in Table 6-1, line two.

Table 6-1 Nominal and mean measured data

	radius [mm]	thickness [mm]	layup	free length [mm]	total length [mm]	E_L [GPa]
nominal	115.00	0.81	$[90/+30/-30]_S$	215	255	58.7[1]
measured mean	114.86	0.80	as built; Refer section 2.1.2	-	-	46.8

[1] *from classical lamination theory and [Hex14a], [Hex14b]*

For the deterministic computation of tested cylinders, radii as measured and presented in Table 5-8 (page 70) are used.

The values for longitudinal, transvers and shear stiffness are adjusted to achieve the laminate stiffness of 46.8 kN. The used stiffness values are given in Table 6-2.

Table 6-2 Lamina stiffness values

E_{11} [GPa]	E_{22} [GPa]	G_{12} [GPa]	ν_{12} []
122.5	11.0	3.25	0.27

6.1.2 Imperfections

A plot of the resulting shell-wall mid-surface imperfection is depicted in Figure 5-21 with the issue of peel ply leftovers visible. To filter these artificial thickness increases for the FE-model, the measured imperfection data has been Fourier transformed using a double cosine representation (refer to Appendix A7). Following a convergence study, a representation up to 8 half-waves in axial and 24 in circumferential direction was chosen.

The resulting imperfection pattern of the unwound cylinder is plotted in Figure 6-1.

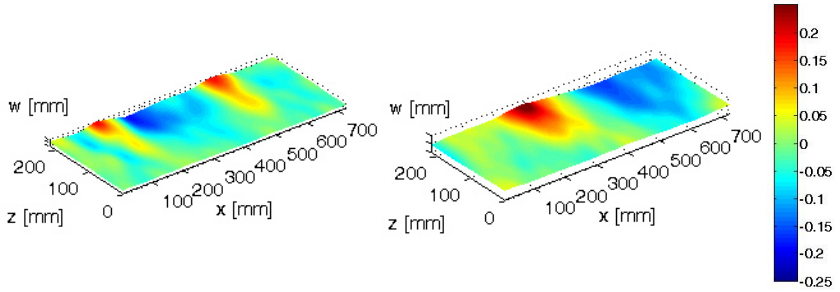

Figure 6-1 Approximated imperfection patterns of Z 1.1 (left) and Z 1.2 (right)

Using these functions, a mesh for implementation in the finite element program is created.

The load imperfections considered in the FE-models are applied according to their proportion with respect to the measured axial buckling load.

6.1.3 Reference model O, clamped edge condition

For realisation of the boundary conditions of the reference model, the bottom node line and top node line have been coupled rigidly to two master nodes, respectively. The master node controlling the bottom nodes is constrained in all six degrees of freedom. The master node for the top nodes is not constrained to allow for load imperfections. However, through the rigid connections to the master node, independent local rotations of the top nodes are effectively restricted. Load is applied through the master node. A typical resulting postbuckling mode is depicted in Figure 6-2.

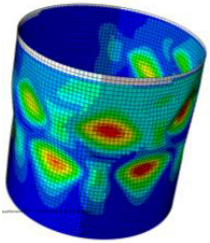

Figure 6-2 Typical buckling mode

6.1.4 Comparison of force strain curves using reference model

The reference FE model described in the previous sections is used to generate force strain curves of cylinders Z1.1-Z1.3. These three cylinders are used due to the high

number of strain data available from eight strain gauges per cylinder (refer 5.5.1). To be able to compare the data, the strain data of the FE-models is read from elements resembling the positions of the strain gauges (marked red in Figure 6-3).

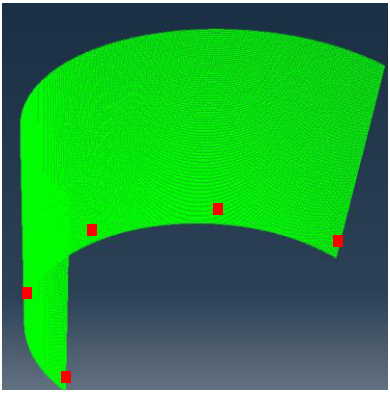

Figure 6-3 Elements used to read out strain data on half-model

The resulting force-strain curves from the non-linear analysis are compared against the experimental measurements in Figure 6-4 to Figure 6-6. Colours of the curves match the corresponding positions. For cylinder Z1.3 (Figure 6-6) the curves are in fairly good agreement. The inhomogeneous strain state, which is caused by the load imperfections, is obvious due to the unequal trends of the curves. This fan out of the curves is more pronounced for cylinder Z1.1 (Figure 6-4), where there is still good agreement regarding the buckling load, and even more for cylinder Z1.2 (Figure 6-5). Here, the maximum strain during the experiment reaches almost -0.4 % while the numerical prediction lies at -0.26 %.

The curves of cylinders Z1.1 and Z1.2 indicate that a small additional moment was present during the experiment that was not covered through the application of shear loads on the top master node.

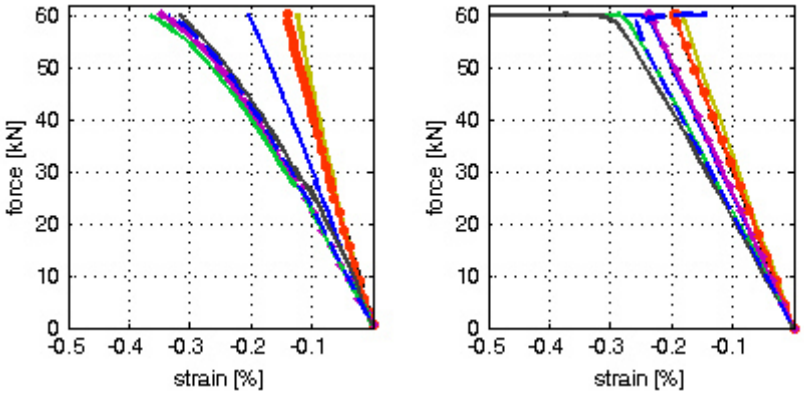

Figure 6-4 Z1.1 force strain curves, experiment (left), FE model (right)

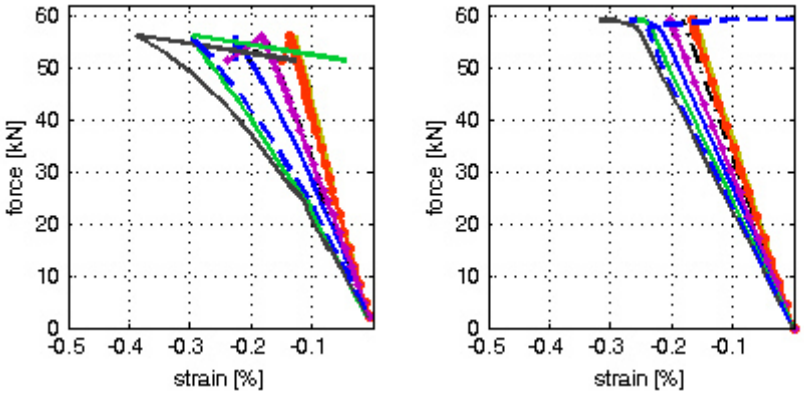

Figure 6-5 Z1.2 force strain curves, experiment (left), FE model (right)

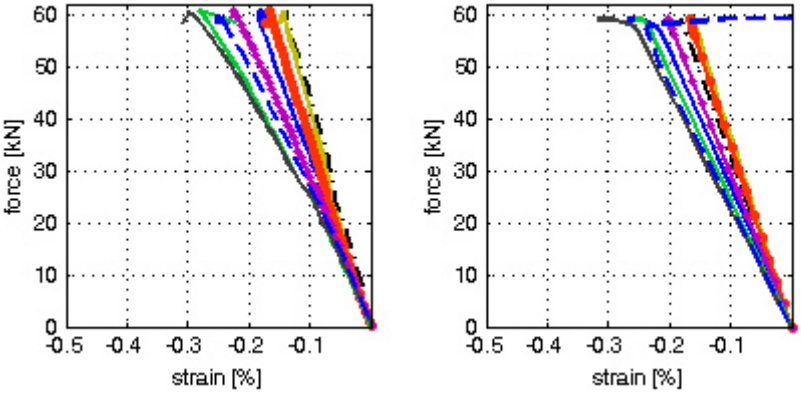

Figure 6-6 Z1.3 force strain curves, experiment (left), FE model (right)

6.1.5 Model A: 3-D modelled epoxy mass and steel ring

In model A, the clamping condition as depicted in Figure 5-5 is modelled using C3D8R volume elements for the epoxy. The steel ring is simplified as rigid body elements (R3D4) due to its very high stiffness compared to the CFRP-cylinder and the epoxy used for embedding it (Figure 6-7). Due to the application of release agent to the steel parts, a *hard contact* restraint is used to define contact behaviour between the steel ring and the cylinder as well as thesteel ring and the epoxy. This definition implies that no penetration is allowed at each constraint location and the contact pressure is transmitted without limitation when in contact. A friction restrained is considered.

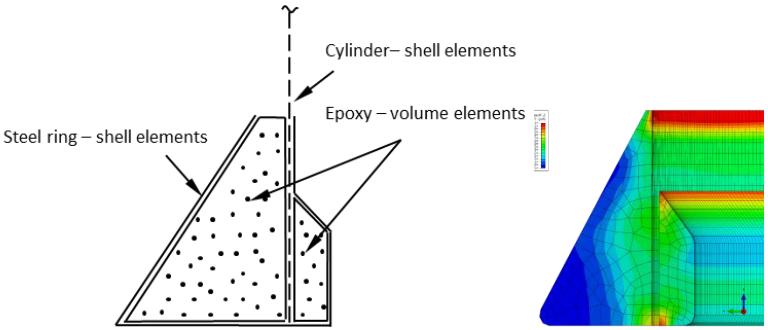

Figure 6-7 Idealisation of model A

6.1.6 Model B: Model A + consideration of pre-strain caused by cylinder clamping

The same idealisation of the structural parts is used as for model A. However, for the geometry of the cylinder the contour of the cylinders of set 2, that have been optically measured before mounting, are used (Figure 5-20, left). The high deflections present in this ovalized form leads to an overlap with the inner steel ring in some areas and a complete clearance in other parts.

In the first load step this contour is shrinked on the lower steel ring but the rest of the cylinder is able to deform. In Abaqus this process is realised through the automatic shrink fit method which assigns a different displacement to each slave node that is equal to that node's initial penetration (Figure 6-8).

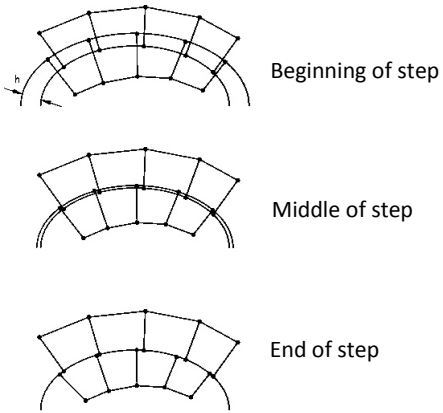

Figure 6-8 Schematic of resolving overclosure in Abaqus [Sim15]

In the second load step, the procedure is repeated for the application of the upper steel ring. Thus, the contour is forced into a cylindrical shape and leads to a certain pre-stress state of the cylinder (Figure 6-9).

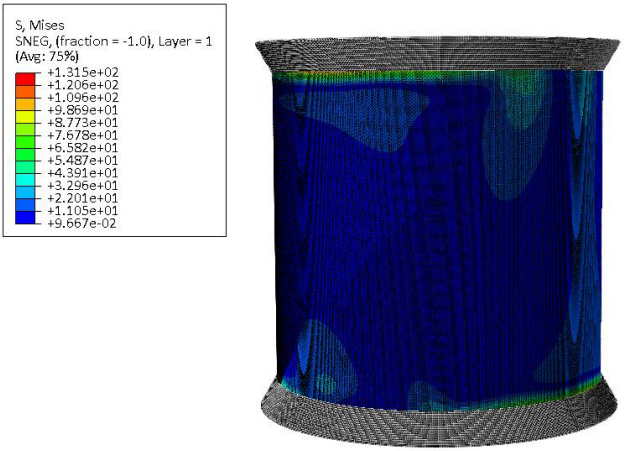

Figure 6-9 Typical pre-stress state of model B

The results from these two load steps are now transferred to a new simulation during which loads are applied and the buckling loads are computed.

6.1.7 Results

The results of the computed buckling loads using different modelling techniques for the boundary conditions are given in Table 6-3 along with the corresponding test results. Only very slight differences are found for model A compared to the reference model employing clamped edge condition (below 1 kN or 1.7 %). Buckling loads computed by the model considering pre-strain from overclosure are scattered around the results of the reference model and differ by a maximum of -2.7 kN and +1.12 kN for cylinder 2.4. Standard deviations of model O and A underestimate the test result by approximately 50 %. The mean values fit very well with the experimental result for all models. The good agreement of the standard deviation of model B suggests that half of the scatter of the buckling load might be caused by the pre-stress state.

Table 6-3 Computed buckling loads for different realisations of boundary conditions

	Buckling load			
Cylinder no.	Test result [kN]	Model O: clamped [kN]	Model A: detailed model [kN]	Model B: with over-closure [kN]
1.1	60.2	60.2	59.32	-
1.2	57.4	59.2	58.69	-
1.3	62.1	59.9	59.20	-
1.5	61.9	58.7	58.22	-
1.6	60.4	59.5	58.93	-
2.1	58.8	60.1	59.34	57.76
2.2	61.7	60.3	59.90	60.58
2.3	60.5	60.2	59.61	60.62
2.4	56.2	62.6	62.12	63.41
2.5	57.7	59.9	59.35	57.92
2.6	55.4	59.7	59.19	58.84
mean	59.3	60.0	59.4	59.9
standard deviation	2.35	0.98	0.99	2.14

6.1.8 Model C: Spring stiffness

Model C aims at a simplification of the modelling technique. Here, the epoxy and steel ring idealisation is omitted and the rotational flexibility of the real clamping condition is simulated through a spring stiffness, which allows each node to rotate around its tangential axis (Figure 6-10). In Abaqus, this connection is realised through a hinge connector that gets a certain stiffness assigned to the corresponding rotational degree of freedom in a local coordinate system that is defined for each node.

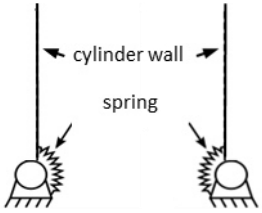

Figure 6-10 Idealisation of model C

The stiffness value is found by comparing the buckling loads computed with the ones determined through the detailed model A. Figure 6-11 shows the study performed for cylinder Z1.1 with the extreme cases of a simply supported and clamped edge condition corresponding to a spring stiffness of 0 and around 3000 Nmm/°, respectively. Up to a spring stiffness of 550 Nmm/° the increment chosen leads to a measurable difference in the buckling load. At larger values, the result approximates the buckling load computed with clamped edges.

Following this approach and identifying equivalent stiffness values for the whole cylinder set (refer to Table 6-4), a range of equivalent stiffness values is identified that is used for sensitivity analysis in section 7.1.1.

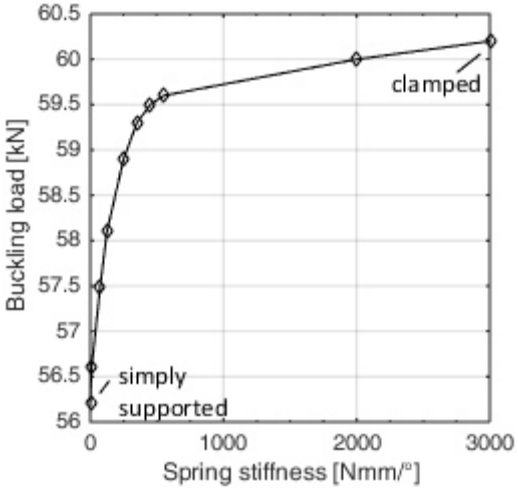

Figure 6-11 Influence of rotational spring stiffness on buckling load, Z1.1

Table 6-4 Spring stiffness values identified to match buckling load of detailed model

Cylinder no.	1.1	1.2	1.3	1.5	1.6	2.1	2.2	2.3	2.4	2.5
Spring stiffness [Nmm/ °]:	350	350	350	400	550	300	350	350	450	350

6.2 Model uncertainty

Five different models are set up to compute the resistance of the measured cylinders against buckling and to compare results against the buckling loads from the tests. The five models differ in the number of parameters considered (Table 6-5).

Table 6-5 Parameters considered in different models

Model number	Geometric imperfection	Load imperfection	Layup as built	Bedding of cylinders
1	x	x	-	-
2	x	x	x	-
3	x	-	-	-
4	-	x	-	-
5	x	x	-	x

The computational results for all 11 cylinders tested are depicted in Figure 6-12 as computed buckling load over tested buckling load. In case of agreement, the results would lie on the blue diagonal line representing a linear resistance model with zero error associated to it.

Model 3 (no consideration of load imperfections) computes similar results for all cylinders, indicating that the considered geometric imperfections have only minor influence on the scatter of the results. Model 4, which neglects geometric imperfections but incorporates load imperfections, shows a high degree of scatter with certain offset from the reference diagonal. Models 2 and 4 scatter around the diagonal, where for model 4 the numerical analysis significantly exceeds the test result for several cylinders. Models 1 and 2 show similar behaviour in terms of scatter around the diagonal.

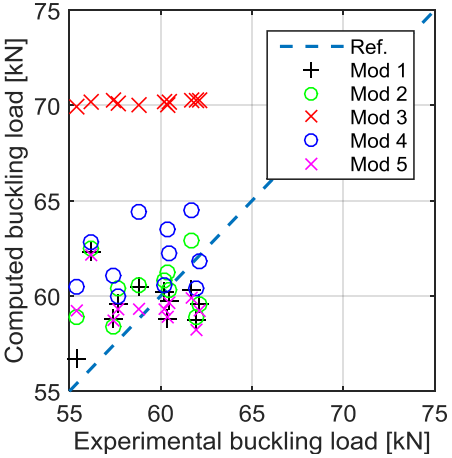

Figure 6-12 Model uncertainty

According to EN 1990 [EN 02], Annex D, the model uncertainty of each type of model can now be further quantified by analysing the mean value correction factor, denoted *b*, and the variance of the error term, V_δ. The factor b can be interpreted as the least squares best-fit to the slope of the resistance model, given by the following relation between experimental resistance r_{ei} and theoretical resistance r_{ti}:

$$b = \sum_{i=1}^{n} r_{ei} r_{ti} \sum_{i=1}^{n} r_{ti}^2 \qquad (6\text{-}1)$$

The error term V_δ is given through:

$$V_\delta = \sqrt{\exp\left(s_\Delta^2\right) - 1} \qquad (6\text{-}2)$$

Refer to EN 1990 [EN 02], Annex D for further details.

The results are summarised in Table 6-6. The variation of the error terms does not vary largely between the models. With values between 3.88 % for model 3 and 4.87 % for model 5, the variance associated with the model uncertainty is in the range of the measured buckling load scatter which showed a coefficient of variance of 3.96 %.

The analysis shows that for the cylinders investigated, the highest loss in resistance prediction accuracy occurs for model 3 and is due to the negligence of load imperfections occurring during the cylinder tests. Here, the mean value correction for the resistance is 15 % lower than for model 1. In comparison, the influence of geometric imperfections, illustrated by the difference of results between model 4 and 1, is small

with only 3 %. The consideration of the layup changes the model bias by only 1 % and reduces the variance of the error term slightly. Highest b-value is achieved for model 5 using a detailed modelling approach for the cylinder mounting (section 6.1.5).

Applying this method to the test results of DEGENHARDT ET AL. [Deg10] and computations made by BROGGI [Bro11] it is found that the introduction of thickness imperfections leads only to minor reduction of the model bias. HÜHNE [Hüh05] reached the maximum b-factor when including geometric imperfections but also high variance of the error term, indicating that this model might also be improved by consideration of additional parameters. A comparison of these results with non-linear computations for the perfect geometry shows that the influence of the geometric imperfections measured has a much larger influence than for the cylinders investigated within this study. This is expected due to the lower radius to thickness ratio as well as the lower imperfections associated with the cylinders. EN 1990 [EN 02] offers a transparent way of quantifying and comparing these influences for different studies, whereas the results always have to be assessed in the context of the geometries and manufacturing methods used.

Table 6-6 Model uncertainty characterisation

	Schillo [Sch15]					Degenhardt [Deg10], Broggi [Bro11]		Hühne [Hüh05]	
	11 nominally identical cylinders					10 nominally identical cylinders		8 cylinders, 5 different layups	
	Model type								
	1	2	3	4	5	Geom. imp	Geom. Imp., thick. imp.	Geom. imp.	Perfect geom.
b	0.99	0.98	0.84	0.96	1.00	0.75	0.76	1.00	0.88
V_δ [%]	4.81	4.53	3.88	4.22	4.87	7.72	7.59	10.3	7.89

Within this work, the mean shear force appearing at buckling that is measured, causing additional moments, is about 5 % of the mean buckling load but making up for 15 % of model bias. To make statements about prediction models for unstiffened cylinders, it is very important to consider this parameter.

6.3 Summary and discussion

Predictions for the resistance of all cylinders tested are made, using four different FE-models with a varying number of parameters considered. While the consideration of geometrical imperfections only increased the model prediction agreement by 3 %, the largest contribution comes from the introduction of load imperfections which made up for 15 % of the model bias. The comparably small influence of the geometric imperfections is remarkable since there is commonly a much higher load reduction associated with it (refer to section 2.2.1). The NASA SP predicts a higher susceptibility towards geometric imperfections with increasing R/t ratio (Figure 2-5, page 14). With a nominal R/t ratio of 147, the cylinders considered are situated at the far left of the NASA SP design curve but a significant knockdown would still be expected (γ=0.52, refer to section 2.4.1). In addition to the expected lower influence the main reason could be associated with the quasi-isotropic layup and the manufacturing process, leading to decreased residual stresses, low tolerances of the geometry and long-waved imperfection modes rather than short-waved. Hence, a general assessment of the sensitivity of unstiffened cylinders towards geometric and load imperfections should include a wider range of R/t values and different manufacturing methods.

The mean vector of transverse load imperfections occurring during test was measured to be around 3 kN, corresponding to approximately 5 % of the axial load applied and contributing by 15 % to the model bias. No data is available to compare this amplitude with other test setups. It is considered to be higher than other test facilities that are purpose-built for uniaxial compression tests of unstiffened cylinders. Since small load imperfections can have large influence on the buckling load, these forces should be measured during test.

Despite the fact that no material inherent flaws and the simplification of rigidly constrained cylinder edges are considered, the prediction agreement for all models considering load imperfections was very high. However, further research should investigate the sensitivity of the models with respect to the thickness variation that has only been included deterministically in these models, as well as an appropriate representation of the cylinder stiffness from coupon tests.

7 Reliability based calibration of safety factors

The following sections describe the Bayesian approach to derive and update calibrated safety factors for the structural and model uncertainty. Parts of this section are also treated in [Sch17].

7.1 Uncertainty analysis

The first step in the development of a reliability based design concept is to identify the uncertainties associated with the input parameters of the analysis. These uncertainties are described through distribution functions than can be simplified to the first two stochastic moments in case normal distributions are presumed. These moments have been measured for material related uncertainties in section 5.3 and 5.4.

7.1.1 Identification of relevant parameters

After identifying uncertainties of the input parameters it is helpful to classify these parameters in terms of their relevance for the output parameter. A Morris screening ([Mor91], refer to section 3.2) is performed to identify those parameters that will be relevant for future Monte Carlo analysis. These parameters of interest are summarised in Table 7-1 and are given along with the chosen perturbation factors *unc*.

Table 7-1 Parameters used for Morris screening

	E1 [GPa]	E2 [GPa]	phi_1 -phi_6 [°]	Fx [N]	Fy [N]	k [Nmm/°]	t [mm]
Nominal values	122.5	11.0	$[90,30,-30]_S$	-1085	2390	350	0.133
Perturbation factor unc [%]	5	5	10	62	43	50	2

The perturbation can be interpreted as picking randomly from a uniform distribution with range from minus the percentage of the nominal value to plus the percentage of the nominal value. A high perturbation hence represents a high uncertainty, either due to high scatter of the quantity or due to lack of information. While for E1 and E2 values could be chosen that are in the range of measured coupon values, a comparably high and conservative value of 10% was chosen for the layer angles. The apparent shear loads introduced at the load introduction point of the cylinders are deduced from experiments. The rotational stiffness of the lower boundary conditions is truncated by a value of 50% since here no information about true scatter is available.

The variation of the thickness will typically have a large influence on the buckling behaviour of unstiffened shells. Within this screening, the dependence between thickness and Young's modulus E1 through the fibre volume fraction is neglected. Hence, the increase in thickness leads to a proportional increase in stiffness, leading to a slight overestimation of the influence of the thickness. This is why a comparably low perturbation of 2% is chosen for that quantity.

The finite element model used for this analysis uses the geometry of one of the test cylinders (Z1.1) and a mesh of 215x722 S4R shell elements. To realise the investigation of the influence of the boundary stiffness, boundary conditions of the lower end of the cylinders are modelled using a spring stiffness as described in section 6.1.8.

390 simulations were run including 30 repetitions (refer to section 3.2). The elementary effects computed for those simulations are shown in Figure 7-1. We recall that the EEs are computed using Equation (3-14) and are evaluated in terms of their mean and standard deviation (Equations (3-1) and (3-2)). A wide spread of the EEs combined with very low values and spreading around zero indicate a small influence on the output value considered. This can be observed for the four layer angles phi2 to phi4 while the 90° angles phi1 and phi6 are more clustered around an absolute higher value. Although the EEis of E1 and t seem to be spread out, their values are comparably high and actually spread about a small range. Small values are found for E2 and especially for the boundary stiffness k, which showed almost no influence within the range considered.

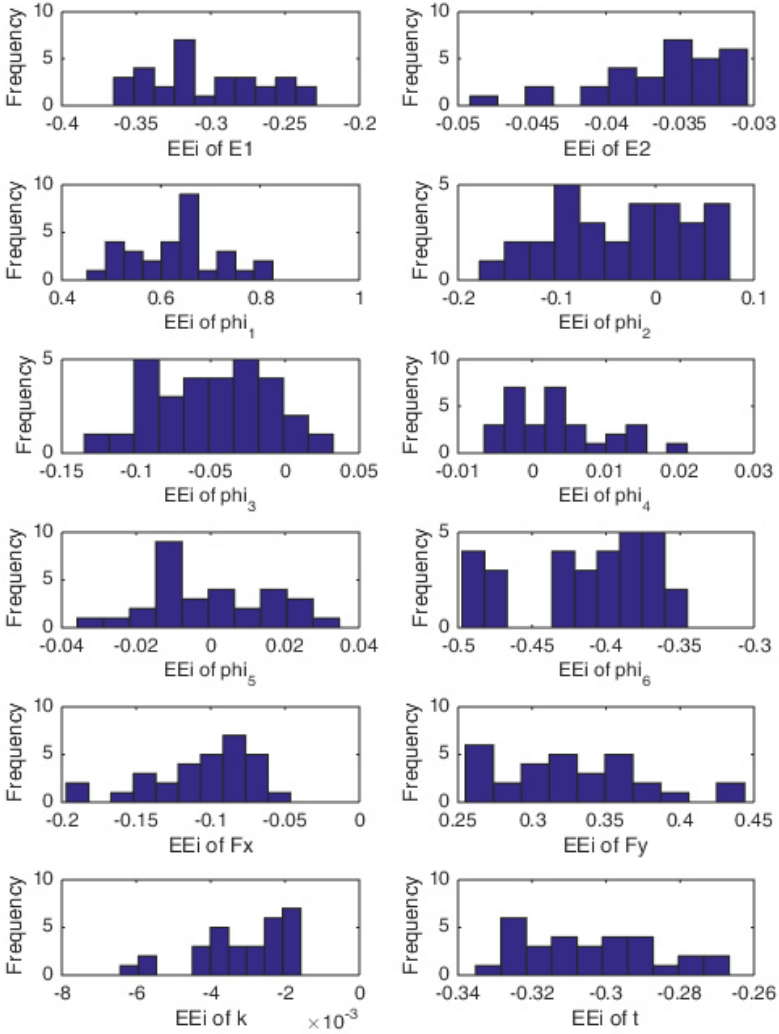

Figure 7-1 Elementary effects

Figure 7-2 shows the standard deviation computed for the EEis computed over the mean values. A high standard deviation combined with a high absolute mean value indicates that the perturbations lead to a high spread in observed buckling loads, whereas a high standard deviation combined with a low mean value has no significant

influence. The parabola indicates a separation between relevant and less relevant parameters [Mor91], [Sin09]. It is formed through two lines that are computed as $Mean_i=\pm 2sem_i$ with sem_i being the standard error of the mean and estimated as

$$sem_i = \frac{\sigma_i}{\sqrt{r}} \tag{7-1}$$

Recall that *r* stands for the number of repetitions chosen for the sampling.

From this plot, parameters *E1, phi1* and *phi6* as well as *t* and the shear loads *Fx* and *Fy* are identified as necessary for further uncertainty analysis.

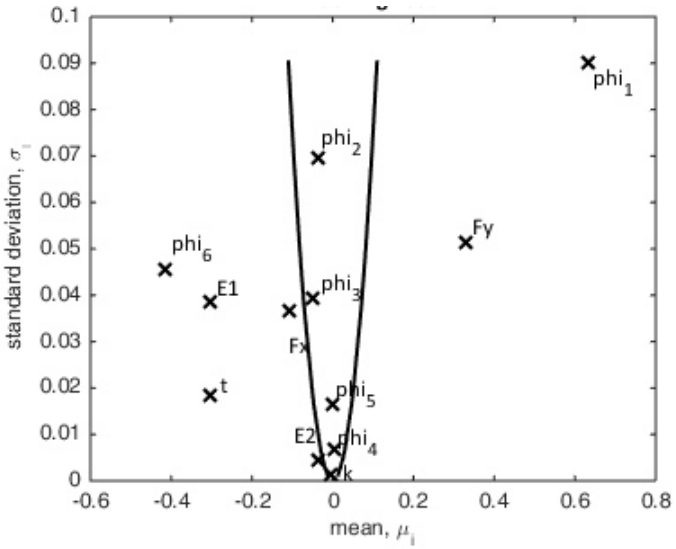

Figure 7-2 Standard deviation plotted over mean of EEis

7.1.2 Influence of *rms* of geometric imperfection

To analyse the influence of the *rms*-value at the pre-design stage, an FE-model is employed using the first four scaled eigenmodes as geometric imperfection (Figure 7-3). Discretization and boundary conditions are similar to the model described in section 6.1.3.

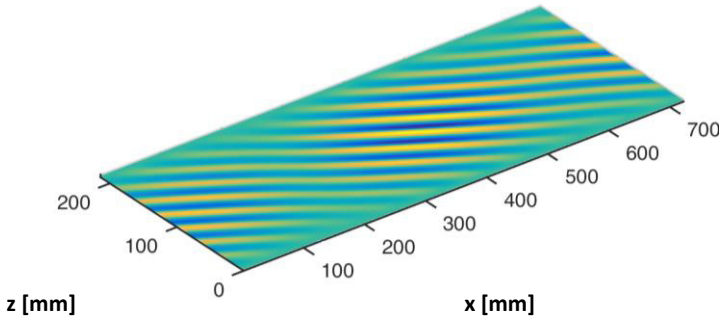

Figure 7-3 Unwound of scaled superposition of first four eigenmodes

The scaling factor for the modes is chosen in such a way that a specific *rms* value is achieved. Monte Carlo simulations are carried out with scattering material parameters at different *rms* levels and the resulting mean and standard deviations are depicted in Figure 7-4, showing the strong non-linear behaviour for *rms*-values higher than 0.04. The choice of the amplitude of the geometric imperfection is hence very critical.

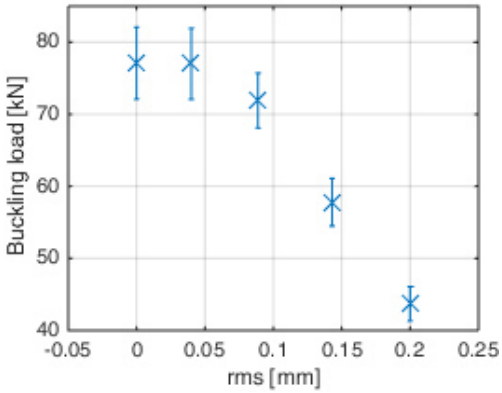

Figure 7-4 Influence of *rms*-value on mean and standard deviation of buckling load

7.2 Generation of similar geometric imperfection patterns

To generate representative artificial geometric imperfections, the Bayesian approach is applied to the Fourier coefficients used to approximate the measured cylinders [Sch15] assuming normal distributions and neglecting possible covariances. Each cylinder is characterised through two matrices that contain the amplitudes and the phase shift

angles of corresponding modes (refer to Appendix A7) respectively. Statistic parameters for a normal distribution are determined for each entry of the matrices based on the six measured cylinders of the first set. This method results in a mean and standard deviation for each coefficient. To create an artificial geometric imperfection, a random sample is drawn from a normal distribution with the derived characteristic values for each Fourier coefficient.

After the information of set Z2 becomes available, these parameters are then updated using the Fourier coefficients found for set Z2 using Equation (3-31).

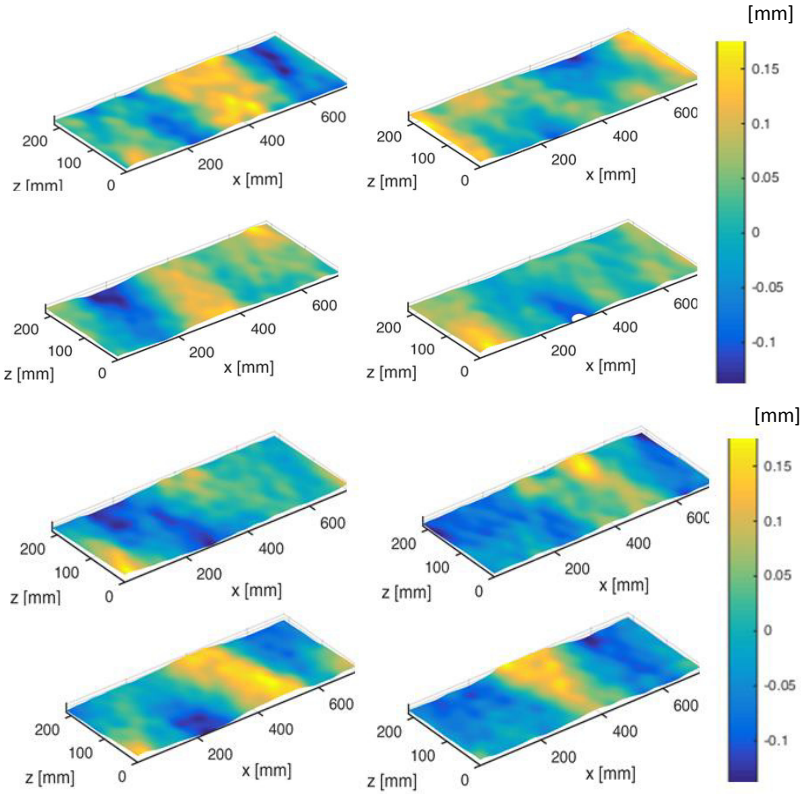

Figure 7-5 Realisations of artificial geometric imperfections

Figure 7-5 shows eight realisations of geometric imperfections created using this method.

7.3 Monte Carlo simulations

Monte Carlo simulations are performed to compute the distribution functions for the load carrying capacity, using three different model assumptions. The first model represents the preliminary design stage when only nominal data is available. In a Bayesian approach the second and third simulation utilise the preliminary assumptions as well as data available from set Z1 and set Z2, respectively.

7.3.1 Summary of uncertainties

For thickness and fibre volume fraction at the preliminary design stage, the nominal values are derived from [Hex11]. Scatter of fibre angle is taken from literature [Sic09] and an estimate of the transverse load is made based on a pre-test. If no information about the geometric imperfections is available, a common design approach is to apply a superposition of a number of eigenmodes to the perfect cylindrical shell. Experience or engineering judgement is necessary to choose the scaling factor (i.e. the amplitude) for the eigenmodes. For this analysis, the scaling factor is chosen to achieve a *rms* value of the deviations of 0.08 mm, based on cylinders AWCYL-92-1 to 3 investigated by Arbocz [Arb05]. Material uncertainties analysed in section 5.3 are reproduced in Table 7-2 along with the values for the load uncertainties (section 5.5.4.1) and the mean *rms* values of the measured cylinders.

Table 7-2 Uncertainties of relevant input data

	t [µm]		$phi_{1/6}$ [°]		FVF [%]		F [kN]		Geometric	
	µ	σ	µ	σ	µ	σ	µ	σ	µ	σ
Preliminary	820.0	40.0[1]	90.5[1]	2.0[2]	60.0	3.00[1]	3.00	1.00[1]	0.08[3]	-
set Z1	798.6	13.94	90.5[1]	1.74	61.0	2.00	3.39	0.25	0.075	0.013
set Z2	810.0	8.55	90.5[1]	1.80	59.8	2.97	2.92	0.36	0.081	0.027

7.3.2 Generation of input data

For the preliminary design stage the input data is identical to the values given in Table 7-2. When information about the first set of cylinders becomes available, this information is updated in the Bayesian sense (section 3.4) using Equation (3-34) with the

[1] Assumption from pre-test

[2] Assumption made from [Sic09]

[3] Assumption made from [Arb05]

preliminary assumptions about the distributions of the input parameters used as the prior distributions. A second update occurs as measurements concerning set Z2 are performed. These again use the previously updated statistics as prior information.
Figure 7-6 exemplary shows the resulting surface plot for the second update of the parameters for the thickness *t*.

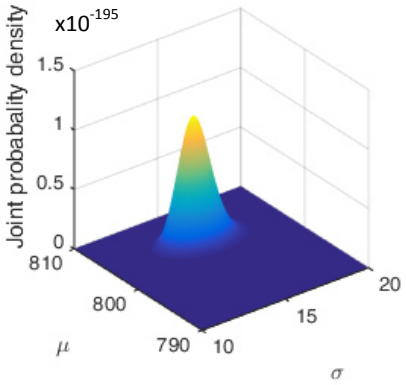

Figure 7-6 Surface plot for μ and σ of thickness

Due to the number of measurements taken, the updated values do not vary strongly from the overall mean taken over all measurements and given in the last row of Table 7-3.

The values of the *rms* for update 1 and 2 are computed from the *rms* of the geometric imperfections of all realisations of the corresponding Monte Carlo simulations and are slightly higher than the overall mean value of the measured cylinders.

Table 7-3 Updated input data for Monte Carlo simulation

	t [µm]		phi [°]	FVF [%]		F [kN]		rms [mm]	
	μ	σ	σ	μ	σ	μ	σ	μ	σ
Preliminary	820.0	40.0	2.0	60.0	3.00	3.0	1.0	0.0800	-
Update1 (set Z1)	799.0	14.55	1.74	61.1	1.83	3.3	0.4	0.0816	0.0158
Update2 (set Z2)	803.8	14.91	1.8	59.8	2.69	3.0	0.3	0.0838	0.0191
Overall μ / σ	803.8	13.18	1.6	60.4	2.45	3.13	0.39	0.0780	0.0205

7.3.3 Results of Monte Carlo Simulation

The resulting mean and standard deviation of the buckling loads computed at the three design stages are given in Table 7-4. In the preliminary design stage the buckling load is overestimated, mainly due to the nominal thickness value that was larger than the thickness measured for the cylinders.

Table 7-4 Results of Monte Carlo Simulations

	Computed buckling load [kN]		Test results [kN]		
	μ	σ	μ	σ	min
Preliminary	63.8	1.75	-	-	-
Update 1	58.7	1.41	60.4[1]	1.88[1]	57.4[1]
Update 2	58.9	1.39	59.3[2]	2.35[2]	55.4[2]
Frequentist	59.1	1.34	59.3[2]	2.35[2]	55.4[2]

Good agreement of the mean values is found with only 2.9 and 2.5 % difference compared to test results for the first and second update, respectively. The scatter is underestimated by 43 % but at low absolute values (1.39 kN compared to 2.35 kN for Update 2, refer to Table 7-4).

7.4 Determination of safety factors

Safety factors for designing the unstiffened shell structure are subdivided into a factor covering structural and material uncertainties (section 7.4.1) and a factor covering the model uncertainty (section 7.4.2).

7.4.1 Safety factor covering material and structural uncertainties

The safety factor covering material and structural uncertainties that has been modelled in the Monte Carlo simulation can now be calibrated according to a chosen target reliability level. For demonstration purposes, the β-value is chosen to be 3.09 and 2.33, corresponding to a structural reliability level of 0.999 and 0.990, respectively (on the basis of [Esn96]). Assuming normal distributions, the allowable buckling load at the

[1] Set Z1

[2] Sets Z1+Z2

design point can then be computed for each Monte Carlo simulation by rewriting Equation (3-24) as [EN 02]:

$$x_D = \mu_{MC} - \sigma_{MC}\beta \tag{7-2}$$

The partial safety factor is then given through [Fab02]:

$$\gamma_R = \frac{x_D}{x_{50\%}} \tag{7-3}$$

where x_D is the design point related to the β-value and $x_{50\%}$ is the characteristic value. In the case of stiffness and geometrical properties the characteristic value is commonly taken as the 50 % quantile [EN 02] .

The resulting safety factors are given in Table 7-5.

Table 7-5 Safety factor covering material and structural uncertainties

Design stage	Information source	$X_{50\%}$ [kN]	X_D [kN]	$\gamma_{R0.999}$ []	$\gamma_{R0.990}$ []
Predesign	Preliminary	63.8	58.3	0.91	0.94
Specific design	Z1	58.7	54.3	0.93	0.95
	Z1+Z2	58.9	54.6	0.93	0.95
	Frequentist	59.1	55.0	0.93	0.95

For a reliability level $\gamma_{R0.999}$, the value of 0.91 reflects the uncertainty at the preliminary design stage. With the availability of measurements from set Z1, this uncertainty reduces to 0.93, resulting from the lower scatter of the buckling load under the given scatter of input variables. Due to only small differences in the input data derived form set Z1 and updated with set Z2, the updated computation does not lead to a change in safety factor. The safety factor when considering the Monte Carlo analysis using averaged measurement data of set Z1 and set Z2 (denoted as Frequentist inTable 7-5) is also 0.93. At a reliability level of $\gamma_{R0.990}$, safety factors are show slightly increased values with identical tendencies.

7.4.2 Safety factor covering model uncertainties

The model uncertainty describes the degree of uncertainty related to deviation between model inference and the test result. This deviation can be caused by a lack of

information about input parameters, by negligence of relevant parameters or by the ability of the model to properly describe the physical effect.

A Bayesian model is set up to compute a safety factor describing the above mentioned deviation. This factor can then be updated in the light of new information available.

A multiplicative error model is employed, written as

$$Y = q \times e \tag{7-4}$$

q describes the simulated data, *e* is the error term and *Y* is the vector of test results.

Assuming lognormal distributions for *q* and *e*, the posterior distribution becomes also lognormal distributed and can be computed as

$$f_{\Theta|Y}(\theta \mid y) = \frac{f_{\Theta}(\theta) f_{Y|\Theta}(y \mid \theta)}{\int f_{\Theta}(\theta) f_{Y|\Theta}(y \mid \theta) d\theta'} \tag{7-5}$$

with θ being the estimator for the mean of the error term. Prior and likelihood functions are written as follows:

$$f_{\Theta}(\theta) \sim LogN(\mu_{\theta}, \sigma_{\theta}) \tag{7-6}$$

$$f_{Y|\Theta}(y \mid \theta) = \frac{1}{\sqrt{2\pi} q e \sigma_{\theta} \sigma_{q}} e^{-0.5\left[\left(\frac{(\log(e)-\theta}{\sigma_{\theta}}\right)^2 + \left(\frac{(\log(q)-\mu_q)}{\sigma_q}\right)^2\right]} \tag{7-7}$$

For the predesign stage, the mean error term is modelled using an uniformative prior via a uniform distribution ranging from 0.5 to 1.5. As a first guess, the knockdown factor given by the NASA SP could also be used. However, since this knockdown factor is associated with another computational method, an uniformative prior is chosen.

At the preliminary design stage, the safety factor is updated two times, with results from set Z1 and set Z2, respectively (Table 7-6). Thus, a safety factor covering the uncertainties related to the usage of nominal data is developed.

The posterior probability density function for θ is computed using Equation (7-6) and (7-4), whereas the integral in the numerator does not have to be solved according to the MAP rule (section 3.4.5). An uninformative uniform prior is chosen for the first update. The resulting posterior distributions are depicted in Figure 7-7 and the safety factor is computed as the 50 % quantile of the estimated mean model error [Fab02].

The most probable stochastic moments of Θ are read from the joint posterior distribution function (Figure 7-7). From the resulting lognormal posterior distribution function

the safety factor is computed as the 5 % quantile to account for the uncertainty of the model error.

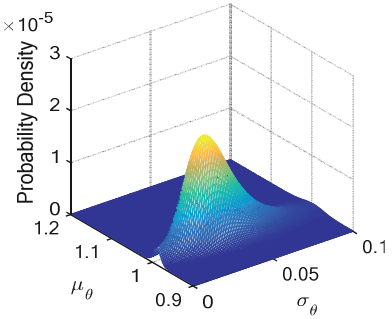

Figure 7-7 Probability density function of μ_θ and σ_θ

Lognormal distribution functions with characteristics of the test data and the data of the MC inference (Table 7-4, p.111) are assumed.

In the absence of any other information, the prior mean error term in Equation (7-4) for the predesign stage is modelled using an uninformative prior via a uniform distribution ranging from 0.5 to 1.5. Evaluating the probability density function gives a most probable value for the mean and standard deviation of the error term. From these, the 50 % and 5 % quantile are derived.

The computation is first run with respect to test results of set Z1 and then updated with respect to test results of set Z2. Each subsequent analysis uses the previous distribution function for the error term as the prior distribution.

At the preliminary design stage the resulting safety factor covers the model uncertainties related to the usage of nominal data. Since the test results of the second cylinder set Z2 showed slightly lower results compared to set Z1, the updated multiplicative safety factor is lower (0.87 as compared to 0.94 for the 5 % quantile).

For the specific design phase this effect can also be observed for the updating process but is less severe since the model inference is in high agreement with test results.

The updated safety factor at the 5 % quantile for the Bayes model is identical to the Frequentist model that gives a factor of 0.94.

Table 7-6 Safety factor γ_m covering model uncertainty

design stage	information source	prior	update Z1 5%	update Z1 50%	update Z2 5%	update Z2 50%
predesign	preliminary	uniform	0.94	0.95	0.87	0.92
specific design	Z1Z2-Bayes	lognormal	0.95	1.00	0.94	0.99
	Z1Z2-Freq	-			0.94	1.00

7.5 Comparison with other approaches

7.5.1 NASA SP 8007

Following the procedure recommended by NASA SP 8007 [Wei65b] and described in section 2.4.1. The computed safety factor γ is 0.52 and using *m*=11 and *n*=2 the resulting design load is 42.3 kN. For γ=1, *m*=15 and *n*=2, the resulting buckling load is 81.9 kN as compared to a non-linear FE analysis with perfect structure (without loading or other imperfections) leading to 70.6 kN.

7.5.2 SPLA

Kriegesmann performs the SPLA (see section 2.4.2) in [Sch17] and computes a design load of 63.3 kN with a perturbation load of 30 N. When adding the load imperfections measured during test, the SPLA leads to a design load of 49 kN with the amplitude of the perturbation load being 45 N.

Thus, the result is conservative only in case the load imperfections are considered.

7.5.3 Results

The results for the different design approaches are summarised in Table 7-8 and Table 7-8. For the cylinders investigated, the NASA SP gives a conservative design load level while treating all possible occurring uncertainties with one global knockdown factor (Table 7-7).

The SPLA leads to an unconservative design in case the load imperfections are not considered. In case these imperfections are implemented a less conservative design as

compared to NASA SP is achieved (49 kN as compared to 42.3 kN for NASA SP, refer to Table 7-7).

Table 7-7 Comparison of deterministic methods

Deterministic method	F_D [kN]	β^1
NASA SP 8007	42.3	7.60
SPLA	63.3	not conservative
SPLA including exact knowledge regarding load imperfections	49.0	4.38

The reliability based calibration needs a target reliability level that in this case was chosen at 0.999 (corresponding to a β value of 3.09) and 0.99 (β=2.33) for comparison. Due to the knowledge of the probability density function, this level can be adjusted as needed for other applications. The design load is then computed by multiplying the model inference with the calibrated safety factor for structural uncertainty (according to specified reliability level and the model uncertainty factor, written as:

$$F_D=\gamma_R\gamma_M X_{50\%} \tag{7-8}$$

The probabilistic approach, incorporating calibrated safety factors, leads to a design load of 50.5 kN at the preliminary design stage and 51.5 kN at the specific design stage (refert to Table 7-8). Thus, a higher exploitation of the lightweight potential is already at an early design phase possible. At the specific design phase the model uncertainty is reduced. Thus, the design load becomes less conservative with a corresponding β value of 3.32 with respect to the distribution curve of the test data.

Table 7-8 Comparison of reliability based method

	Reliability level 0.999		Reliability level 0.990	
Probabilistic method	F_D [kN]	β[1]	F_D [kN]	β[1]
Preliminary	50.5	3.93	52.0	3.25
Reliability based Calibration using Bayesian updating (RBCB)	51.5	3.32	52.5	3.06

7.6 Summary and discussion

The reliability based calibration method could be performed due to extensive measurements described in section 5.3 and 5.4. In a pre-study, parameters significantly influencing the buckling load were identified using a Morris Screening (section 7.1, see Figure 7-8).

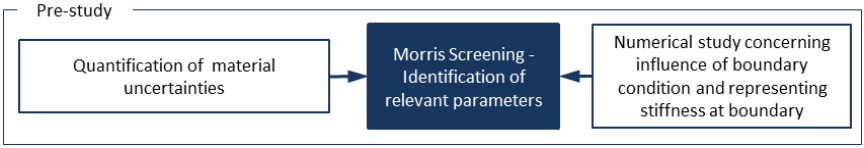

Figure 7-8 Schematic of pre-study

The measurements of these parameters are used for subsequent analyses along with the measurements concerning geometric imperfections. All this data is described through stochastic moments for which prior information exists. Initially, in the absence of any measurements, prior data is created using literature data or engineering judgement. These priors are updated using the available measurements. The updated stochastic moments are input for a Monte Carlo analysis, leading to a probability density function for the loadbearing capacity. A target reliability level is chosen and through the knowledge of the probability density function a structural safety factor to achieve this reliability level is computed.

[1] With respect to test data (Table 7-4)

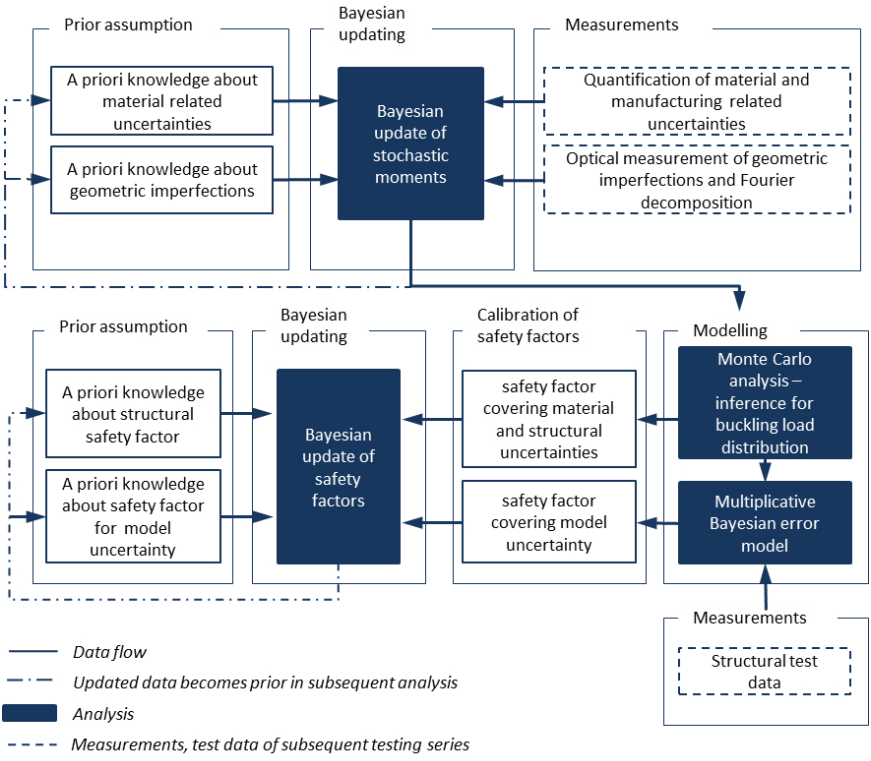

Figure 7-9 Schematic of developed method

The deviation between the inference of the Monte Carlo model and the structural test data leads to a separate safety factor that covers the remaining model uncertainties. It can be caused by uncertainties regarding the test performance or a lack of knowledge about relevant microstructural characteristics like manufacturing flaws described in section 5.5.5. Also, the negligence of the initial stress state can contribute (see section 6.1.6). The a priori assumptions for the safety factors are updated with the computed safety factors.

In case new measurements become available, the procedure is repeated only that the previously derived data concerning material related uncertainties, geometric imperfections and the safety factors become the a priori knowledge for the subsequent analysis (see Figure 7-9).

The approach of the NASA SP 8007 leads to a conservative design load even though no load imperfections, test environment conditions, influence of the stacking sequence or any material or structural uncertainties are specifically considered.

The SPLA shows a less conservative result than the NASA SP when considering the load imperfections and an unconservative result when not considering them separately.

The proposed Bayesian method offers several advantages as compared to deterministic design approaches. Mainly, the conservatism of the design becomes a design variable through the calibration of safety factors, depending on the desired safety level. In contrast, the safety margin inherent to the design load proposed by NASA SP is not known a priori in case of CFRP cylinders. Also, the safety margin associated with the SPLA is not well understood yet. For probabilistic approaches, the knowledge about the safety margin is bought at the expense of great testing and numerical effort while NASA SP and SPLA do only require nominal data for their inference. While SPLA requires the application of a Finite Element code, the NASA SP employs a purely analytical approach that is very fast and makes it easy to compare different designs. As a tool in the pre-design phase it is hence still of great use. In a specific design phase a probabilistic approach allows for exploitation of lightweight potential by directly addressing the required safety level.

Additionally, the usage of a Bayesian framework offers the possibility to incorporate the measured data provided within this thesis as prior information for the uncertainties used to infer buckling loads of new test series with different designs. Thus, the frequentist requirement to use identical designs is avoided. Also, there is no restriction regarding the number of tests to be performed to make an inference.

8 Summary and outlook

8.1 Summary

In addition to the development of a reliability based calibration method for safety factors using Bayesian statistics (RBCB), a contribution to the setup of a databank for uncertainties related to material properties is developed as well as the first statistical meaningful description of Fourier coefficients for unstiffened CFRP cylinders provided.

In order to perform a reliability based design approach, knowledge about uncertainties and sensitivities of the material and structural properties as well as the loading conditions are necessary. The work hence starts off with the determination of uncertainties regarding the material properties on a constituent and laminate level. Although the two Prepreg systems investigated show good quality in terms of fibre volume fraction, the tension tests reveal a stiffness value significantly below the value expected through CLT with high scatter. Measurements of the reference material show high susceptibility towards the preparation of the test specimens. An alternative method is used to determine the bending modulus via dynamic analysis and leads to similar stiffness values but significantly reduced scatter. Hence, this reduced scatter is more representative for the material property.

On the structural level, two sets with 6 CFRP cylinders each are optically measured using the ATOS system to determine geometric imperfections. The quasi-isotropic layup of $[90/+30/-30]_S$ is chosen to represent a layup of realistic applications. Prior to the buckling tests, 11 cylinders are tested on the Hexapod test rig in tension and compression and the ratio of tension stiffness to compression stiffness is found to be between 0.92 and 1.06. During the buckling tests, the axial loads as well as load imperfections are recorded. Thermography is applied to analyse flaws and delaminations before and after the buckling test and all experiments are recorded using a high speed camera. Buckling initiation at a single buckle is observed and delaminations are found after the buckling that does not grow when the structure is repeatedly loaded. The load bearing capacity is however significantly reduced.

Different finite element models with varying degree of detail are employed and their uncertainty with respect to test results are analysed. It is found that the consideration of the load imperfections has by far the highest influence on the deviation between the model and the test result. The consideration of the exact layup, that was found to be different to the specifications made, have only minor influence on the result and so does the consideration of geometric imperfections.

For small R/t ratios it is well known that the susceptibility towards geometric imperfections is reduced. The very low influence found in this investigation is still remarkable. Next to the low R/t ration it is also striking that the cylinders show a very low *rms* value of geometric imperfection compared to others reported in literature. One reason is the constant tension applied to the fibres during the winding process. Additionally, the quasi-isotropic layup leads to comparably high structural integrity compared to other cylinders found in literature.

The relevance of the boundary conditions provided by the test set up is studied separately. A detailed FE model of the potting is performed and the results are compared to other model results. Like the simple model with clamped edge condition, the deviation to the mean of the test result is very small while the inferred scatter is approximately half of the test result of 2.3. Next, six cylinders are optically measured before they were clamped. These measurements are used for a FE model in which the shrinking on the steel rings is considered as additional load steps. The addition of this pre-stress state leads to an increase of standard deviation of the buckling load that matches the test result more closely (2.14).

To develop a reliability based design approach, a sensitivity analysis is performed first to identify relevant parameters to be considered for the Monte Carlo simulations. To consider the stiffness of the clamping condition, a simpler FE-model is set up using a rotational spring stiffness applied to the edge nodes to fit the stiffness of the. A Morris Screening is then performed to analyse the influence of globally changing parameters like thickness, stiffness properties and fibre angle orientation along with the spring stiffness. The load imperfections, stiffness in fibre direction, thickness and fibre angles of the outer 90° layers are identified to be used in later analysis.

The following analysis is divided into three steps: first, simulations are performed representing a preliminary design stage. Here, only nominal values and data from literature are available. At the second stage, data regarding the first set of cylinders set Z1 become available. All data gathered is then updated in a third stage, when set Z2 is measured.

In order to consider geometric imperfections for the second design stage, the Fourier coefficients are assumed to be normally distributed with the first two moments result-

ing from Fourier coefficients of set Z1. These distributions are updated in a Bayesian sense with data of set Z2 for the third design stage. Also, material data is updated but due to the number of independent measurements available here, the results do not differ from the frequentist approach of averaging.

Three Monte Carlo simulations are run representing three design stages. The second update (last design stage) closely matches the test result. From this model, a safety factor in accordance with a target reliability level is calculated. An additional safety factor is computed from the model uncertainty. To retrieve it, a multiplicative error model is employed. Assuming lognormal distributions for the quantities, and applying a Bayesian approach again, a distribution for the error term is calculated and the safety factor determined as the 50 % quantile. Through consideration of load imperfections within this work it is shown for the first time that the FE model is able to represent the buckling behaviour very well, the safety factor regarding model uncertainty is found to be 0.97. Thus, the model can be considered as validated. A high confidence in the model with low scatter is prerequisite for a reliability based design.

Last, the described reliability based Bayesian calibration of the safety factor for the structure and the model uncertainty is compared to other design methods like the NASA SP and Single Perturbation Load Approach. Both these approaches lead to conservative designs (SPLA only if load imperfections are considered) but with unknown reliability level. Both are feasible with very few information. In contrast, a reliability approach relies on the knowledge of the underlying uncertainties of the system under investigation which are commonly not known a priori. However, a Bayesian approach offers a concise framework for a transparent development and calibration of safety factors that can be used as prior information for identical or similar structures. So in case a new structure is developed, the described FE model with measured scatter of material and structural uncertainties can be used with the developed safety factors as prior knowledge. Another advantage of this Bayesian procedure is that for the updating of the parameters involved only very few data, namely the first two moments describing the distribution functions, are necessary. Especially in the case of modelling geometric imperfections this reduces the amount of data dramatically.

8.2 Outlook

The inference made from the updated input parameters using a FE-model with clamped edge condition is in high agreement with the test results in case the load imperfections are considered. In fact, they are making up for the largest portion of uncertainty among the parameters considered. It has to be noted that these load imperfections have to be attributed to the test procedure and cannot be related to forces and moments acting on the structure in service. A design method should not be fitted

to a test that is not representative for the real structural behaviour. It is hence imperative to know the deviations between structural loading conditions in service and those occurring during experiments. A discussion on the scale of shear forces and moments expected acting on the real structure would be helpful to further analyse the reliability level of design approaches that use these structural tests for validation but do not explicitly consider load imperfections.

Although geometric imperfections play only a minor role in the analysis of uncertainties of the present investigation, this finding should be verified using cylinders with higher R/t ratios. Especially it has to be analysed if the low *rms* values found for the cylinders treated in this thesis can be reproduced with larger structures.

Also, different manufacturing methods should be used to compare their influence on geometrical as well as material properties. The more is learned about the transferability of one data set to the other, the stronger is the confidence in the prior probability density functions coming from another set of cylinders.

To be able to solve the Bayesian equations analytically, certain assumptions regarding the type of distribution of the parameters have been made. Future investigations could look at less restricted distribution types and employ Markov chain Monte Carlo Methods to solve the equations.

Appendix

A1 Overview of CFRP cylinder tests

Layup sequence (inside to outside)	No. of specimens	t [mm]	R [mm]	l [mm]	R/t
Bisagni [Bis99]					
fabric(0/+45/-45/+0)	4	1.32	350	540	265
fabric(+45/-45)s	4	1.32	350	540	265
unidir(+45/-45)2s	2	1.2	350	540	292
unidir(90/0)2s	2	1.2	350	540	292
wrapped(90/+30/-30/90)	2	1.5	350	540	233
wrapped(+45/-45)	2	1.5	350	540	233
Bisagni [Bis03]					
fabric(0/+45/-45/+0)	1	1.32	350	540	265
fabric(+45/-45)s	1	1.32	350	540	265
unidir(+45/-45)2s	1	1.2	350	540	292
unidir(90/0)2s	1	1.2	350	540	292
Geier [Gei91] and Meyer-Piening [Mey01]					
(+51/51/+90/90/+40/40)	1	0.75	250	510	333
(+39/39/+0/0/+50/50)	1	0.75	250	510	333
(+49/49/+36/36/+0/0)	1	0.75	250	510	333
(-37/+37/-52/+52/-	2	1.25	250	510	200

68/+68/0/0/60/+60)					
(+60/-60/0/0/+68/-68/+52/-52/+37/-37)	1	1.25	250	510	200
(+38/-38/+68/-68/+90/-90/+8/-8/+53/-53)	2	1.25	250	510	200
(+30/-30/90/90/+22/-22/+38/-38/+53/-53)	4	1.25	250	510	200
(+51/-51/+45/-45/+37/-37/+19/-19/0/0)	1	1.25	250	510	200
(0/0/+19/-19/+37/-37/+45/-45/+51/-51)	3	1.25	250	510	200
Hilburger [Hil06]					
(-45/+45/0/0/0/0/45/-45)	1	1.016	200	355.6	197
(-45/+45/90/90/90/90/45/-45)	1	1.016	200	355.6	197
(-45/+45/0/90/90/0/45/-45)	1	1.016	200	355.6	197
Carri [Car73]					
(±45/05/90/±45/90/05/±45)	2	2.33	46.36	464.3	20
(±45/04//902/04/±45)	2	2.33	46.61	426.7	20
Tennyson [Ten84] (as from [Tak12])					
(0/+45/90/-45/0/+45/90/-45)	1	1.12	83.9	282.7	75
(0/+45/-45/90/90/-45/+45/0)	1	0.99	83.82	287.8	85
(0/0/+45/+45/-45/-45/90/90)	1	1	83.85	284.7	84
(0/+45/-45/-45/+45/0/0/0)	1	0.93	83.79	274.1	90
(0/0/+45/+45/-45/-45/0/0)	1	0.94	83.82	269.2	89
(+45/-45/-45/+45/0/0/0/0)	1	0.93	83.79	282.2	90
(0/90/90/0)	1	0.46	83.57	282.7	182
(90/0/0/90)	1	0.43	83.57	267.7	194
Sun [Sun87] (as from [Tak12])					

(26/-42/76/-3)	1	0.5	83.31	152.4	167
(90/0/0/90)	1	0.49	83.31	152.4	170
(0/90/90/0)	1	0.51	83.31	152.4	163
(-59/5/51/-59)	1	0.5	83.31	152.4	167
(-83/37/15/-86)	1	0.5	83.31	152.4	167
Degenhardt [Deg10]					
(+24/-24/+41/-41)	10	0.46	250.73	500	545
Biagi [Bia08]					
[±45°/0°/90°]2s	1	2	500	1000	250
[±45°/02] 2s	1	2	500	1000	250
[±45°/902] 2s	1	2	500	1000	250
[±45°]4s	1	2	500	1000	250
[±54.7°]4s	1	2	500	1000	250
[0/90]4s	1	2	500	1000	250
Priyadarsini [Pri12]					
[0°/45°/-45°/0°]s	1	1	150	400	150
Schillo [Sch15]					
[0/+30/-30/90]	11	0.78	115	215	147

A2 Randomization process of Morris Screening

Following Morris [Mor91], the sampling space is constructed by first generating a matrix of size *m* x *k* with m equalling *k*+1 and k being the number of parameters under investigation. This matrix *B*, consisting of zeros and ones only, is characterized through the fact that for each column *i*=1,2,3,…,k there exist two rows that differ only in their *i*th entry

$$B = \begin{bmatrix} 0 & 0 & 0 & \dots & 0 \\ 1 & 0 & 0 & \dots & 0 \\ 1 & 1 & 0 & \dots & 0 \\ \dots & \dots & \dots & \dots & \dots \\ 1 & 1 & 1 & 1 & 1 \end{bmatrix}$$

Hence, *m* represents the number of perturbations carried out plus the computational run for the reference configuration (first row, all entries zero).

This matrix is now randomized in the following way:

1. A k-dimensional diagonal matrix *D** is set up with the diagonal elements consisting of either +1 or -1 with equal probability. If $J_{m,k}$ is an *m* x *k* matrix of 1's, then ½[2B-J)D*+J] is a *m* x *k* matrix in which each column is either set equal to corresponding entries in *B* or entries are replaced columnwise by 0's for 1's or vice versa.
2. *x** is a randomly chosen base value of *x* where each element of *x* is randomly assigned a perturbation level from {0, 1/(p-1), 2/(p-1),…,1-Δ} with equal probability.
3. *P** is a *k* x *k* random permutation matrix. Each column contains one element equal to 1 and zeros in all other entries of that column. No two columns have a 1 at the same position.

Now B* with

$$B^* = (J_{m,l} x^* + (\Delta/2)[2B - J_{m,k})D^* + J_{m,k}]P^*$$

is called a random orientation of B. It provides an elementary effect per input that is randomly selected.

Example

The following example is computed using MATLAB.

k	p	Δ	r
5	6	0.6	3

	r=1	r=2	r=3
D*	$\begin{bmatrix} -1 & 0 & 0 & 0 & 0 \\ 0 & -1 & 0 & 0 & 0 \\ 0 & 0 & 1 & 0 & 0 \\ 0 & 0 & 0 & 1 & 0 \\ 0 & 0 & 0 & 0 & 1 \end{bmatrix}$	$\begin{bmatrix} 1 & 0 & 0 & 0 & 0 \\ 0 & 1 & 0 & 0 & 0 \\ 0 & 0 & 1 & 0 & 0 \\ 0 & 0 & 0 & -1 & 0 \\ 0 & 0 & 0 & 0 & 1 \end{bmatrix}$	$\begin{bmatrix} 1 & 0 & 0 & 0 & 0 \\ 0 & 1 & 0 & 0 & 0 \\ 0 & 0 & 1 & 0 & 0 \\ 0 & 0 & 0 & -1 & 0 \\ 0 & 0 & 0 & 0 & 1 \end{bmatrix}$
x*	$[0,0,0.2,0,0.4]$	$[0,0.2,0.4,0.4,0.4]$	$[0,0.2,0.4,0.4,0.4]$
P*	$\begin{bmatrix} 0 & 1 & 0 & 0 & 0 \\ 0 & 0 & 0 & 0 & 1 \\ 0 & 0 & 1 & 0 & 0 \\ 0 & 0 & 0 & 1 & 0 \\ 1 & 0 & 0 & 0 & 0 \end{bmatrix}$	$\begin{bmatrix} 0 & 0 & 1 & 0 & 0 \\ 1 & 0 & 0 & 0 & 0 \\ 0 & 1 & 0 & 0 & 0 \\ 0 & 0 & 0 & 1 & 0 \\ 0 & 0 & 0 & 0 & 1 \end{bmatrix}$	$\begin{bmatrix} 0 & 0 & 1 & 0 & 0 \\ 1 & 0 & 0 & 0 & 0 \\ 0 & 1 & 0 & 0 & 0 \\ 0 & 0 & 0 & 1 & 0 \\ 0 & 0 & 0 & 0 & 1 \end{bmatrix}$
B*	$\begin{bmatrix} 0.4 & 0.6 & 0.2 & 0 & 0.6 \\ 0.4 & 0 & 0.2 & 0 & 0.6 \\ 0.4 & 0 & 0.2 & 0 & 0 \\ 0.4 & 0 & 0.8 & 0 & 0 \\ 0.4 & 0 & 0.8 & 0.6 & 0 \\ 1 & 0 & 0.8 & 0.6 & 0 \end{bmatrix}$	$\begin{bmatrix} 0.2 & 0.4 & 0 & 1 & 0.4 \\ 0.2 & 0.4 & 0.6 & 1 & 0.4 \\ 0.8 & 0.4 & 0.6 & 1 & 0.4 \\ 0.8 & 1 & 0.6 & 1. & 0.4 \\ 0.8 & 1 & 0.6 & 0.4 & 0.4 \\ 0.8 & 1 & 0.6 & 0.4 & 1 \end{bmatrix}$	$\begin{bmatrix} 0.2 & 0.4 & 0 & 1 & 0.4 \\ 0.2 & 0.4 & 0.6 & 1 & 0.4 \\ 0.8 & 0.4 & 0.6 & 1 & 0.4 \\ 0.8 & 0.4 & 0.6 & 1 & 0.4 \\ 0.8 & 1 & 0.6 & 0.4 & 0.4 \\ 0.8 & 1 & 0.6 & 0.4 & 1 \end{bmatrix}$

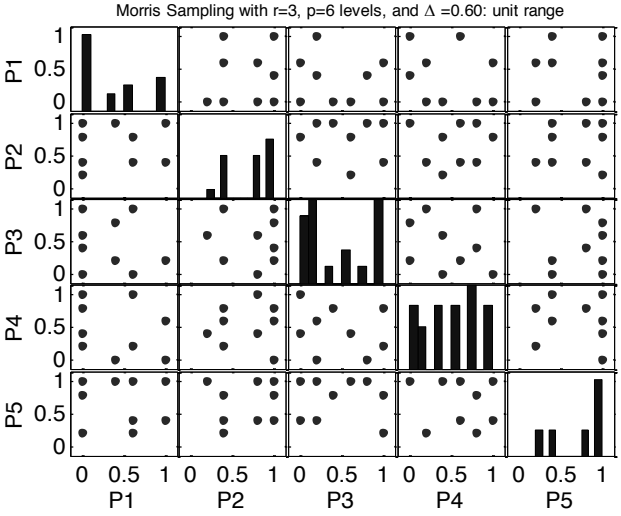

The diagonal of the above figure represents the histogram of appearing perturbation steps that need to be multiplied with the base values of the parameters. The off-diagonal plots show the appearance of parameter combinations. It can be observed that 3 repetitions of this procedure do only partly fill the parameter space. In case a higher coverage is necessary the number of repetitions can be changed. For example, in the below figure the r is changed to 15.

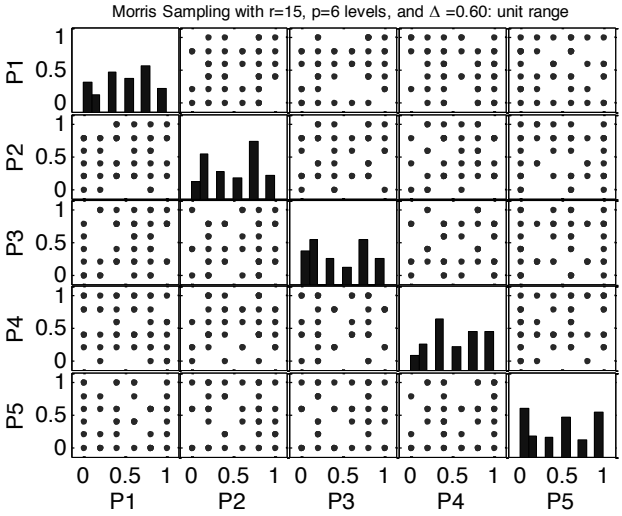

A3 Fibre volume contents

Coupon specimens	Fibre mass proportion [%]	Fibre volume content [%]	Material	Density [g/cm³]
C 30 90 1.3-1	74.40	66.08	AS7	1.79
C 30 90 1.3-2	72.30	63.63	HexPly 8552 Epoxy	1.2
C 30 90 1.3-3	70.90	62.03		
C 30 90 1.3-4	72.50	63.86		
C 30 90 2.3-1	72.80	64.21		
C 30 90 2.3-2	71.80	63.06		
C 30 90 2.3-3	73.70	65.26		
C 30 90 2.3-4	72.30	63.63		
C 30 90 3.3-1	70.40	61.46		
C 30 90 3.3-2	71.20	62.37		
C 30 90 3.3-3	70.30	61.34		
C 30 90 3.3-4	70.70	61.80		
mean	71.94	63.23		
Cov [%]	0.02	2.37		

Cylinder specimens	Fibre mass proportion [%]	Fibre volume content [%]	Material	Density [g/cm³]
C tube 1	66.6	57.2	AS7	1.79
C tube 2	66.3	56.9	HexPly 8552 Epoxy	1.2
C tube 3	66.6	57.2		
C tube 4	66.5	57.1		
mean	66.5	57.1		
Cov [%]	0.21	0.25		

A4 Coupons – Tension tests

Please note: all specimens are numbered consecutively – missing specimens did not break within free length and are hence omitted

Position	Definition	Code	Description
1.	tab material between coupon and aluminium	G/C	GFRP/CFRP
2.	curing temperature during application of tabs	h/c	hot/cold (70 °C /20 °C)
3.	specimen width	n/b	narrow/broad (15 mm/25 mm)
4.	used clamping method	m/s	manual/self-locking
5.	peel-ply	w/o	with/without
6.	strain measurement technique	E/D	Extensometer/strain gauge

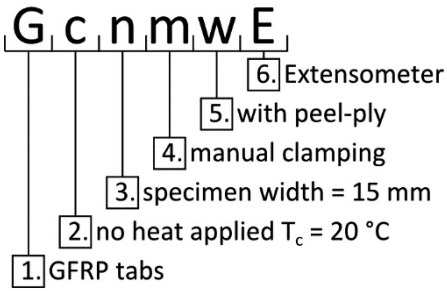

GcnmwE (8)

	b	h	max. ε	max. F	stiffness evaluation range:	
No.	[mm]	[mm]	[%]	[N]	0.05-0.25	0.10-0.30
4	15.04	1.052	1.67	36990	129100	131400
9	15.04	1.035	1.70	34650	128700	130600
10	15.02	1.043	1.64	34100	133400	133700
11	15.01	1.072	1.70	36090	132200	135300
12	15.00	1.052	1.63	33880	127600	127700
13	15.02	1.040	1.53	34230	138300	139300
14	15.03	1.012	1.51	30850	132200	134200
16	15.06	1.021	1.57	33910	135100	138200

GcnswE (6)

	b	h	max. ε	max. F	stiffness evaluation range:	
No.	[mm]	[mm]	[%]	[N]	0.05-0.25	0.1-0.3
8	15.02	1.048	1.88	40220	126700	129900
9	15.06	1.047	1.64	35760	131000	129000
10	15.05	1.016	1.83	39810	131700	132400
11	15.06	1.034	1.83	37760	122600	124600
12	15.08	1.027	1.69	37160	133700	133500
13	15.03	1.049	1.88	43140	136100	136000

GcbswE (7)

	b	h	max. ε	max. F	stiffness evaluation range:	
No.	[mm]	[mm]	[%]	[N]	0.05-0.25	0.1-0.3
1	25.01	1.040	1.94	66710	119100	125100
2	25.04	1.066	1.89	63850	121400	122600
3	25.03	1.042	1.63	61880	129500	132600
4	25.05	1.027	1.77	60720	127200	129100
5	25.02	1.028	1.77	63770	128100	131700
6	25.02	1.021	1.60	58970	133500	133200
7	25.00	1.040	1.85	68290	131500	133400

GhbswE (8)

	b	h	max. ε	max. F	stiffness evaluation range:	
No.	[mm]	[mm]	[%]	[N]	0.05-0.25	0.1-0.3
1	25.07	1.018	1.32	53790	134800	132100
4	25.09	1.056	1.80	60890	120300	119300
5	25.08	1.053	1.95	67260	128400	125200
6	25.08	1.028	1.70	54660	133900	127700
7	25.09	1.016	1.79	61950	135400	136000
8	25.08	1.029	1.75	59630	127200	126000
9	25.07	1.020	1.57	56320	126600	124700
10	25.08	1.040	1.73	63890	126900	123600

GhbswD (8)

	b	h	max. ε	max. F	stiffness evaluation range:	
No.	[mm]	[mm]	[%]	[N]	0.05-0.25	0.1-0.3
1	25.07	1.018	1.32	53790	138900	139800
4	25.09	1.056	1.80	60890	124000	126000
5	25.08	1.053	1.95	67260	127900	129600
6	25.08	1.028	1.70	54660	124300	125400
7	25.09	1.016	1.79	61950	132000	133400
8	25.08	1.029	1.75	59630	129000	130600
9	25.07	1.020	1.57	56320	125600	126800
10	25.08	1.040	1.73	63890	133400	134500

GhbsoE12 (plate 1: GhbsoE1 (10); plate 2: GhbsoE2 (5))

	b	h	max. ε	max. F	stiffness evaluation range:	
No.	[mm]	[mm]	[%]	[N]	0.05-0.25	0.1-0.3
1	24.50	1.040	1.85	68350	131300	131300
2	23.50	1.040	1.73	61000	132500	133700
4	24.75	1.080	1.75	64280	130900	132700
5	23.67	1.080	1.83	67430	141300	143000
6	24.67	1.080	1.70	65260	134400	136000
7	23.63	1.080	1.83	64640	135800	136200
8	24.68	1.080	1.77	67620	132800	132700
9	24.50	1.040	1.85	68350	131300	131300
10	24.53	1.080	1.84	68760	124800	125400
2	24.93	1.040	1.87	66770	128100	134000
3	24.86	1.040	1.90	70080	134200	133500
4	24.87	1.040	1.85	65400	131600	133100
5	24.95	1.040	1.79	67430	141900	140000
6	24.94	1.040	1.72	64340	139600	139600

A5 Analysis of Micrographs

Layer Thickness Measurements (all values in µm)

Z1_1_2							
Position	L1	L2	L3	L4	L5	L6	Resin Layer
0.0	139.8	135.4	127.7	143.6	118.2	117.6	49.6
62.5	139.8	140.4	133.5	134.7	119.5	114.4	62.3
125.0	138.5	139.8	134.7	136.0	117.6	114.4	35.0
187.5	140.4	139.8	133.4	132.8	119.5	112.5	24.8
250.0	151.9	132.2	135.4	132.8	115.0	113.1	22.9
312.5	143.0	140.4	122.6	143.0	120.1	109.9	22.3
375.0	141.7	142.3	124.5	142.3	117.6	109.3	26.1
437.5	146.2	138.5	129.6	136.0	118.2	113.1	11.4
500.0	149.3	133.4	136.6	130.3	120.1	109.9	28.0
562.5	143.0	140.4	127.1	137.9	116.9	112.5	77.5
625.0	146.2	144.2	126.5	133.4	115.0	115.7	69.9
687.5	145.5	142.3	129.6	134.1	115.7	111.8	64.2
750.0	141.7	146.2	109.9	144.9	118.2	113.1	57.2
812.5	144.2	147.4	113.1	146.8	113.7	113.8	52.7
875.0	141.7	150.0	122.0	139.2	115.7	116.3	47.7
937.5	146.2	151.2	120.7	134.7	118.2	117.6	43.9
1000.0	143.6	151.9	114.4	142.3	115.7	119.5	48.3
1062.5	145.5	148.7	115.0	142.3	115.7	119.5	55.9
1125.0	143.6	148.1	111.9	144.9	116.3	121.4	55.3
1187.5	141.1	153.1	123.3	132.2	116.9	120.7	62.9
1250.0	140.4	147.4	141.1	119.5	113.8	122.0	27.3

Z1_1_5							
Position	L1	L2	L3	L4	L5	L6	Resin Layer
-62.5	142.4	123.9	142.3	141.7	123.9	120.7	24.2
0.0	143.0	126.5	139.2	138.5	132.8	146.8	17.2
62.5	131.5	134.7	141.7	137.9	132.8	125.2	21.0
125.0	137.9	126.5	142.3	138.5	129.6	115.0	38.1
187.5	134.7	126.5	143.6	129.6	137.9	113.8	38.8
250.0	136.6	134.7	138.5	143.0	127.7	113.1	33.7
312.5	142.3	122.0	141.1	141.7	131.5	122.0	26.1
375.0	144.2	121.4	136.6	141.7	133.4	126.5	32.4
437.5	144.2	122.6	136.0	139.2	135.3	134.7	16.5
500.0	143.6	123.9	135.3	137.9	136.6	140.4	38.1
562.5	150.6	123.3	136.0	142.3	127.7	123.3	40.0
625.0	143.0	129.6	135.4	142.3	129.0	109.9	38.8
687.5	141.7	129.0	135.4	142.4	130.9	109.3	40.7
750.0	137.9	126.5	137.3	143.6	134.1	104.8	66.7
812.5	129.6	137.3	133.4	144.2	132.2	108.0	75.0
875.0	132.8	143.6	127.7	145.5	135.4	112.5	50.2
937.5	134.1	143.6	127.1	145.5	135.3	129.6	29.2
1000.0	133.5	134.7	135.4	142.4	130.3	149.3	61.6
1062.5	136.6	128.4	139.2	134.7	134.1	132.2	29.9
1125.0	127.7	136.0	144.9	137.3	129.6	118.2	0.0

Z1_1_7							
Position	L1	L2	L3	L4	L5	L6	Resin Layer
-62.5	130.3	133.4	129.6	135.4	128.4	111.2	0.0
0.0	130.3	131.6	132.8	134.7	129.0	115.0	0.0
62.5	123.9	136.0	130.9	134.7	130.9	128.4	42.6
125.0	118.8	137.3	129.0	137.3	132.2	149.3	15.3
187.5	119.5	135.4	130.9	132.2	134.1	151.9	15.3
250.0	129.0	132.2	134.1	133.4	132.8	126.5	0.0
312.5	123.3	136.0	135.3	134.7	130.3	108.0	21.6
375.0	122.6	133.4	139.2	130.3	133.4	104.2	15.9
437.5	120.7	132.8	141.7	130.9	132.2	116.3	10.2
500.0	126.5	133.4	139.8	132.2	131.5	129.6	5.1
562.5	123.9	136.6	142.3	131.5	130.9	147.4	28.6
625.0	116.9	137.9	148.1	125.8	134.1	149.3	21.6
687.5	125.2	127.7	142.3	133.4	131.5	129.0	44.5
750.0	125.2	127.7	146.2	131.5	130.9	106.8	66.7
812.5	133.4	123.3	146.2	132.2	131.5	97.9	63.6
875.0	136.0	125.2	143.0	129.6	132.8	101.0	68.0
937.5	130.9	123.9	143.0	137.3	129.6	109.9	69.9
1000.0	119.5	135.3	144.9	128.4	135.4	135.4	47.0
1062.5	128.4	130.3	141.1	134.7	129.0	143.6	30.5
1125.0	134.1	132.8	137.9	129.0	137.3	125.2	17.2

Z1_2_1							
Position	L1	L2	L3	L4	L5	L6	Resin Layer
-62.5	126.5	148.7	132.2	124.5	125.2	129.6	28.0
0.0	132.2	144.9	133.4	125.8	124.5	130.9	1.3
62.5	129.6	145.5	135.4	125.2	125.8	130.9	6.4
125.0	129.6	145.5	135.4	127.7	126.5	131.5	36.2
187.5	126.5	147.4	134.7	128.4	129.6	134.1	16.5
250.0	127.1	146.2	136.6	125.2	130.3	139.2	26.7
312.5	128.4	143.0	135.4	128.4	126.5	142.3	43.2
375.0	129.6	141.1	136.0	127.1	125.8	144.3	28.6
437.5	127.7	143.0	139.8	123.9	125.8	144.2	20.3
500.0	124.5	145.5	137.9	123.3	130.3	143.0	30.5
562.5	127.1	141.1	141.1	123.9	128.4	146.2	21.0
625.0	131.5	138.5	142.3	120.7	129.6	146.2	15.9
687.5	129.0	134.7	144.9	122.0	130.3	145.5	20.3
750.0	127.7	138.5	143.0	121.4	131.5	146.2	28.0
812.5	124.5	136.6	144.9	119.5	134.7	145.5	42.6
875.0	129.0	132.2	146.2	117.6	134.7	150.0	54.7
937.5	134.7	127.1	151.2	116.3	133.4	150.6	65.5
1000.0	133.4	127.1	148.1	120.7	132.8	151.2	18.4
1062.5	128.4	133.4	150.6	113.7	136.0	150.6	22.9

Z2_1_5							
Position	L1	L2	L3	L4	L5	L6	Resin Layer
-62.5	142.4	123.9	142.3	141.7	123.9	120.7	24.2
0.0	143.0	126.5	139.2	138.5	132.8	146.8	17.2
62.5	131.5	134.7	141.7	137.9	132.8	125.2	21.0
125.0	137.9	126.5	142.3	138.5	129.6	115.0	38.1
187.5	134.7	126.5	143.6	129.6	137.9	113.8	38.8
250.0	136.6	134.7	138.5	143.0	127.7	113.1	33.7
312.5	142.3	122.0	141.1	141.7	131.5	122.0	26.1
375.0	144.2	121.4	136.6	141.7	133.4	126.5	32.4
437.5	144.2	122.6	136.0	139.2	135.3	134.7	16.5
500.0	143.6	123.9	135.3	137.9	136.6	140.4	38.1
562.5	150.6	123.3	136.0	142.3	127.7	123.3	40.0
625.0	143.0	129.6	135.4	142.3	129.0	109.9	38.8
687.5	137.9	126.5	137.3	143.6	134.1	104.8	66.7
750.0	129.6	137.3	133.4	144.2	132.2	108.0	75.0
812.5	132.8	143.6	127.7	145.5	135.4	112.5	50.2
875.0	134.1	143.6	127.1	145.5	135.3	129.6	29.2
937.5	133.5	134.7	135.4	142.4	130.3	149.3	61.6
1000.0	136.6	128.4	139.2	134.7	134.1	132.2	29.9
1062.5	127.7	136.0	144.9	137.3	129.6	118.2	0.0

Z2_4_1							
Position	L1	L2	L3	L4	L5	L6	Resin Layer
-62.5	135.4	121.4	152.5	142.3	118.8	143.6	47.0
0.0	136.0	126.5	148.7	144.2	114.4	145.5	30.5
62.5	137.3	123.3	153.8	141.7	113.7	147.4	11.4
125.0	140.4	118.8	157.0	135.4	115.0	150.0	3.8
187.5	133.4	129.6	152.5	137.3	113.7	149.3	3.2
250.0	135.3	129.0	152.5	137.9	113.1	148.7	10.8
312.5	132.8	129.6	150.0	136.0	113.8	151.9	22.9
375.0	131.5	133.4	148.1	138.5	111.2	151.2	36.9
437.5	130.9	135.4	145.5	136.0	113.1	152.5	50.8
500.0	128.4	136.6	141.7	140.4	110.6	152.5	40.7
562.5	127.7	139.2	136.6	144.3	109.9	151.2	16.5
625.0	130.9	138.5	137.3	139.8	113.8	151.9	10.8
687.5	134.7	139.8	136.0	144.9	108.0	150.0	5.7
750.0	135.4	139.2	141.7	136.6	109.9	154.4	3.8
812.5	132.2	140.4	141.1	137.3	109.3	154.4	21.6
875.0	132.2	139.8	142.3	136.6	109.9	155.0	29.2
937.5	131.5	139.2	142.3	131.5	115.7	153.8	64.8
1000.0	131.5	143.0	142.3	129.0	116.9	155.0	55.3
1062.5	132.8	139.8	143.6	133.4	113.7	155.0	31.1
1125.0	133.4	139.8	143.6	127.1	130.3	145.5	11.4
1187.5	134.7	139.8	143.0	125.8	123.9	151.2	1.3

Z2_4_3							
Position	L1	L2	L3	L4	L5	L6	Resin Layer
-62.5	116.3	153.1	144.9	132.2	156.3	110.6	13.3
0.0	116.3	154.4	141.1	132.8	158.2	109.3	13.3
62.5	117.6	151.2	141.1	133.4	150.6	115.0	18.4
125.0	115.0	148.7	141.7	132.8	148.1	121.4	14.0
187.5	119.5	148.1	139.2	123.3	165.9	115.7	32.4
250.0	118.8	148.7	141.1	137.3	133.4	132.8	71.8
312.5	117.6	147.4	144.3	132.2	145.5	127.7	35.0
375.0	117.6	149.3	141.7	135.4	146.2	121.4	16.5
437.5	118.2	149.3	141.1	137.3	142.3	126.5	10.2
500.0	119.5	146.2	142.3	130.3	152.5	123.3	10.2
562.5	118.2	146.8	143.6	141.1	139.8	126.5	12.1
625.0	127.7	136.6	142.3	137.9	136.6	133.4	15.3
687.5	129.0	134.1	144.9	133.4	154.4	120.1	23.5
750.0	120.1	143.6	142.3	130.3	166.5	112.5	35.6
812.5	122.0	144.2	139.8	130.9	168.4	109.9	49.6
875.0	127.1	139.2	137.9	131.5	171.6	104.2	68.6
937.5	127.1	139.8	135.4	131.6	177.3	100.4	50.2
1000.0	125.2	143.6	134.1	130.3	160.1	116.3	29.9
1062.5	125.2	141.7	137.3	127.7	171.6	106.1	28.0
1125.0	126.5	139.8	133.5	128.4	166.5	115.7	13.3

Z2_4_7							
Position	L1	L2	L3	L4	L5	L6	Resin Layer
-62.5	120.1	161.4	127.1	130.9	142.3	123.9	19.1
0.0	121.4	157.0	130.9	127.1	146.8	122.6	15.3
62.5	122.0	154.4	127.2	133.4	145.5	123.9	18.4
125.0	123.9	153.1	129.1	144.3	134.1	123.3	25.4
187.5	127.1	151.9	132.2	132.8	139.2	123.3	41.3
250.0	127.7	146.2	133.4	133.4	141.1	120.1	57.8
312.5	127.7	146.2	140.4	127.7	142.3	119.5	82.6
375.0	125.8	143.0	153.8	118.2	146.2	116.3	42.6
437.5	122.6	141.7	160.8	111.2	149.3	114.4	17.2
500.0	123.3	142.4	158.3	116.3	147.4	113.1	31.1
562.5	128.4	136.6	153.8	118.8	155.0	108.7	1.9
625.0	127.1	138.5	141.7	133.4	150.6	109.9	20.3
687.5	126.5	136.6	170.3	109.3	149.3	111.2	8.3
750.0	125.2	137.3	158.3	122.7	151.2	110.6	29.3
812.5	127.1	136.6	155.7	123.3	150.0	114.4	82.0
875.0	123.9	134.7	149.3	132.8	147.4	116.9	70.5
937.5	123.3	132.2	139.2	146.2	150.0	117.6	59.7
1000.0	120.1	134.7	141.1	141.1	148.7	123.9	40.7
1062.5	126.5	128.4	144.9	143.0	146.2	120.7	32.4
1125.0	122.6	128.4	141.2	151.2	143.0	122.0	26.7
1187.5	122.6	124.5	146.8	150.6	139.2	123.3	33.1

Fibre volume content [%]

2a						
Position	L1	L2	L3	L4	L5	L6
0		68.4	71.3	69.1	68.0	
125		69.8	70.0	68.7	68.8	
250		66.6	68.9	65.3	59.5	
375		65.8	65.1	69.8	62.3	
500		68.6	67.6	64.6	64.8	
625		71.0	67.0	69.2	61.6	
750		67.7	68.4	62.9	60.9	
875		68.3	65.3	66.4	67.7	
1000		70.7	69.0	66.1	65.8	
1125		72.3	69.3	71.2	66.8	

2b						
Position	L1	L2	L3	L4	L5	L6
0		67.9	60.9	65.4	67.1	
125		59.2	64.7	67.5	66.4	
250		59.5	60.0	66.2	66.1	
375		64.1	65.2	69.9	66.7	
500		66.6	62.9	67.2	63.5	
625		65.7	68.6	66.2	62.3	
750		62.0	58.2	68.4	66.8	
875		61.2	63.6	73.7	71.4	
1000		59.9	61.0	69.5	75.1	
1125		61.5	67.0	67.1	69.3	

6_a						
Position	L1	L2	L3	L4	L5	L6
0		71.4	65.7	71.6	65.4	
125		72.7	70.4	73.2	65.3	
250		69.4	64.2	73.4	65.7	
375		74.0	67.0	77.0	66.7	
500		75.8	70.1	74.2	63.3	
625		76.4	72.3	74.5	68.7	
750		67.1	62.2	73.5	71.4	
875		67.9	61.5	71.5	71.6	
1000		71.4	64.5	69.6	69.4	
1125		65.4	66.7	70.8	70.7	

RZ1_1						
Position	L1	L2	L3	L4	L5	L6
0	64.9	64.2	62.9	63.0	66.5	55.2
125	65.1	64.4	62.7	56.1	72.3	60.0
250	63.4	67.5	62.9	63.1	72.2	54.1
375	58.4	67.9	63.9	63.9	70.9	54.3
500	60.4	69.6	64.2	68.5	72.0	57.3
625	61.6	66.4	65.8	66.5	73.0	52.7
750	62.0	66.0	65.7	63.0	72.2	57.2
875	62.3	68.6	65.6	67.1	71.0	62.7
1000	59.2	66.8	62.4	64.2	72.2	61.5
1125	54.8	69.9	59.2	58.7	67.3	60.1

RZ1_2						
Position	L1	L2	L3	L4	L5	L6
0		58.2	54.9	60.9	63.6	
125		58.1	63.5	55.6	58.9	
250		62.6	58.6	60.7	58.4	
375		55.4	60.8	61.0	53.6	
500		58.4	61.0	52.7	59.2	
625		60.3	64.0	61.5	61.7	
750		62.3	58.8	63.6	64.3	
875		57.1	58.2	59.3	50.5	
1000		56.9	62.3	58.1	58.1	
1125		57.1	60.4	63.2	60.9	

RZ1_3						
Position	L1	L2	L3	L4	L5	L6
0		57.8	54.0	58.9	62.6	
125		61.4	60.0	64.7	63.1	
250		64.2	62.7	64.0	63.2	
375		63.2	58.8	61.7	69.2	
500		62.7	63.6	64.0	63.9	
625		59.2	53.2	60.8	58.2	
750		56.2	51.9	54.3	60.1	
875		55.0	61.6	60.4	66.4	
1000		55.9	58.5	56.9	66.0	
1125		52.6	61.2	55.6	61.7	

RZ1_4						
Position	L1	L2	L3	L4	L5	L6
0	59.7	57.7	63.8	63.7	70.1	59.8
125	60.8	58.5	65.2	58.4	65.7	53.1
250	63.7	64.4	64.4	60.5	68.2	54.9
375	59.9	63.7	68.5	62.7	69.9	53.5
500	62.8	64.6	64.1	61.9	69.7	59.2
625	62.7	57.3	66.7	62.6	67.5	56.8
750	62.4	61.2	65.2	67.1	66.1	63.0
875	63.7	60.3	66.5	61.9	61.3	62.0
1000	65.5	57.7	66.1	64.2	58.8	63.5
1125	62.1	56.8	62.7	65.9	59.4	55.9

Z1_1_1						
Position	L1	L2	L3	L4	L5	L6
0		62.2	62.1	59.1	59.4	
125		60.6	63.2	62.6	59.9	
250		61.3	64.3	57.7	59	
375		62.5	63.3	58.6	58.4	
500		55.2	60.4	54.6	60.2	
625		63.7	54.5	59.6	58.5	
750		61.4	57.1	62.2	63.3	
875		61.4	62.8	56.7	50.7	
1000		58.5	64.9	56.4	55.9	
1125		59.3	64.2	58.5	58.7	

Z1_1_2						
Position	L1	L2	L3	L4	L5	L6
0		56.1	53.7	64.5	62.4	
125		61.8	60.7	56.4	62.9	
250		62.3	31.2	62.0	61.5	
375		59.9	59.6	61.4	62.9	
500		59.8	61.6	59.4	61.3	
625		61.4	59.1	62.1	66.0	
750		61.5	57.8	60.7	55.0	
875		62.9	63.5	65.0	63.4	
1000		63.9	60.6	65.3	66.9	
1125		63.3	62.2	55.7	62.6	

Z1_1_5						
Position	L1	L2	L3	L4	L5	L6
0	64.4	57.4	59.4	65.2	62.0	60.4
125	60.3	70.5	59.3	66.8	61.4	56.4
250	60.6	59.3	56.0	63.1	61.1	57.1
375	59.0	67.4	53.8	68.0	61.2	60.0
500	60.8	62.5	55.4	70.0	66.7	61.6
625	61.9	65.9	52.0	68.2	68.0	63.3
750	59.2	60.9	51.8	66.6	63.4	60.1
875	60.7	63.0	51.4	68.1	64.8	59.8
1000	60.4	65.0	51.1	69.1	62.7	62.7
1125	61.6	54.9	59.4	71.4	65.5	67.0

Z1_1_7						
Position	L1	L2	L3	L4	L5	L6
0	63.5	66.1	66.4	51.4	65.3	66.6
125	59.0	65.4	63.2	50.7	62.1	66.1
250	61.1	63.1	63.0	54.4	60.6	64.1
375	63.4	66.6	62.9	55.7	65.4	64.0
500	62.8	63.0	63.5	60.7	61.4	68.5
625	56.9	63.9	65.0	59.8	61.8	69.6
750	58.8	66.6	66.4	57.4	58.9	67.2
875	64.5	68.0	64.8	62.1	62.8	63.8
1000	61.8	62.9	63.2	60.5	60.6	66.9
1125	57.2	64.6	64.5	61.3	55.4	64.5

Z1_2_1						
Position	L1	L2	L3	L4	L5	L6
0		58.5	55.8	63.0	57.2	
125		61.7	63.1	61.8	65.1	
250		58.9	61.1	62.8	64.5	
375		59.3	55.8	67.6	62.6	
500		59.4	58.4	64.6	62.7	
625		59.8	62.1	65.7	63.4	
750		59.1	52.2	59.4	60.9	
875		59.8	56.4	61.5	60.1	
1000		55.9	61.5	59.3	62.8	
1125		55.4	58.9	58.3	59.7	

Z2_1_5						
Position	L1	L2	L3	L4	L5	L6
0		52.5	58.3	63.9	59.2	
125		55.1	63.6	62.5	54.7	
250		57.7	63.3	63.8	62.4	
375		57.7	61.2	62.0	64.7	
500		60.2	57.5	61.6	57.9	
625		57.0	62.1	60.7	59.6	
750		56.2	61.0	62.5	62.9	
875		58.5	61.2	60.4	62.6	
1000		56.2	58.3	57.1	57.8	
1125		54.9	58.8	59.8	55.7	

Z2_4_1						
Position	L1	L2	L3	L4	L5	L6
0		53.1	61.7	64.7	63.3	
125		56.5	63.9	62.6	58.7	
250		61.9	63.7	60.3	56.9	
375		59.2	59.2	59.5	57.7	
500		59.4	56.1	61.2	60.1	
625		59.4	54.3	60.4	58.1	
750		59.7	57.2	61.2	56.2	
875		59.7	58.4	60.1	53.0	
1000		60.2	59.2	57.8	58.1	
1125		59.9	59.8	59.0	48.5	

Z2_4_3						
Position	L1	L2	L3	L4	L5	L6
0		58.3	51.1	55.4	50.2	
125		57.9	52.4	59.4	57.0	
250		59.5	51.5	60.1	50.7	
375		59.2	56.8	57.9	64.2	
500		60.0	56.8	61.7	58.2	
625		58.3	60.2	65.8	53.7	
750		58.1	57.3	65.9	52.6	
875		62.9	51.5	61.7	54.4	
1000		60.8	52.9	50.5	52.4	
1125		61.2	50.1	55.6	56.7	

Z2_4_7						
Position	L1	L2	L3	L4	L5	L6
0		61.6	58.8	64.3	50.1	
125		66.0	61.9	59.2	61.3	
250		64.3	63.8	64.2	60.8	
375		64.4	64.5	67.0	61.5	
500		59.6	63.3	62.3	63.4	
625		59.6	69.7	63.4	66.4	
750		65.9	66.0	63.8	65.3	
875		68.5	65.7	62.6	65.3	
1000		64.9	67.9	60.2	63.2	
1125		67.8	68.9	61.4	62.7	

A6 Histograms of imperfections for individual cylinders

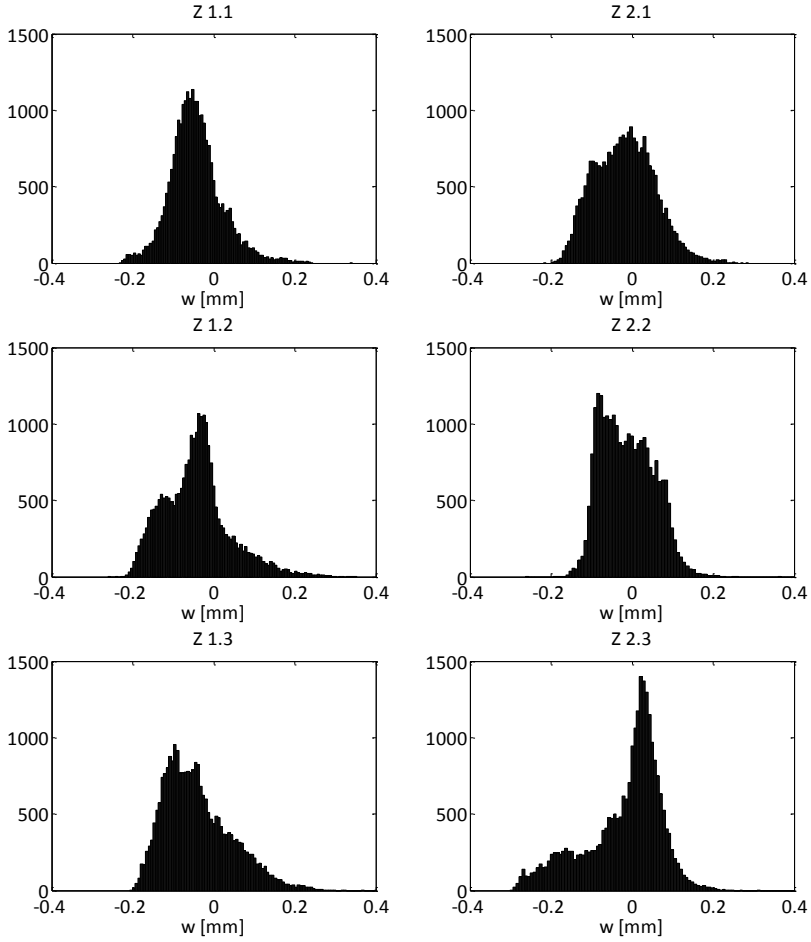

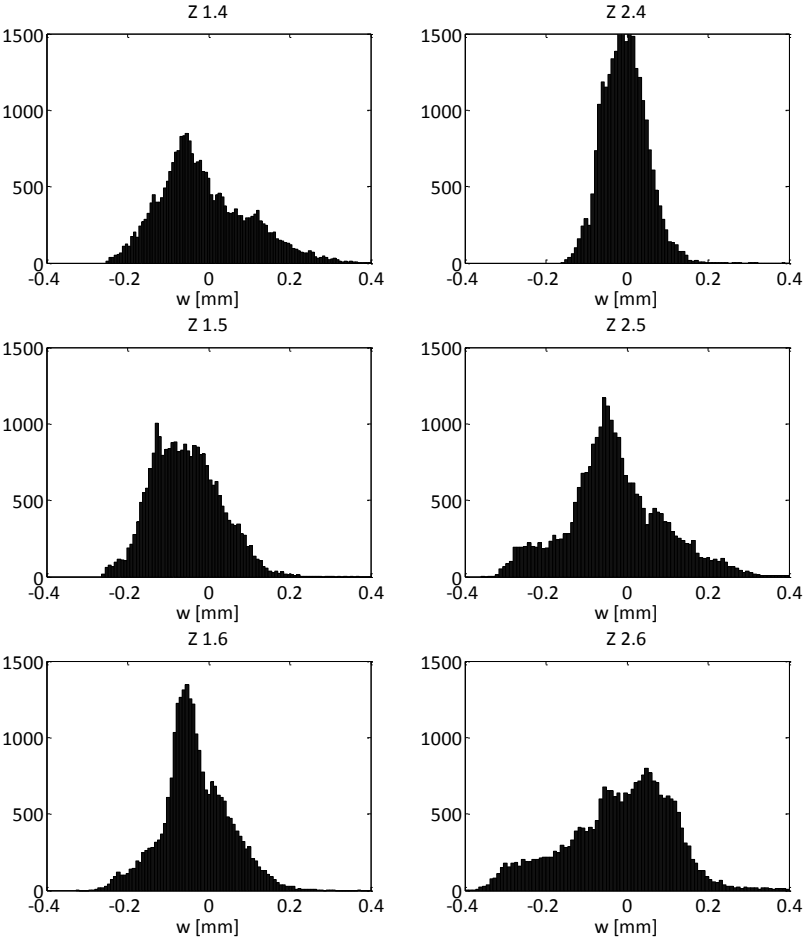
Z 1.4
Z 2.4
Z 1.5
Z 2.5
Z 1.6
Z 2.6
1500
1000
500
0
-0.4
-0.2
0
0.2
0.4
w [mm]

A7 Fourier coefficients of CFRP cylinders

The following tables give the Fourier coefficients of the tested cylinders with their amplitude and phase shift representation. Ten coefficients for the axial representation are given from left to right and 15 coefficients for the circumferential representation from top to bottom, respectively.

Z 1.1

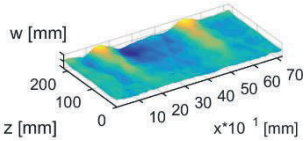

χ *10^{-2}

3.248	0.215	0.595	0.785	1.112	0.825	0.091	1.183	0.734	0.023
3.355	3.928	0.078	0.248	0.158	0.099	0.173	0.129	0.161	0.133
5.528	4.875	0.291	0.360	0.110	0.106	0.085	0.078	0.187	0.140
1.142	1.351	1.078	0.025	0.040	0.056	0.145	0.033	0.054	0.041
4.155	4.313	1.637	0.404	0.342	0.035	0.188	0.109	0.042	0.039
1.077	0.725	0.508	0.070	0.066	0.054	0.062	0.134	0.046	0.052
1.414	1.695	0.918	0.519	0.142	0.177	0.086	0.060	0.039	0.048
0.294	0.130	0.506	0.141	0.161	0.113	0.043	0.304	0.172	0.072
0.123	0.408	1.213	0.498	0.248	0.068	0.166	0.261	0.118	0.242
0.142	0.249	0.680	0.411	0.468	0.263	0.208	0.060	0.110	0.129
0.035	0.119	0.107	0.392	0.128	0.165	0.073	0.033	0.109	0.065
0.073	0.109	0.104	0.029	0.295	0.148	0.042	0.071	0.039	0.041
0.081	0.291	0.074	0.465	0.316	0.342	0.175	0.093	0.102	0.039
0.040	0.037	0.135	0.051	0.234	0.196	0.103	0.073	0.040	0.085
0.043	0.096	0.140	0.065	0.031	0.338	0.200	0.069	0.118	0.057

ϕ *10^{-0}

3.142	0.000	0.000	3.142	0.000	3.142	0.000	3.142	0.000	3.142
-0.479	2.522	0.937	2.218	-0.754	2.792	0.262	1.750	1.064	0.423
2.654	-0.730	1.667	-0.505	-1.412	-0.667	-0.839	1.796	-1.047	-0.222
0.446	0.216	3.796	0.112	4.135	4.496	1.297	-0.791	1.902	2.065
-0.302	2.653	-1.310	3.028	-0.688	3.135	-1.555	1.611	-0.706	0.314
1.602	3.628	-0.755	-0.107	-0.252	0.079	0.529	0.625	-1.366	0.975
2.193	-1.430	0.502	-0.398	1.796	-0.224	2.175	-0.780	3.746	0.309
2.156	3.877	1.320	4.683	4.647	0.932	4.131	2.808	4.603	4.588
-0.174	-0.435	2.225	2.433	-1.423	0.942	0.474	-0.521	3.689	-1.478
2.770	0.578	3.234	2.478	-0.410	0.115	-0.657	0.136	0.250	-0.665
0.088	2.333	4.454	1.949	0.120	0.592	3.894	0.848	-0.071	2.499
0.040	1.561	0.967	3.937	1.813	1.665	2.468	-0.631	3.201	-0.197
1.202	-0.358	0.925	0.009	2.547	3.092	0.927	3.756	0.737	3.088
0.612	2.636	0.896	-0.408	0.603	2.373	2.906	-0.387	2.356	0.381
-0.134	1.874	-0.747	1.366	-0.249	-0.811	1.310	3.961	1.186	4.408

Z 1.2

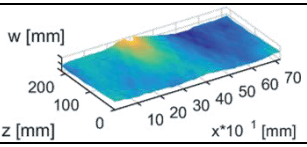

χ *10^{-2}

2.185	1.070	1.006	0.059	0.389	0.202	0.080	0.279	0.209	0.281
9.994	8.634	0.447	0.738	0.444	0.223	0.217	0.465	0.042	0.198
4.687	3.310	0.285	0.403	0.294	0.395	0.144	0.347	0.176	0.082
1.921	2.963	0.231	0.447	0.167	0.146	0.152	0.175	0.068	0.146
1.077	2.220	0.218	0.077	0.086	0.066	0.185	0.052	0.023	0.060
0.624	0.621	0.550	0.143	0.177	0.134	0.016	0.092	0.111	0.134
0.329	0.467	0.340	0.214	0.176	0.107	0.102	0.040	0.022	0.100
0.205	0.251	0.293	0.111	0.178	0.150	0.138	0.173	0.027	0.204
0.048	0.241	0.332	0.419	0.168	0.087	0.192	0.065	0.040	0.040
0.114	0.325	0.339	0.226	0.270	0.223	0.147	0.083	0.117	0.011
0.056	0.133	0.065	0.418	0.023	0.017	0.129	0.077	0.031	0.042
0.094	0.117	0.038	0.220	0.262	0.141	0.095	0.085	0.036	0.042
0.097	0.184	0.179	0.323	0.228	0.298	0.061	0.085	0.112	0.043
0.077	0.060	0.100	0.245	0.321	0.047	0.061	0.024	0.100	0.080
0.097	0.060	0.186	0.067	0.097	0.209	0.055	0.019	0.112	0.106

ϕ *10^{-0}

3.142	3.142	0.000	0.000	0.000	3.142	0.000	3.142	0.000	3.142
2.152	-0.920	0.882	-0.840	1.307	-0.892	0.175	3.931	-0.298	2.343
-0.077	1.760	4.032	1.750	-1.109	2.347	4.403	1.781	-0.859	3.796
1.500	-1.112	-1.297	4.248	4.578	-1.306	-0.409	3.720	3.982	-0.032
2.725	-0.087	-0.080	2.886	0.311	0.692	1.165	0.480	0.496	2.898
0.745	4.216	-0.552	1.771	0.030	1.650	-0.246	1.645	0.290	3.596
1.566	4.476	3.412	-0.677	0.637	-1.564	0.211	1.275	1.023	4.603
3.484	1.897	1.020	0.831	-1.309	-0.031	-0.350	4.599	1.864	3.281
2.457	0.076	2.890	3.209	2.129	1.748	1.496	4.236	1.778	0.355
4.305	0.426	-0.101	-0.975	3.399	4.685	3.269	1.573	4.417	4.081
3.178	2.505	-1.533	3.923	1.158	1.893	1.382	-0.183	-0.228	2.276
-0.137	-0.044	-0.554	1.121	3.667	-0.964	1.619	2.718	2.791	3.692
3.270	2.905	3.975	2.293	-0.373	-0.214	-0.225	-0.594	1.626	-0.677
2.187	0.953	1.310	-0.899	2.752	2.436	2.386	4.264	-0.248	1.381
1.057	-0.297	3.512	4.686	2.598	1.959	-1.305	4.709	2.425	3.669

Z 1.3

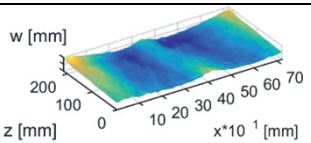

χ *10^{-2}

4.652	0.654	1.207	0.084	0.905	0.469	0.876	0.359	0.474	0.148
7.751	6.702	0.336	0.795	0.117	0.472	0.144	0.176	0.068	0.270
8.871	3.507	0.401	0.361	0.084	0.155	0.137	0.048	0.085	0.070
0.849	2.451	0.213	0.308	0.168	0.110	0.060	0.124	0.035	0.056
1.653	2.201	0.766	0.090	0.017	0.058	0.105	0.152	0.119	0.155
0.637	1.123	0.325	0.157	0.128	0.221	0.095	0.035	0.180	0.110
0.289	0.850	0.510	0.460	0.106	0.065	0.143	0.049	0.112	0.155
0.266	0.477	0.234	0.159	0.160	0.210	0.414	0.219	0.164	0.069
0.044	0.330	0.441	0.139	0.272	0.095	0.133	0.073	0.026	0.137
0.091	0.088	0.359	0.309	0.268	0.105	0.096	0.116	0.100	0.164
0.055	0.137	0.086	0.150	0.216	0.106	0.121	0.058	0.078	0.073
0.090	0.283	0.146	0.328	0.309	0.208	0.093	0.095	0.039	0.031
0.135	0.189	0.148	0.207	0.496	0.135	0.074	0.039	0.084	0.073
0.050	0.099	0.038	0.050	0.060	0.127	0.050	0.147	0.039	0.026
0.078	0.150	0.061	0.017	0.086	0.062	0.152	0.073	0.067	0.079

ϕ *10^{-0}

3.142	0.000	0.000	3.142	0.000	3.142	0.000	3.142	0.000	3.142
0.239	3.402	2.485	3.674	0.027	3.962	3.341	3.303	2.597	2.987
0.413	2.319	2.807	2.560	3.628	2.618	1.907	0.042	2.108	-0.026
2.336	-1.077	-1.144	4.441	4.400	-0.431	4.225	3.506	4.629	1.404
0.807	2.380	-0.742	2.933	1.805	3.761	2.874	-0.910	3.513	-1.152
1.984	-1.212	0.330	-1.153	-0.141	-0.442	1.526	3.930	0.723	0.606
-0.840	2.391	2.579	3.125	2.868	-0.185	1.951	2.760	-0.956	-0.662
1.145	-0.877	3.471	4.290	1.464	3.312	1.771	2.458	0.408	3.862
1.940	2.590	1.345	2.998	4.136	2.185	4.182	-1.420	3.243	3.978
3.391	0.814	2.857	-1.388	0.793	-1.289	1.178	4.619	4.340	1.400
-0.941	-0.550	-0.188	-1.442	3.705	1.003	-1.067	0.783	-1.440	-1.108
2.076	0.241	2.557	0.873	0.085	4.045	1.251	3.564	-0.092	2.310
3.354	-0.931	1.879	-0.856	1.359	2.593	1.164	4.050	0.020	-1.011
3.257	0.596	1.705	-0.731	2.692	3.896	0.379	2.529	-1.256	2.036
2.048	-1.206	0.670	1.757	3.621	-1.483	2.785	2.358	-0.491	3.609

Z 1.4

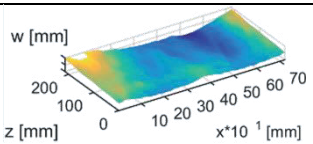

χ *10^{-2}

3.257	0.354	0.972	0.770	1.099	0.823	0.809	0.189	0.107	0.529
14.273	11.441	0.338	1.192	0.308	0.797	0.286	0.341	0.206	0.080
8.898	1.611	0.237	0.205	0.114	0.213	0.055	0.367	0.086	0.013
1.133	0.998	0.503	0.118	0.175	0.253	0.184	0.216	0.262	0.090
0.545	0.932	1.223	0.227	0.270	0.063	0.258	0.105	0.168	0.204
0.838	0.451	0.512	0.129	0.174	0.281	0.147	0.158	0.100	0.113
0.322	1.391	0.665	0.508	0.174	0.153	0.096	0.087	0.222	0.069
0.346	0.210	0.498	0.161	0.256	0.072	0.266	0.170	0.219	0.184
0.218	0.145	0.420	0.243	0.613	0.134	0.289	0.103	0.064	0.037
0.275	0.165	0.220	0.217	0.129	0.106	0.057	0.016	0.208	0.238
0.160	0.095	0.144	0.353	0.378	0.183	0.068	0.168	0.140	0.090
0.069	0.165	0.057	0.584	0.170	0.225	0.114	0.007	0.021	0.103
0.104	0.135	0.043	0.230	0.399	0.109	0.195	0.049	0.054	0.076
0.084	0.091	0.136	0.035	0.235	0.115	0.160	0.074	0.051	0.096
0.034	0.062	0.041	0.172	0.052	0.162	0.077	0.108	0.124	0.053

ϕ *10^{-0}

3.142	0.000	0.000	3.142	3.142	3.142	3.142	3.142	0.000	0.000
0.766	3.876	-0.125	3.907	-1.509	4.183	-1.145	4.473	2.377	3.648
0.699	4.580	-0.868	-1.297	-0.722	-1.233	-0.652	-0.537	3.527	0.698
0.378	2.873	3.792	2.991	0.845	0.192	1.724	-0.062	3.800	3.875
-0.757	0.756	1.614	-0.412	1.669	-0.944	2.348	-1.001	3.283	0.005
2.244	3.741	-0.553	-1.038	2.917	3.770	1.767	4.535	0.610	-0.879
-0.707	1.422	1.424	4.425	0.326	4.600	-0.635	4.646	0.937	-0.124
3.408	-1.168	3.221	2.139	0.617	-0.978	0.748	3.982	2.221	2.288
3.774	1.166	2.800	-1.331	1.066	-0.594	0.727	3.868	0.611	3.462
3.498	0.868	1.821	0.742	3.052	1.444	-1.152	0.988	-1.084	-1.478
3.962	-1.189	4.361	4.324	2.026	2.274	-0.247	2.115	0.200	0.431
2.620	4.122	0.631	3.633	1.325	0.351	-0.182	1.195	2.201	-0.409
3.268	-0.598	1.625	-1.005	0.923	0.905	4.551	1.415	1.696	2.787
4.343	-0.852	1.430	-1.470	0.978	-0.914	4.495	1.845	-0.925	4.415
-0.736	-0.657	1.354	-1.226	0.756	0.524	-0.432	1.757	-1.109	-0.426

Z 1.5

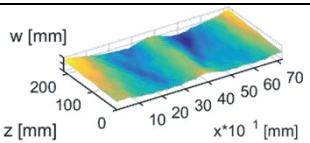

χ *10^{-2}

3.611	0.883	0.301	0.253	0.563	0.052	0.320	0.031	0.114	0.339
6.824	5.275	0.477	0.564	0.485	0.195	0.261	0.356	0.205	0.341
10.226	2.811	0.580	0.209	0.056	0.181	0.116	0.038	0.161	0.180
2.088	1.010	0.830	0.139	0.232	0.123	0.114	0.162	0.113	0.136
2.337	1.186	1.162	0.574	0.304	0.130	0.180	0.171	0.009	0.091
0.812	0.726	0.489	0.436	0.222	0.126	0.096	0.186	0.227	0.047
0.867	0.741	1.087	0.036	0.336	0.044	0.165	0.045	0.079	0.081
0.116	0.645	0.341	0.484	0.097	0.112	0.087	0.116	0.067	0.067
0.158	0.574	0.571	0.572	0.273	0.053	0.111	0.172	0.067	0.179
0.176	0.164	0.512	0.195	0.304	0.071	0.124	0.159	0.122	0.042
0.069	0.141	0.148	0.118	0.117	0.083	0.074	0.084	0.151	0.107
0.091	0.214	0.188	0.287	0.427	0.122	0.122	0.169	0.145	0.056
0.035	0.049	0.072	0.083	0.643	0.149	0.084	0.022	0.030	0.054
0.101	0.104	0.068	0.082	0.202	0.025	0.145	0.042	0.078	0.063
0.015	0.055	0.101	0.042	0.120	0.063	0.050	0.057	0.083	0.020

ϕ *10^{-0}

3.142	0.000	0.000	0.000	0.000	0.000	0.000	3.142	0.000	0.000
0.332	3.562	2.852	3.293	3.591	1.965	-1.364	2.240	4.065	2.853
0.273	2.974	1.867	3.056	3.954	4.080	0.640	1.196	4.120	3.163
3.000	0.198	-1.065	-0.121	4.306	2.086	3.276	1.011	0.331	-0.204
0.390	4.573	1.376	2.294	1.214	1.226	1.062	1.807	1.804	2.641
-1.388	1.730	2.298	-1.208	-1.142	-1.279	4.625	-1.052	-0.287	3.356
1.886	2.568	-1.373	0.486	1.566	-1.442	1.155	3.816	0.337	-0.495
-1.202	4.691	2.054	1.562	-0.822	2.313	-0.333	4.049	-1.353	4.274
3.521	1.522	1.074	4.378	3.732	-0.454	3.514	2.369	-1.141	1.783
4.635	0.181	4.710	3.620	0.748	3.168	0.911	4.429	1.411	3.909
3.479	2.292	3.265	1.267	-1.016	3.139	2.746	-1.014	2.901	4.371
0.862	-1.406	1.749	4.581	3.988	1.921	4.372	1.487	-1.150	-0.170
-1.290	0.305	2.910	1.396	0.991	1.335	3.265	3.712	1.599	3.261
0.588	1.980	2.198	0.302	-0.001	-1.329	3.860	2.570	3.578	0.909
-1.207	4.698	0.850	2.062	-1.246	0.404	1.087	2.673	-0.647	-0.316

Z 1.6

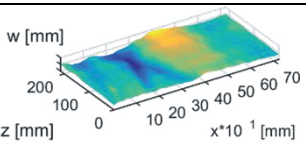

χ *10^{-2}

3.188	0.093	0.376	0.728	0.619	0.015	0.679	0.079	0.851	0.062
8.684	5.669	0.594	0.732	0.263	0.547	0.384	0.236	0.331	0.190
7.039	3.858	0.526	0.322	0.378	0.295	0.200	0.172	0.121	0.300
2.428	1.384	0.889	0.103	0.224	0.192	0.182	0.068	0.200	0.113
2.137	3.177	1.650	0.533	0.132	0.170	0.129	0.067	0.031	0.057
0.852	1.723	1.006	0.618	0.288	0.223	0.140	0.099	0.104	0.047
0.768	0.675	0.648	1.226	0.129	0.396	0.242	0.193	0.153	0.249
0.134	1.030	0.618	0.895	0.192	0.095	0.114	0.122	0.114	0.127
0.253	0.835	0.774	1.227	0.078	0.062	0.103	0.131	0.165	0.046
0.095	0.197	0.308	0.719	0.437	0.248	0.150	0.153	0.045	0.109
0.085	0.241	0.205	0.214	0.368	0.130	0.151	0.173	0.093	0.152
0.065	0.204	0.227	0.642	0.356	0.185	0.087	0.183	0.054	0.093
0.081	0.134	0.179	0.169	0.825	0.145	0.142	0.120	0.042	0.086
0.087	0.126	0.038	0.053	0.323	0.166	0.170	0.068	0.203	0.115
0.067	0.153	0.032	0.118	0.105	0.128	0.159	0.079	0.018	0.089

ϕ *10^{-0}

3.142	0.000	0.000	0.000	3.142	0.000	0.000	3.142	0.000	3.142
4.174	1.024	2.353	1.196	3.112	0.749	4.139	4.298	3.042	1.085
1.161	3.519	4.074	4.066	4.486	2.704	4.688	3.083	0.823	3.458
3.948	1.175	0.154	4.513	4.695	3.925	-0.431	0.839	-0.551	0.918
-0.770	2.223	2.164	-0.977	2.602	-0.189	2.916	1.647	2.986	1.233
0.274	3.742	-1.208	1.269	-0.791	2.176	-0.414	1.679	4.658	-0.294
0.577	0.562	1.222	3.527	2.492	3.716	2.691	2.976	2.395	2.358
0.836	3.229	1.086	-0.255	-0.254	0.186	-0.255	-1.251	1.985	-0.155
3.801	-1.201	2.336	1.802	1.048	0.225	1.774	3.546	4.457	4.300
-0.736	1.175	4.595	3.838	1.222	0.784	-0.108	0.112	3.228	2.330
-0.497	-1.513	0.112	-0.269	2.908	3.029	4.101	-1.267	3.796	3.903
-0.002	3.207	2.546	2.593	-0.548	-0.125	0.909	-1.013	0.609	-0.844
-1.073	-1.291	3.075	3.677	2.037	1.631	0.562	-0.839	-0.949	2.292
0.812	0.131	2.596	2.466	3.447	2.312	0.359	-0.357	0.362	4.674
0.692	-0.548	4.060	-1.278	-0.699	1.923	2.424	1.340	1.811	-0.718

Z 2.1

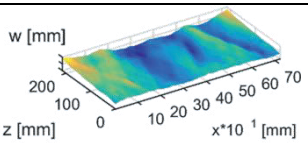

χ *10^{-2}

2.432	0.385	0.056	0.275	0.009	0.227	0.098	0.319	0.150	0.232
7.067	5.684	0.522	0.864	0.181	0.571	0.473	0.128	0.605	0.389
5.029	1.364	0.371	0.198	0.121	0.067	0.127	0.175	0.115	0.074
1.455	1.768	1.512	0.298	0.400	0.047	0.112	0.032	0.110	0.093
4.423	3.267	1.186	0.437	0.194	0.258	0.064	0.040	0.168	0.027
1.458	1.219	1.104	0.244	0.120	0.110	0.202	0.092	0.026	0.108
0.517	1.975	0.768	0.914	0.427	0.192	0.089	0.057	0.007	0.038
0.512	1.051	0.393	1.209	0.462	0.300	0.294	0.126	0.022	0.130
0.116	0.601	0.793	0.203	0.171	0.176	0.169	0.126	0.092	0.084
0.196	0.319	0.724	0.279	0.666	0.105	0.136	0.171	0.145	0.080
0.140	0.220	0.506	0.490	0.868	0.311	0.036	0.264	0.066	0.062
0.188	0.314	0.223	0.704	0.151	0.680	0.086	0.101	0.056	0.048
0.052	0.101	0.127	0.391	0.228	0.105	0.022	0.099	0.026	0.011
0.051	0.128	0.207	0.298	0.513	0.150	0.289	0.201	0.127	0.042
0.066	0.144	0.204	0.155	0.140	0.235	0.298	0.023	0.047	0.102

ϕ *10^{-0}

3.142	0.000	0.000	0.000	3.142	3.142	0.000	3.142	0.000	0.000
0.286	3.458	-1.019	3.380	0.888	3.895	2.094	4.523	1.221	-0.592
1.764	3.259	-0.684	0.129	4.240	3.229	4.597	3.830	-0.372	3.805
2.499	2.932	-0.447	-0.501	-0.093	4.527	2.154	1.233	4.490	-1.140
0.536	2.749	4.554	3.272	-1.399	3.732	4.446	-1.558	3.331	-1.481
-0.869	2.058	1.616	-0.813	4.164	3.829	3.930	2.390	-1.407	0.475
2.499	0.001	1.827	3.380	2.627	3.397	2.271	3.264	-1.072	0.876
1.380	-0.767	2.878	2.243	-1.182	3.950	4.680	4.613	2.831	1.638
1.348	2.834	-0.216	-0.739	2.657	-1.530	3.791	3.516	3.031	2.576
3.988	3.614	-1.260	0.938	1.359	-0.230	1.821	2.528	2.519	4.187
3.383	3.984	3.402	-0.167	0.477	3.578	2.766	3.127	2.338	-1.393
-0.126	-0.487	0.562	-0.950	2.582	2.381	3.149	4.297	-1.254	1.373
1.196	-0.900	2.282	3.934	0.876	0.582	-0.716	3.574	4.271	-1.466
2.928	3.366	2.880	3.220	3.125	0.804	0.288	0.622	0.280	0.230
2.360	1.919	2.821	-1.210	4.281	-0.509	0.019	4.379	1.100	4.631

Z 2.2

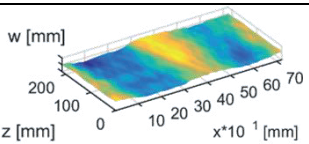

χ *10^{-2}

1.771	0.192	0.589	0.521	0.504	0.658	0.026	0.485	0.062	0.065
4.915	3.446	0.124	0.473	0.147	0.619	0.259	0.216	0.235	0.182
8.151	2.565	0.609	0.211	0.136	0.185	0.048	0.244	0.128	0.174
1.652	1.060	0.324	0.171	0.095	0.110	0.112	0.040	0.092	0.121
1.866	1.039	0.197	0.042	0.093	0.074	0.108	0.024	0.130	0.051
0.484	0.832	0.838	0.195	0.158	0.109	0.041	0.080	0.102	0.057
0.113	0.274	0.242	0.454	0.122	0.097	0.124	0.079	0.019	0.074
0.054	0.306	1.133	0.288	0.206	0.146	0.064	0.027	0.166	0.088
0.022	0.187	0.288	0.465	0.202	0.089	0.199	0.022	0.038	0.056
0.106	0.119	0.300	0.297	0.240	0.146	0.088	0.058	0.114	0.027
0.022	0.129	0.111	0.462	0.303	0.199	0.071	0.081	0.047	0.081
0.061	0.223	0.129	0.294	0.201	0.196	0.023	0.080	0.041	0.041
0.014	0.030	0.177	0.160	0.207	0.104	0.106	0.078	0.028	0.085
0.091	0.164	0.087	0.259	0.222	0.298	0.132	0.060	0.016	0.070
0.070	0.040	0.039	0.061	0.154	0.171	0.116	0.018	0.055	0.031

ϕ *10^{-0}

3.142	3.142	3.142	0.000	0.000	0.000	0.000	3.142	0.000	3.142
3.940	0.605	-1.236	-0.466	2.700	0.297	-1.203	4.546	-1.057	0.449
0.328	1.781	3.880	1.554	4.191	-0.576	-0.226	-0.241	1.464	4.629
-0.664	0.402	1.739	1.103	2.634	2.178	-1.517	-0.690	2.577	1.275
-0.081	1.990	3.275	1.611	3.727	1.392	3.876	2.024	3.562	0.071
1.375	4.048	1.734	1.216	1.608	2.955	0.620	3.946	1.399	1.108
0.416	3.870	2.917	-0.197	1.575	-0.835	-0.494	-0.561	3.478	3.258
3.300	3.520	0.458	0.147	3.792	3.099	3.610	3.401	4.213	2.379
0.734	2.979	0.194	-0.878	2.553	4.191	-0.904	-1.255	-0.156	3.833
0.461	-0.501	-0.075	1.591	2.280	-1.029	1.736	1.371	2.212	4.645
2.267	3.488	3.184	3.666	0.182	0.962	-1.310	0.107	4.369	0.230
4.139	0.241	-1.557	0.043	0.638	3.139	3.716	2.565	-1.277	3.314
0.832	-0.721	1.392	3.797	2.520	0.552	2.525	0.854	3.510	-0.772
2.701	4.088	2.452	4.474	2.540	0.728	-0.818	0.473	1.777	0.453
1.667	0.940	2.140	2.496	1.198	0.108	3.527	-1.121	1.654	4.030

Z 2.3

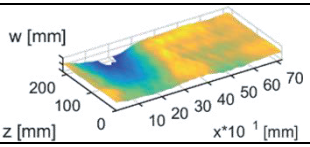

χ *10^{-2}

	2.350	2.703	0.520	0.104	0.931	0.744	0.596	0.569	0.272	0.872
	11.246	8.403	0.521	0.897	0.195	0.583	0.416	0.494	0.514	0.221
	7.825	1.609	0.213	0.174	0.217	0.050	0.263	0.077	0.115	0.178
	1.353	1.106	0.451	0.216	0.051	0.241	0.054	0.042	0.054	0.121
	1.332	0.626	0.138	0.242	0.250	0.156	0.231	0.083	0.135	0.159
	0.406	0.104	0.751	0.209	0.152	0.141	0.115	0.025	0.082	0.102
	0.186	0.380	0.119	0.109	0.244	0.052	0.099	0.037	0.052	0.137
	0.244	0.472	0.663	0.369	0.190	0.242	0.148	0.126	0.140	0.210
	0.082	0.201	0.475	0.192	0.282	0.110	0.028	0.043	0.051	0.125
	0.064	0.063	0.271	0.191	0.162	0.150	0.139	0.055	0.130	0.101
	0.118	0.075	0.096	0.078	0.290	0.068	0.033	0.021	0.030	0.109
	0.051	0.177	0.038	0.099	0.292	0.083	0.130	0.061	0.091	0.013
	0.040	0.065	0.072	0.224	0.299	0.138	0.065	0.037	0.027	0.034
	0.036	0.126	0.051	0.216	0.181	0.188	0.052	0.075	0.086	0.030
	0.038	0.141	0.015	0.076	0.084	0.306	0.029	0.052	0.015	0.031

ϕ *10^{-0}

	3.142	0.000	0.000	3.142	3.142	3.142	3.142	0.000	3.142	0.000
	4.596	1.449	-0.213	1.766	0.220	2.606	0.339	3.906	0.421	3.400
	-0.100	3.880	1.787	4.331	3.282	-1.137	3.076	1.284	3.118	0.937
	1.936	4.201	-1.392	4.270	3.727	4.383	3.809	4.337	2.204	0.557
	-0.365	2.446	0.835	2.277	4.621	3.200	-0.835	1.727	0.372	1.765
	1.727	4.084	-0.768	4.039	-1.554	-1.332	4.292	-0.464	1.051	1.561
	-0.144	1.742	2.397	-1.460	-0.218	0.122	-1.130	-1.452	3.115	2.153
	1.593	0.308	0.005	3.480	-1.054	-1.333	4.432	4.677	0.687	2.375
	2.531	3.846	2.226	-0.706	-0.141	2.028	-0.306	1.986	4.373	2.025
	2.177	1.023	2.109	3.405	3.128	0.962	0.807	0.322	3.693	2.975
	-1.003	3.870	1.894	-0.078	1.226	1.484	0.311	4.532	2.207	3.216
	2.728	0.134	3.189	-0.070	0.452	3.884	1.146	1.114	4.329	-0.189
	3.007	0.722	1.579	-1.330	-0.865	2.471	4.233	2.525	1.841	4.090
	4.628	3.239	0.894	2.401	2.052	0.245	4.126	0.503	-1.193	4.469
	2.795	-0.459	-0.955	0.476	1.383	2.841	-1.441	3.241	1.396	4.385

Z 2.4

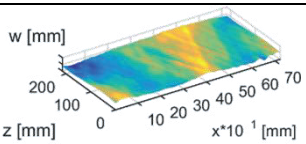

χ *10^{-2}

0.956	0.793	0.096	0.747	0.023	0.089	0.146	0.101	0.175	0.199
5.576	4.286	0.166	0.513	0.221	0.236	0.254	0.135	0.275	0.168
1.853	4.735	0.268	0.322	0.030	0.225	0.165	0.219	0.218	0.211
1.488	0.296	0.602	0.147	0.212	0.107	0.241	0.050	0.237	0.142
0.414	0.998	0.641	0.246	0.097	0.241	0.122	0.101	0.125	0.153
1.055	0.089	0.709	0.110	0.054	0.108	0.108	0.030	0.034	0.174
0.211	0.535	0.205	0.200	0.131	0.296	0.154	0.216	0.195	0.103
0.085	0.550	0.420	0.696	0.137	0.231	0.075	0.037	0.124	0.144
0.167	0.110	0.689	0.378	0.268	0.165	0.154	0.141	0.113	0.111
0.083	0.164	0.234	0.491	0.182	0.178	0.102	0.139	0.102	0.171
0.070	0.109	0.151	0.380	0.232	0.133	0.164	0.055	0.091	0.097
0.105	0.261	0.315	0.266	0.385	0.103	0.077	0.078	0.091	0.088
0.140	0.234	0.190	0.245	0.342	0.084	0.086	0.099	0.080	0.058
0.104	0.164	0.186	0.084	0.457	0.524	0.132	0.027	0.050	0.077
0.034	0.185	0.058	0.267	0.143	0.472	0.094	0.140	0.071	0.010

ϕ *10^{-0}

3.142	0.000	3.142	3.142	0.000	3.142	0.000	0.000	3.142	0.000
3.968	0.671	-1.559	0.984	0.587	1.667	0.762	3.171	-0.459	1.736
0.681	0.599	1.216	1.299	1.929	1.903	3.415	1.657	3.108	2.543
-0.112	0.949	3.422	-0.334	3.625	1.732	4.435	1.527	4.060	3.338
2.199	0.978	0.939	1.723	4.401	1.062	-0.215	1.025	4.110	1.369
-0.912	0.777	2.512	1.473	1.685	2.093	2.452	0.785	4.357	1.632
1.589	3.090	2.854	0.335	-1.439	0.979	-0.335	1.465	-1.445	1.168
3.624	1.154	0.895	4.547	0.432	3.743	1.957	3.223	0.248	1.991
3.379	2.877	4.530	2.504	1.828	4.130	0.187	-1.122	1.407	3.946
3.546	-0.099	4.132	4.461	0.203	3.390	4.077	4.506	3.928	4.339
1.773	3.422	2.759	3.399	4.312	4.275	-1.525	4.516	4.466	3.628
4.134	3.222	4.527	4.418	1.015	2.595	3.472	2.155	2.447	3.487
1.989	2.940	2.607	2.886	3.141	-1.276	-0.549	1.974	-0.927	3.021
1.893	4.218	1.640	4.294	1.058	1.731	-1.497	1.953	-0.842	1.700
0.273	1.684	1.227	2.368	2.038	-1.055	-0.383	1.230	1.881	-0.911

Z 2.5

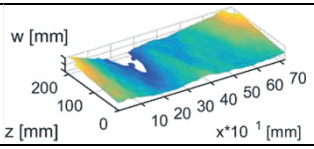

χ *10^{-2}

4.386	0.456	0.362	0.316	0.018	0.135	0.454	0.120	0.221	0.188
14.882	11.033	0.052	1.252	0.121	0.373	0.067	0.447	0.119	0.212
10.513	2.697	0.347	0.386	0.113	0.128	0.184	0.155	0.066	0.118
2.212	0.706	0.434	0.197	0.099	0.260	0.133	0.106	0.053	0.144
2.019	1.543	1.090	0.066	0.172	0.113	0.158	0.172	0.044	0.070
2.306	0.503	1.936	0.511	0.224	0.056	0.124	0.104	0.215	0.199
0.514	1.048	0.748	0.284	0.190	0.131	0.151	0.152	0.163	0.270
0.030	0.403	0.353	0.716	0.284	0.125	0.202	0.115	0.094	0.162
0.361	0.521	0.751	0.379	0.447	0.104	0.038	0.067	0.096	0.067
0.225	0.219	0.736	0.280	0.891	0.143	0.324	0.092	0.245	0.041
0.115	0.144	0.297	0.148	0.273	0.095	0.169	0.117	0.057	0.084
0.117	0.130	0.252	0.176	0.246	0.145	0.062	0.138	0.052	0.089
0.067	0.048	0.077	0.103	0.415	0.062	0.168	0.052	0.103	0.019
0.022	0.131	0.182	0.156	0.079	0.276	0.161	0.049	0.060	0.066
0.103	0.136	0.136	0.079	0.404	0.187	0.213	0.093	0.048	0.063

ϕ *10^{-0}

3.142	3.142	0.000	0.000	3.142	0.000	3.142	3.142	0.000	3.142
-0.561	2.579	2.005	2.615	2.821	2.681	3.210	2.736	3.724	2.628
0.227	2.485	1.828	2.956	2.934	2.459	3.209	2.214	2.584	2.439
1.820	3.258	-0.664	-0.663	-1.193	4.563	2.819	-1.534	1.922	-0.621
-0.884	2.220	1.075	1.698	1.037	3.056	1.323	3.116	2.668	2.298
1.538	3.576	-1.561	1.870	4.522	2.091	3.541	3.015	3.715	3.010
0.195	1.667	1.675	4.281	3.929	-1.235	4.385	-1.162	4.143	0.146
0.888	3.393	4.658	0.256	-0.553	-0.623	-1.191	1.774	0.243	1.660
2.601	-0.212	2.506	2.496	0.117	4.067	4.273	4.241	-0.574	-0.259
-0.488	2.706	0.285	1.105	3.455	-0.069	3.831	-0.810	4.376	4.254
1.763	0.764	2.707	3.524	-0.142	3.470	-0.524	4.161	2.428	4.084
1.420	3.170	1.535	4.211	3.815	-0.546	3.696	-1.281	3.775	3.751
1.406	2.080	1.150	2.937	1.949	-0.879	-1.318	-1.235	-0.909	1.520
-0.317	3.546	3.794	-1.465	3.904	1.011	0.650	0.754	0.031	4.232
2.971	3.050	4.198	1.950	-1.167	-0.922	1.640	-1.320	4.297	3.837

Z 2.6

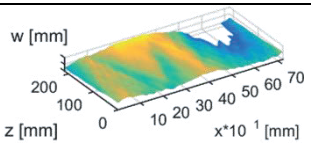

χ *10^{-2}

3.082	0.515	0.885	0.135	0.545	0.159	0.036	0.102	0.441	0.108
16.734	12.608	0.877	1.293	0.355	0.469	0.136	0.547	0.195	0.326
9.407	0.705	0.833	0.224	0.130	0.088	0.258	0.087	0.066	0.052
1.555	1.444	0.268	0.058	0.080	0.101	0.023	0.130	0.062	0.051
3.895	1.087	1.855	0.499	0.150	0.066	0.201	0.116	0.144	0.170
1.971	0.598	2.564	0.196	0.218	0.082	0.085	0.094	0.061	0.093
0.906	0.968	1.161	0.983	0.054	0.095	0.104	0.237	0.062	0.148
0.173	1.414	0.419	1.008	0.047	0.104	0.102	0.270	0.140	0.124
0.258	0.622	0.358	1.123	0.032	0.075	0.034	0.079	0.128	0.139
0.099	0.291	1.060	1.196	1.051	0.051	0.304	0.115	0.181	0.082
0.079	0.150	0.170	0.221	0.311	0.030	0.122	0.102	0.103	0.065
0.105	0.143	0.121	0.354	0.319	0.345	0.154	0.152	0.153	0.086
0.054	0.082	0.090	0.184	0.356	0.400	0.118	0.149	0.054	0.075
0.108	0.160	0.212	0.155	0.087	0.244	0.392	0.164	0.071	0.060
0.080	0.093	0.241	0.134	0.247	0.091	0.191	0.056	0.067	0.038

ϕ *10^{-0}

3.142	0.000	0.000	0.000	0.000	3.142	3.142	3.142	0.000	0.000
2.268	-0.901	2.852	-0.832	3.038	-0.609	3.902	-0.865	4.056	-0.916
1.005	1.050	-0.908	-0.553	-0.456	1.818	-0.618	-1.222	4.554	4.377
0.777	3.162	4.060	0.285	2.419	-1.133	-0.895	-0.602	2.989	4.237
1.642	0.525	-1.413	1.592	-1.522	4.288	-1.255	3.319	3.826	4.197
3.863	0.083	1.407	-0.183	0.645	0.794	3.104	0.536	-0.469	-1.343
0.974	1.134	4.159	3.583	1.181	4.487	0.964	4.110	1.904	-0.995
3.835	1.963	-0.742	-0.869	-0.078	-0.957	2.490	4.327	0.323	-0.477
1.601	3.062	3.242	0.376	3.878	-0.439	4.135	0.991	0.463	-0.485
-1.511	1.092	0.003	3.301	2.859	0.682	2.503	1.059	2.439	1.996
-0.418	3.811	1.526	2.327	-0.351	-0.272	1.914	1.754	2.022	2.664
0.014	-0.711	1.406	-1.013	1.987	2.518	0.374	2.890	3.995	3.518
3.794	4.282	1.151	-0.041	2.701	1.985	-0.535	4.582	-0.763	0.871
3.930	0.169	-1.506	-0.500	4.400	-1.359	-0.212	3.068	1.438	1.839
-1.462	-0.367	0.186	1.431	1.590	0.341	4.316	-1.021	-0.650	3.581

Literature

[Alm65] Almroth, B. O.: „Influence of Edge Conditions on the Stability of Axially Compressed Cylindrical Shells“, 1965.

[Ang07] Ang, A. H.-S.; Tang, W. H.: „Probability concepts in engineering“. Emphasis on applications in civil & environmental engineering. Wiley, New York, 2007.

[Arb01] Arbocz, J.; Starnes, J.; Nemeth, M.: „On a high-fidelity hierarchical approach to buckling load calculations“: 19th AIAA Applied Aerodynamics Conference, 2001, S. 1–21.

[Arb02] Arbocz, J.; Starnes Jr, J. H.: „Future directions and challenges in shell stability analysis“, in: Thin-Walled Structures, 2002, 40, S. 729–754.

[Arb05] Arbocz, J.; Hilburger, M. W.: „Toward a Probabilistic Preliminary Design Criterion for Buckling Critical Composite Shells“, in: AIAA Journal, 2005, 43, S. 1823–1827.

[Arb79] Arbocz, J.; Abramovich, H.: „The initial imperfection data bank at the Delft University of Technology“ TU Delft, 1979.

[Arb91] Arbocz, J.; Hol, A. M.: „Collapse of Axially Compressed Cylindrical Shells with Random Imperfections“, in: AIAA Journal, 1991, 29, S. 2247–2256.

[AST02] ASTM International: „Standard Test Method for Tensile Properties of Plastics“, West Conshohocken, PA, 2002.

[Ayy11] Ayyub, B. M.; McCuen, R. H.: „Probability, statistics, and reliability for engineers and scientists“, 2011.

[Bae03] Baecher, G. B.; Christian, J. T.: „Reliability and statistics in geotechnical engineering“. J. Wiley, Chichester, West Sussex, England, Hoboken, NJ, 2003.

[Bat47] Batdorf, S. B.: „A Simplified Method of Elastic Stability Analysis for Thin Cylindrical Shells“, 1947.

[Ber08] Bertsekas, D. P.; Tsitsiklis, J. N.: „Introduction to probability“. Athena Scientific, Belmont, Mass., 2008.

[Bia08] Biagi, M.; Del Medico, F.: „Reliability-based knockdown factors for composite cylindrical shells under axial compression“, in: Thin-Walled Structures, 2008, 46, S. 1351–1358.

[Bis03] Bisagni, C.; Cordisco, P.: „An experimental investigation into the buckling and post-buckling of CFRP shells under combined axial and torsion loading“, in: Composite Structures, 2003, 60, S. 391–402.

[Bis99] Bisagni, C.: „Experimental Buckling of Thin Composite Cylinders in Compression“, in: AIAA Journal, 1999, 37, S. 276–278.

[Bol62] Bolotin, V. V.: „Statistical Methods in the Nonlinear Theory of Elastic Shells“, Washington NASA Langley Research Center, 1962.

[Bro11] Broggi, M.; Schuëller, G. I.: „Efficient modeling of imperfections for buckling analysis of composite cylindrical shells“, in: Engineering Structures, 2011, 33, S. 1796–1806.

[Car69] Card, M. F.: „The sensitivity of buckling of axially compressed fiber-reinforced cylindrical shells to small geometric imperfections“, 1969.

[Car73] Carri, R. L.: „Buckling Behavior of Composite Cylinders Subjected to Compressive Loading“ NASA Langley Research Center, 1973.

[Cas14] Castro, S. G. et al.: „Geometric imperfections and lower-bound methods used to calculate knock-down factors for axially compressed composite cylindrical shells“, in: Thin-Walled Structures, 2014, 74, S. 118–132.

[Cha04] Chamis, C.: „Probabilistic simulation of multi-scale composite behavior“, in: Theoretical and Applied Fracture Mechanics, 2004, S. 51–61.

[Cha05] Chamis, C. C.; Abumeri, G. H.: „Probabilistic dynamic buckling of composite shell structures“, in: Special Issue Honouring Jack Vinson on his 75th BirthdayAlso to commemorate 40 years of service to the profession and the 30 year anniversary of the University of Delaware Center for Composite Materials, 2005, 36, S. 1368–1380.

[Chr95] Chryssanthopoulos, M.; Poggi, C.: „Probabilistic imperfection sensitivity analysis of axially compressed composite cylinders“, in: Engineering Structures, 1995, 17, S. 398–406.

[Deg10] Degenhardt, R. et al.: „Investigations on imperfection sensitivity and deduction of improved knock-down factors for unstiffened CFRP cylindrical shells“, in: Composite Structures, 2010, 92, S. 1939–1946.

[DIN01] DIN 1055-100: „Einwirkungen auf Tragwerke. Teil 100, Grundlagen der Tragwerksplanung, Sicherheitskonzept und Bemessungsregeln“. Beuth Verlag GmbH, Berlin, 2001.

[DIN96] DIN EN ISO 6721-3: „Plastics — Determination of dynamic mechanical properties — Part 3: Flexural vibration — Resonance-curve“, 1996.

[DIN97] DIN EN ISO 527-4: „Kunststoffe-Bestimmung der Zugeigenschaften; Teil 4: Prüfbedingungen für isotrop und anisotrop faserverstärkte Kunststoffverbundwerkstoffe“, 1997.

[DIN98] DIN EN 2564: „Carbon fibre laminates - Determination of the fibre-, resin- and void contents“, 1998.

[Don34] Donnell, L. H.: „A New Theory for the Buckling of Thin Cylinders under Axial Compression and Bending“, in: ASME Trans., 1934, 56, S. 795–806.

[Eli82] Elishakoff, I.; Arbocz, J.: „Reliability of axially compressed cylindrical shells with random axisymmetric imperfections“, in: International Journal of Solids and Structures, 1982, 18, S. 563–585.

[Eli87] Elishakoff, I.; van Mannen, S.; Arbocz, J.: „First-order second-moment analysis of the buckling of shells with random imperfections“, in: AIAA Journal, 1987, 25, S. 1113–1117.

[EN 02] EN 1990: „Eurocode-Basis of structural design“, 2002.

[Esn96] Esnault, P.; Klein, M.: „Factors of Safety and Reliability“. In (Burke, W. R. Hrsg.): Spacecraft Structures, Materials and Mechanical Engineering, Proceedings of the Conference held by ESA, CNES and DARA, Paris, 1996.

[Ess67] Esslinger, M.: „Eine Erklärung des Beulmechanismus von dünnwandigen Kreiszylinderschalen“, in: Der Stahlbau, 1967, S. 366–371.

[Ess69] Esslinger, M.; Geier, B.: „Buckling and postbuckling behavior of thin-walled circular cylinders“ Deutsche Forschungs- und Versuchsanstalt für Luft- und Raumfahrt, 1969.

[Ess70] Esslinger, M.: „Hochgeschwindigkeitsaufnahmen vom Beulvorgang dünnwandiger axialbelasteter Zylinder“, in: Der Stahlbau, 1970, S. 73–76.

[Fab02] Faber, M.; Sorensen, J.: „Reliability Based Code Calibration“, 2002.

[Fra69] Fraser, W. B.; Budiansky, B.: „The Buckling of a Column With Random Initial Deflections“, in: Journal of Applied Mechanics, 1969, 36, S. 233–240.

[Fri16] Friedrich, L.; Schröder, K.-U.: „Discrepancy between boundary conditions and load introduction of full-scale built-in and sub-scale experimental shell structures of space launcher vehicles“, in: Thin-Walled Structures, 2016, 98, Part B, S. 403–415.

[Gei02] Geier, B.; Meyer-Piening, H.-R.; Zimmermann, R.: „On the influence of laminate stacking on buckling of composite cylindrical shells subjected to axial compression“, in: Composite Structures, 2002, 55, S. 467–474.

[Gei91] Geier, B.; Klein, H.; Zimmermann, R.: „Buckling Tests with Axially Compressed Unstiffened Cylindrical Shells made from CFRP“. In (Jullien, J. Hrsg.): Proceedings of the International Colloquium on Buckling of Shell Structures, on Land, in the Sea and in the Air. Elsevier, London, 1991, S. 498–507.

[Gel13] Gelman, A.: „Bayesian data analysis“. Chapman and Hall/CRC, 2013.

[Gol11] Goller, B.; Schuëller, G. I.: „Investigation of model uncertainties in Bayesian structural model updating“, in: Journal of sound and vibration, 2011, 330, S. 6122–6136.

[GOM16a] GOM: „ARAMIS- 3D Motion and Deformation Sensor“. http://www.gom.com/metrology-systems/aramis.html, 15.07.2016.

[GOM16b] GOM: „ATOS - Industrial 3D Scanning Technology“. http://www.gom.com/de/messsysteme/atos.html, 15.07.2016.

[Gur13] Gurit: „EP137-CR527/120-35 Product Data Sheet“, 2013.

[Hah94] Hahn, H. T. et al.: „Structural design criteria for filament- wound composite shells - NASA CR-195125“, 1994.

[Har00] Hart-Smith, L. J.: „Backing-out Composite Lamina Strengths from Cross-Ply Testing“. In (Kelly, A.; Zweben, C. Hrsg.): Comprehensive Composite Materials, 2000, S. 149–161.

[Hex11] Hexcel: „HexPly 8552/34%/UD145/AS7 Product Data Sheet“, 2011.

[Hex14a] Hexcel: „HexTow AS7 4000 Product Data Sheet“. http://www.hexcel.com/Resources/DataSheets/Carbon-Fiber-Data-Sheets/AS7_4000.pdf, 25.12.2014.

[Hex14b] Hexcel: „HexPly 8552 Product Data Sheet“. http://www.hexcel.com/Resources/DataSheets/Prepreg-Data-Sheets/8552_eu.pdf, 30.10.2014.

[Hil04] Hilburger, M. W.; Starnes, J. H.: „Effects of imperfections of the buckling response of composite shells“, in: Thin-Walled Structures, 2004, 42, S. 369–397.

[Hil06] Hilburger, M. W.; Nemeth, M. P.; Starnes, J. H.: „Shell Buckling Design Criteria Based on Manufacturing Imperfection Signatures“, in: AIAA Journal, 2006, 44, S. 654–663.

[Hip92] Hipp, P. A.; Jensen, D. W.: „Design and analysis of filament-wound cylinders in compression“: 33rd Structures, Structural Dynamics and Materials Conference. American Institute of Aeronautics and Astronautics, 1992.

[Hof66] Hoff, N.: „Thin shells in aerospace structures“: AIAA 3rd Annual Meeting 29 November -02 December, 1966, S. 1–27.

[Hüh02] Hühne, C. et al.: „Sensitivities to Geometrical and Loading Imperfections on Buckling of Composite Cylindrical Shells“. In (CNES Hrsg.): Proceedings European Conference on Spacecraft Structures, Materials and Mechanical Testing, 2002.

[Hüh05] Hühne, C.: „Robuster Entwurf beulgefährdeter, unversteifter Kreiszylinderschalen aus Faserverbundwerkstoff“. Dissertation, Technische Universität Carolo-Wilhelmina zu Braunschweig, Fakultät für Maschinenbau TU Braunschweig, 2005.

[Hüh08] Hühne, C. et al.: „Robust design of composite cylindrical shells under axial compression — Simulation and validation“, in: Thin-Walled Structures, 2008, 46, S. 947–962.

[ISO97] ISO: „Statistical methods for quality control of building materials and components“, 1997.

[Jac92] Jackson, K. E.; Kellas, S.; Morton, J.: „Scale Effects in the Response and Failure of Fiber Reinforced Composite Laminates Loaded in Tension and in Flexure“, in: Journal of Composite Materials, 1992, 26, S. 2674–2705.

[Jon68] Jones, R. M.: „Buckling of Circular Cylindrical Shells with Multiple Orthotropic Layers and Eccentric Stiffeners“, in: AIAA Journal, 1968, 6, S. 2301–2305.

[Kep13] Kepple, J.: „Influence of imperfections on axial buckling load of composite cylindrical shells“. In (Hoa, S. V.; Hubert, P. Hrsg.): The 19th International Conference on Composite Materials, 2013.

[Kir89] Kirkpatrick, S. W.; Holmes, B. S.: „Axial buckling of a thin cylindrical shell: experiments and calculations“. In (Liu, W. K. et al. Hrsg.): Computational Experiments, 1989, S. 67–74.

[Koi70] Koiter, W. T.: „The Stability of Elastic Equilibrium“ NASA Langley Research Center, 1970.

[Kri10] Kriegesmann, B. et al.: „Probabilistic design of axially compressed composite cylinders with geometric and loading imperfections“, in: International Journal of Structural Stability and Dynamics, 2010, 10, S. 623–644.

[Kri11] Kriegesmann, B. et al.: „Fast probabilistic design procedure for axially compressed composite cylinders“, in: Composite Structures, 2011, S. 3140–3149.

[Kri12a] Kriegesmann, B.: „Probabilistic Design of Thin-Walled Fiber Composite Structures“. Dissertation, Hannover Gottfried Wilhelm Leibniz Universität Hannover, 2012a.

[Kri12b] Kriegesmann, B.; Hilburger, M. W.; Rolfes, R.: „The Effects of Geometric and Loading Imperfections on the Response and Lower-Bound Buckling Load of a Compression-Loaded Cylindrical Shell“. In (AIAA Hrsg.): 53rd AIAA/ASME/ASCE/AHS/ASC Structures, Structural Dynamics and Materials Conference, 2012b.

[Kru11] Kruschke, J. K.: „Doing Bayesian Data Analysis: A Tutorial with R and BUGS“. Academic Press, 2011.

[Lav00] Lavoie, J. A.; Soutis, C.; Morton, J.: „Apparent strength scaling in continous fiber composites“, in: Composites Science and Technology, 2000, 60, S. 283–299.

[Lie14] Liebig, W.: „Mikrostrukturelle Betrachtung des Einflusses von Poren auf die mechanischen Eigenschaften von faserverstärkten Kunststoffen“. Technisch-Wissenschaftliche Schriftenreihe. TUTech Verlag TU Hamburg-Harburg, 22, 2014.

[Lor08] Lorenz, R.: „Achsensymmetrische Verzerrungen in dünnwandigen Hohlzylindern“, in: Zeitschrift des Vereins Deutscher Ingenieuere, 1908, 52, S. 1706–1713.

[Lun34] Lundquist, E. E.: „Strength tests of thin-walled duralium cylinders“ NASA Langley Research Center, 1934.

[Meh12] Mehrez, L. et al.: „Stochastic identification of composite material properties from limited experimental databases, Part II: Uncertainty modelling“, in: Mechanical Systems and Signal Processing, 2012, 27, S. 484–498.

[Mey01] Meyer-Piening, H.-R. et al.: „Buckling loads of CFRP composite cylinders under combined axial and torsion loading – experiments and computations“, in: Composite Structures, 2001, 53, S. 427–435.

[Mor91] Morris, M. D.: „Factorial Sampling Plans for Preliminary Computational Experiments“, in: Technometrics, 1991, 33, S. 161–174.

[Opt13] Optronis: „CamRecord 5000“. http://www.optronis.com/de/home.html, 18.07.2016.

[Pet68] Peterson, J. P.; Seide, P.; Weingarten, V. I.: „NASA SP-8007-Buckling of thin-walled circular cylinders“, Hampton, VA, United States NASA Langley Research Center, 1968.

[Pla13] Plaumann, B.; Rasmussen, O.; Krause, D.: „System analysis and synthesis for the dimensioning of variant lightweight cabin interior“: 54th AIAA/ASME/ASCE/AHS/ASC Structures, Structural Dynamics, and Materials Conference. American Institute of Aeronautics and Astronautics, 2013.

[Pot01] Potter, K. et al.: „Heavily loaded bonded composite structures: design, manufacture and test of 'I' beam specimens“, in: Composite Structures, 2001, 51, S. 389–399.

[Pri12] Priyadarsini, R. S.; Kalyanaraman, V.; Srinivasan, S. M.: „Numerical and Experimental Study of Buckling of Advanced Fiber Composite Cylinders under Axial Compression“, in: Int. J. Str. Stab. Dyn., 2012, 12, S. 1250028.

[Ras15] Rasband, W.: „ImageJ- Image Processing and Analysis in Java“, 2015.

[Roo69] Roorda, J.: „Some statistical aspects of the buckling of imperfection-sensitive structures“, in: Journal of the Mechanics and Physics of Solids, 1969, 17, S. 111–123.

[Sch01] Schenk, C. A.: „Some aspects of simulation of stochastic processes and fields“, Innsbruck Institute of Engineering Mechanics, Leopold Franzens University, 2001.

[Sch03] Schenk, C. A.; Schuëller, G. I.: „Buckling analysis of cylindrical shells with random geometric imperfections“, in: International Journal of Non-Linear Mechanics, 2003, 38, S. 1119–1132.

[Sch05] Schulte, K.; Fiedler, B.: „Structure and Properties of Composite Materials“. TuTech Innovation GmbH, Hamburg, 2005.

[Sch10] Schillinger, D.; Papadopoulos, V.: „Accurate estimation of evolutionary power spectra for strongly narrow-band random fields“, in: Computer Methods in Applied Mechanics and Engineering, 2010, 199, S. 947–960.

[Sch13] Schillo, C.; Krause, D.: „Uncertainties in the prediction of CFRP laminate properties in the context of a reliability based design approach“. In (Hoa, S. V.; Hubert, P. Hrsg.): The 19th International Conference on Composite Materials, 2013.

[Sch15] Schillo, C.; Röstermundt, D.; Krause, D.: „Experimental and numerical study on the influence of imperfections on the buckling load of unstiffened CFRP shells“, in: Composite Structures, 2015, S. 128–138.

[Sch17] Schillo, C.; Kriegesmann, B.; Krause, D.: „Reliability based calibration of safety factors for unstiffened cylindrical composite shells“, in: Composite Structures, 2017, DOI: http://dx.doi.org/10.1016/j.compstruct.2017.02.082.

[Sic09] Sickinger, C.: „Verifikation entfaltbarer Composite-Booms für Gossamer-Raumfahrtsysteme“. Shaker, Aachen, 2009.

[Sim15] Simulia: „Abaqus 6.12“, 2015.

[Sin02] Singer, J.; Arbocz, J.; Weller, T.: „Buckling Experiments: Experimental Methods in Buckling of Thin-Walled Structures“. John Wiley & Sons, Inc, Hoboken, NJ, USA, 2, 2002.

[Sin09] Sin, G.; Gernaey, K. V.; Lantz, A. E.: „Good modeling practice for PAT applications: propagation of input uncertainty and sensitivity analysis“, in: Biotechnology progress, 2009, 25, S. 1043–1053.

[Siv06] Sivia, D.; Skilling, J.: „Data Analysis: A Bayesian Tutorial“. OUP Oxford, 2006.

[Sou14] Southwell, R. V.: „The General Theory of Elastic Stability“, in: Phil. Trans. Royal Soc., 1914, 213, S. 187–245.

[Sun87] Sun, G.: „Optimization of Laminated Cylinders for Buckling“, 1987.

[Tak12] Takano, A.: „Statistical Knockdown Factors of Buckling Anisotropic Cylinders Under Axial Compression“, in: Journal of Applied Mechanics, 2012, S. 1–17.

[Ten84] Tennyson, R. C.; Hansen, J. S.: „Optimum Design for Buckling of Laminated Cylinders“. In (Thompson, J.; Hunt, G. W. Hrsg.): Collapse: The Buckling of Structures in Theory and Practice. Cambridge University Press, 1984.

[Thi64] Thielemann, W.; Eßlinger, M.: „Einfluß der Randbedingungen auf die Beullast von Kreiszylinderschalen“, in: Stahlbau, 1964, 12, S. 353–361.

[Tim10] Timoshenko, P.: „Einige Stabilitätsprobleme der Elastizitätstheorie“, in: Zeitschrift für Angewandte Mathematische Physik, 1910, 58, S. 337–385.

[Tof11] Toft, H.; Sorensen, J.: „Reliability-based design of wind turbine blades“, in: Structural Safety, 2011, S. 333–342.

[Toh14] Toho Tenax Toho Tenax: „IMS filament Product Sheet“, 2014.

[Wei65a] Weingarten, V. I.; Morgan, E. J.; Seide, P.: „Elastic stability of thin-walled cylindrical and conical shells under axial compression“, in: AIAA Journal, 1965a, 3, S. 500–505.

[Wei65b] Weingarten, V. I.; Seide, P.: „NASA SP-8007 - Buckling of thin-walled circular cylinders“, Hampton, VA, United States NASA Langley Research Center, 1965b.

[Wel67] Welch, P. D.: „The use of Fast Fourier Transform for the estimation of Power Spectra: a method based on time averaging over short, modified periodigrams“, in: IEEE Transactions on Audio and electroacoustics, 1967, 15, S. 70–73.

[Wie07] Wiedemann, J.: „Leichtbau“. Elemente und Konstruktion. Springer, Berlin, Heidelberg, 2007.

[Yue10] Yuen, K.-V.: „Bayesian methods for structural dynamics and civil engineering“. John Wiley & Sons Asia, Singapore, Hoboken, N.J., 2010.

[Yur87] Yurgartis, S. W.: „Measurement of Small Angle Fiber Misalignments in Continuous Fiber Composites“, in: Composite Science and Technology, 1987, 30, S. 279–293.

[Zim92] Zimmermann, R.: „Optimierung axial gedrückter CFK-Zylinderschalen“. VDI-Verl., Düsseldorf, 207, 1992.

[Zim96] Zimmermann, R.: „Buckling research for imperfection tolerant fiber composite structures“. In (Burke, W. R. Hrsg.): Spacecraft Structures, Materials and Mechanical Engineering, Proceedings of the Conference held by ESA, CNES and DARA, Paris, 1996, S. 411–416.

Zum Forschungsthema betreute studentische Arbeiten

[AUG14] Augustin, T.: Bestimmung der Steifigkeit von CFK-Couponproben mit Hilfe dynamischer Analysen. Projektarbeit am Institut für Produktentwicklung und Konstruktionstechnik, Hamburg 2014.

[KRA13] Kranz, M.: Untersuchung von Unsicherheiten bezüglich Coupontests zur Bestimmung von Steifigkeit und Festigkeit von FKV. Bachelorarbeit am Institut für Produktentwicklung und Konstruktionstechnik, Hamburg 2013.

[MEY15] Meyer, N.; Sensitivitätsuntersuchungen an unversteiften Zylinderschalen. Bachelorarbeit am Institut für Produktentwicklung und Konstruktionstechnik, Hamburg 2015.